THE NONLINEAR THERMAL EVOLUTION OF CORONAL STRUCTURES

César Augusto Mendoza Briceño

A Thesis Submitted for the Degree of PhD
at the
University of St Andrews

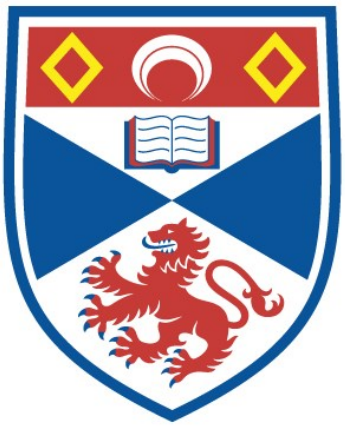

1996

The Nonlinear Thermal Evolution of Coronal Structures

César Augusto Mendoza Briceño

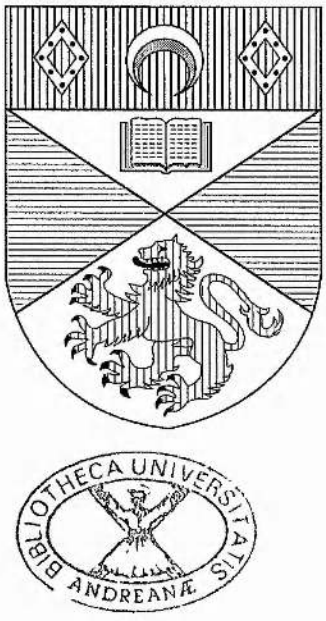

Thesis submitted for the degree of Doctor of Philosophy of the

University of St. Andrews

April 23th 1996

ProQuest LLC.
789 East Eisenhower Parkway
P.O. Box 1346
Ann Arbor, MI 48106 – 1346

Th
C40

Abstract

The thermal equilibrium and evolution of coronal structure is studied in this thesis. A symmetric and constant cross-sectional coronal loop is considered and, because of the strong magnetic field, the plasma is confined to move along the field lines , so that a one-dimensional problem can be assumed.

We begin by giving a brief description of the Sun and corresponding phenomena. Then a discussion of the basic MHD equations is given. Here, it is assumed that the heating function is spatially dependent and the cooling function is due to an optically thin plasma.

The thermal equilibrium of uniform-pressure coronal loop is investigated. The effects due to varying the values of the parameters involved in the governing equations are studied. It is found that there is a critical decay length of the heating below which a hot coronal loop does not exist. It is suggested that thermal non-equilibrium occurs, allowing the existence of catastrophic cooling. A study of the stability of the equilibrium up to the second order approximation is presented, and it is found that the response of the structure not only depends on the amplitude of the disturbance, but also on whether the disturbance increases or decreases the static temperature.

The thermal evolution of the above structure is also investigated by assuming that the inertial terms are small. The previous results related to the critical heating decay length are verified. The numerical simulation shows that an initial hot plasma evolves to a new equilibrium which has a cool summit. This equilibrium is identified as a prominence-like solution. Further investigations are made in order to show how the structure can either evolve to a hot or a cool summit temperature depending on whether the initial conditions are above or below threshold values. The evolution of a disturbance increasing or decreasing a initial equilibrium temperature is followed numerically verifying the prediction made in the stability analysis.

Furthermore, the effect of gravity is considered in the thermal equilibrium of loop. Similar results were found as studied for a constant-pressure loop. However, it was found that the critical values in which thermal non-equilibrium can occur is increased. A magnetic dip is also included in this model and the thermal equilibrium is studied.

Finally, extensions of the present work is presented and some preliminary results are discussed.

Esta tesis es dedicada a
Beatriz y a mi hijo César Augusto.
Porque sin ellos
mi espiritu hubiera estado vacio.

Declarations

1. I, **César Augusto Mendoza Briceño**, hereby certify that this thesis, which is approximately 35,000 words in length, has been written by myself, that it is a record of work carried out by me and that it has not been submitted in any previous application for a higher degree.

   Date: 23/4/96 Signature of candidate: .

2. I was admitted as a research student in October 1992 and as a candidate for the degree of Doctor of Philosophy in October 1993; the higher study for which this is a record was carried out in the University of St. Andrews between 1992 and 1996.

   Date: 23/4/96 Signature of candidate: ...

3. I hereby certify that the candidate has fulfilled the conditions of the Resolution and Regulations appropriate for the degree of Doctor of Philosophy in the University of St. Andrews and that the candidate is qualified to submit this thesis in application for that degree.

   Date: 23/4/96 Signature of supervisor: ..

4. In submitting this thesis to the University of St. Andrews I understand that I am giving permission for it to be made available for use in accordance with the regulations of the University Library for the time being in force, subject to any copyright vested in the work not being affected thereby. I also understand that the title and abstract will be published and that a copy of the work may be made and supplied to any *bona fide* library or research worker.

Date: 23/4/96 ..... Signature of candidate:

Acknowledgements

I have to thank my supervisor Dr. Alan Hood for his guidance and overall help. Prof. Eric Priest was instrumental in granting me the opportunity to join the Solar Group and for this I give him my sincere thanks. For the many constructive discussions which I have had with former and present members of the Solar Physics Group, too numerous to mention by name, I shall remain ever grateful. My special thanks are due to Dr. Jack Ireland for his kindness in reading the manuscript of this thesis. For the inspiration, interest and continuous encouragement which Prof. Miguel Ibañez has given me throughout my scientific development, I express my profound thanks. To my fellow postgraduates which whom I shared an office, I accord my appreciation and will treasure happy memories of our friendship.

My wife Beatriz and I say an especial thankyou to María Cristina, Frances and David for being our friends. Last but not least I have to thank my family: particularly my Mum whose determination, constancy and perseverance has always been an example and an inspiration for me.

Finally, I gratefully acknowledge the Sir Harold Mitchell Scholarship from the University of St. Andrews and the financial support which I received from the Consejo Nacional de Investigaciones Cientificas y Tecnológicas and from the Universidad de los Andes, Venezuela.

Contents

Chapter 1

Description of the Sun

1.1 Introduction

A brief description of the Sun, and the most important phenomena that occur upon it, is given in this chapter. For mankind, the Sun has fulfilled different roles during the period that civilisations have waxed and waned upon the Earth. Many ancient civilisations worshipped the Sun as a god who brought light and life to the Earth, whilst others gave scant attention to the Sun when they compared it with the myriad of other celestial bodies. In spite of belonging to this latter group, Chinese astronomers of the first millennium were already undertaking observations of sunspots and eclipses. From 23 B.C. until the middle ages sunspots were observed systematically by the Chinese; and they were first observed through the telescope by Scheiner and by Galileo. The systematic study of the other phenomena including solar eclipses began in 1836, and it was only seven years later that Schwabe proposed that sunspot activity was cyclical and that it exhibited a periodicity of eleven years. During the last two centuries a far greater interest has been taken in the Sun. This is especially true of the last 50 years when significant discoveries have been made, including high resolution observations both from the ground and from space which have revealed, in fine detail, new features of the photosphere and chromosphere. In recent times many satellites, including Skylab, have been launched with the sole purpose of observing the Sun, and further projects including SOHO are envisaged.

The fact that the Sun is the only star that can be observed in great detail, means

that the data, thus derived, can be applied to understand the processes occurring in more distant stars. Furthermore, the Sun can be regarded as a natural laboratory from whose surface energy in the form of electromagnetic radiation has been emitted for thousands of millions of years, at the rate of 4×10^{23} kilowatts per second.

The source of this energy is derived from nuclear fusion reactions occurring within the Sun. Understanding how these reactions occur and how they could be reproduced in a controlled way, would offer a source of almost limitless energy.

Other phenomena of importance to the Earth include magnetic storms and polar auroras that can be attributed to the interaction of the solar wind with the Earth's magnetic field.

1.2 Observations

Observation of the Sun with the naked eye is not recommended, and even when dark filters are employed, it is almost impossible to identify surface details. A preferable method is to project, using a small telescope, a full disk image of the Sun onto a white surface.

Photographs from recent solar observations (see the examples in Priest, 1982 and Zirin, 1988) have shown many fascinating and varied events occurring on or near the Sun.

The Sun is known to be a fairly typical, middle aged, main sequence star. It is about 4.5×10^9 years old, has a mass of 1.99×10^{30} kg, a radius of 6.96×10^8 m, and consists of a massive ball of plasma that is held together and compressed by its own gravitational attraction. This plasma consists of about 90% hydrogen, 10% helium, and 0.1% of other elements such as carbon, nitrogen and oxygen. These minor elements are extremely important in the radiative losses used in this thesis.

The Sun may be considered in two parts: (i) the Sun's interior (which constitutes the main body of the Sun) and (ii) the Sun's atmosphere, both of which will be described in the following two subsections. The solar atmosphere and interior are depicted in Figure 1.1.

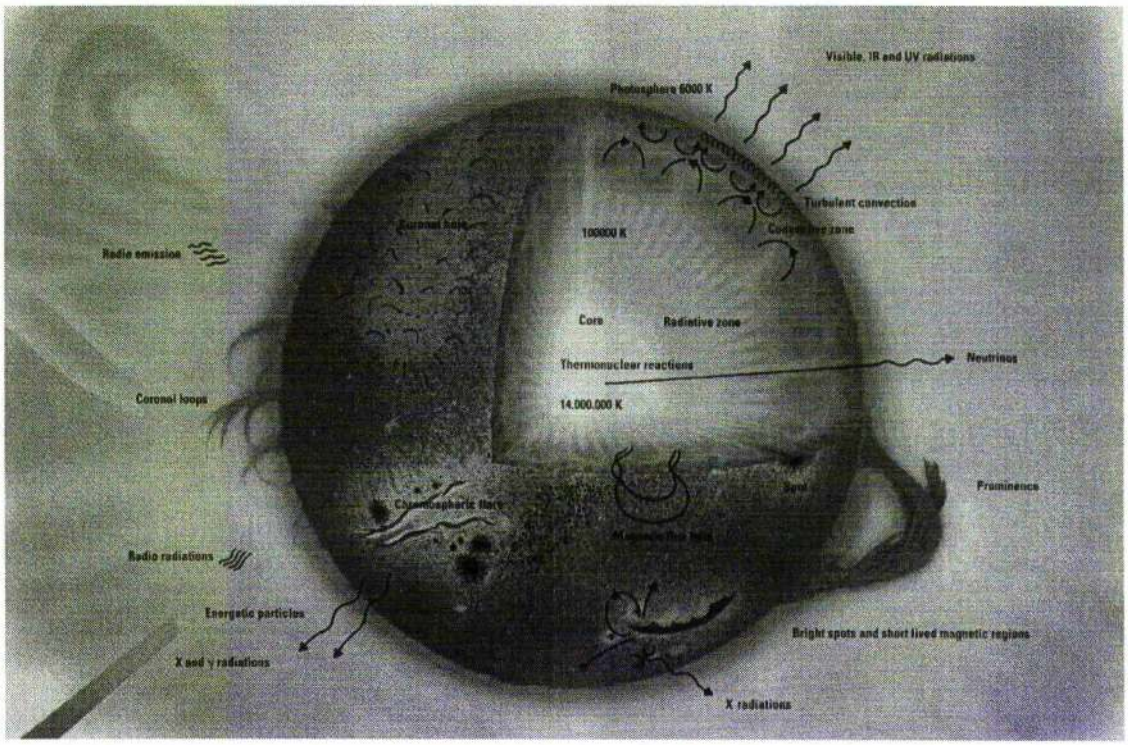

Figure 1.1: The overall structure of the Sun, showing the different regions, their temperatures and several features observed in the solar atmosphere. (From homepage: http://www.anu.edu.au/Physics/nineplanets/sol.html)

1.2.1 Solar Interior

This region of the Sun is hidden from view. Consequently, identification of the conditions therein depends to a large degree on the application of theoretical models.

The Sun's interior is comprised of three layers: the central core, the radiative zone, and the convection zone. The core, which occupies a region extending to about 0.25 of the solar radius, is believed to have a temperature of 1.5×10^7K, a density of $1.6 \times 10^5 \text{kgm}^{-3}$ and to generate energy through the fusion of 5 million tons of hydrogen per second to form helium. Most of the energy released in the core is primarily in the form of γ-ray and X-ray radiation or high energy, short wavelength "photons". These photons cannot travel far before undergoing absorption owing to the high opacity of the interior. Consequently, it can take the photons something like $\sim 10^7$ years to reach the surface via absorption and emission. If the photons were to reach the surface directly, the time taken would be only 2 seconds. This process

of absorption and re-emission occurs in the radiative zone, which extends from 0.25 solar radii ($R_\odot$) to over $0.7R_\odot$. During the numerous absorptions and emissions the energy is continually downgraded until the photons emerge, at the surface of the Sun, as visible light. Beyond 0.7 $R_\odot$ is the convection zone. In this zone the transport of energy is mainly by convection in which a hot parcel of plasma carries heat as it rises to the surface, cools and starts to sink; meanwhile other plasma has begun to ascend to replace it. At the surface, the temperature and density, are found to have diminished to 6,600K and 4×10^{-4}kg m^{-3} respectively.

1.2.2 Solar Atmosphere

The solar atmosphere consists of three parts, the photosphere, chromosphere and corona. The lowest level is the photosphere, it is only 500km thick, from which most of the Sun's visible light is emitted. The photosphere has a density of about 10^{-4}kgm^{-3} and a temperature that falls from the surface value of 6,000K towards 4,300K, the value at the temperature minimum. In high resolution observations the photosphere appears covered with irregularly shaped areas resembling "cobble stones", called granular cells or granules, that are in continual motion. It seems likely that the centre of these granules are rising convection cells of hotter gas. They are visible in white light and have a typical diameter ranging between 700km and 1,500km with lifetimes of between 7 and 10 minutes, and have vertical velocities of order 1 km s^{-1}. Supergranules cells are also found in the solar photosphere but are not visible in white light but instead through the Doppler effect. They are very irregular in shape, and are much larger than granules. Typical diameters range from 1.0×10^4km to 5.4×10^4km, (Leighton et al., 1962). Supergranular cells have a lifetime of about 20 hours and the motion is mainly horizontal with typical velocities of about 500m s^{-1}. At the edges of these cells, in the downdraughts, are found small concentrations of magnetic field of about 30G. At the junction of three cells the magnetic field strength can be as high as $1 - 2$kG. Other cells, at scales in between granulation and supergranulation, exist called mesogranulation, with sizes of about 5,000km approximate speeds of 60 m/s and lasting several tens of minutes.

The next level is the chromosphere, with a thickness of 2,500km. The number

density is $10^{17}\mathrm{m}^{-3}$. Through this level the temperature increases monotonically from a minimum temperature of 4,300K to 10^6K. Many fine structures can be observed within the chromosphere in Hα, for instance spicules and fibrils; more details will be given in the next section.

The final level is the corona that extends outwards from the transition region, the boundary between the chromosphere and the corona (about 0.5 Mm thick) where the temperature gradients are the highest found on the Sun. At the top of the transition region the corona is at a temperature of about 2×10^6K and number density of $5 \times 10^{14}\mathrm{m}^{-3}$. It is a hot tenuous plasma that cannot be seen with the unaided eye except during a total eclipse. Recently, however coronographs have been developed and, using these, the corona has been studied in considerable detail for much longer periods of time. Individual features of the white-light corona have been recorded, and it was recognised from this observation that coronal structures were generally either 'closed' resembling arches, or 'open', i.e. directed outwards but not necessarily radially. A distinction was made between closed forms with large 'arches', and smaller ones 'loop'. The arches are fainter and more stable, and the loops brighter and often associated with solar flares (Phillips, 1992). The corona has also been observed by satellites in soft X-rays. These observations show the same features as those seen in white-light, but with the advantage that structures on the solar disk could be observed as well. The corona was shown to be composed entirely of loops or arches with temperatures of $2-4 \times 10^6$K and number density of $1-7 \times 10^{15}\mathrm{m}^{-3}$, with their footpoints attached to the photosphere or chromosphere, and dark regions known as coronal holes, with a typical temperature in the range $1 - 1.5 \times 10^6$ and number densities of $4 \times 10^{14}\mathrm{m}^{-3}$ where very low or even zero X-ray emission were observed. The various features in the X-ray or white-light corona strongly suggest that they have a magnetic origin and that the magnetic field dominates the corona.

1.3 Features of the Sun

In this section, various interesting properties of the Sun will be discussed.

In the solar atmosphere there are different areas with different amounts of mag-

netic flux. There are some areas in which this flux is larger than others and are called active regions. These regions play an important part in many solar phenomena. Well known features found on the Sun are sunspots. These are observed in the photosphere, often within a mature active region. A typical sunspot consists of a darker central region called the umbra and an outer region, the penumbra. Both the umbra and the penumbra appear dark compared with the brighter photosphere because they are cooler than the average photospheric temperature. The umbra generally has a temperature of about 4,000K compare to about 5,500K for the penumbra, and about 6,000K for the photospheric granules (Priest, 1982).

Very strong magnetic fields are associated with sunspots. Most have a vertical magnetic field ranging between $1-2$kG, but they can occasionally exceed 4kG. The magnetic field strength increases with the area of the spot and the darker the spot, the stronger the field.

Sunspots range in size from tiny pores about the size of individual granules (about 1,000km in diameter), which appear as dark spots within the penumbra, to complex structures several tens of thousands of kilometers in diameter, covering areas of up to some 10^9km^2. A large group of sunspots may extend over a distance in excess of 10^5km. Sunspots are generally found in pairs which gradually drift apart from one another, up to a distance of about 1.5×10^5km (Bray and Loughhead, 1964).

Fibrils are a feature observed in Hα on the disk and within the chromosphere. They are short-lived structure (10 to 20 min) essentially of horizontal strands of gas, typically 10,000km long and 1,500 to 2,000km wide, suspended at a height of 2,000km above the photosphere and show up as dark absorption features. They are usually found near and at the edges of actives regions. The fibrils connect areas of opposite magnetic polarity and are believed to be aligned with the local magnetic field.

Spicules also form part of the fine structure found in the chromosphere. Spicules are "spike-like" jets seen in the upper part of the solar chromosphere in the red hydrogen line (Phillips, 1992). They are usually cylindrical or cone-shaped and rise to a height of about 1,000km, with an ascending speed ranging from 20kms^{-1} (Schmidt, 1974) to about 25kms^{-1} (Michard, 1974). Spicules have a typical lifetime of 5 to 10 min, diameter of 500 to 1,200km, maximum lengths of 10,000 to 20,000km,

temperatures of 1 to 2×10^4K and electron densities of 3×10^{16} to 3×10^{17}m^{-3}. They are much cooler and denser in comparison to the plasma surrounding them. There are roughly 30 spicules to each supergranule cell at any given time, and their average inclination to the vertical is 20° (Priest, 1982).

Occasionally, solar flares may be observed. This is perhaps the most spectacular and energetic form of solar activity, both because of its dominance as a primary energy release mechanism in the solar atmosphere and of its effect upon the Earth's upper atmosphere. A flare is seen in Hα as a rapid brightening. Flares usually form in the low chromosphere (invariably within active regions) and consist of various phases, the preflare phase, the flash phase and the main phase. The preflare phase, occurs 10 minutes before the flare onset, indicates an enhanced thermal emission due to some preflare heating. In the flash phase, the intensity of the emission increases rapidly over a period of about 5 minutes, whereas in the main phase the emission slowly decreases and lasts between an hour and a day. The energy released by the flare is approximately 10^{22}J for a small flare to 3×10^{25}J for a large flare. The origin of this energy is believed to come from the stressed magnetic field.

Magnetic loop structures seem to be the basic building blocks of the entire corona as mentioned in section 1.2.2. Material is concentrated with higher densities and temperatures in these structures. They connect points on the solar surface of opposite magnetic polarity and cross the polarity inversion line (or neutral line). An individual loop normally lasts from about a day upwards, with a loop system having a much greater lifetime. Observations show that coronal loops, depending on their temperature, can be divided into two distinct categories. Loops formed at temperatures greater than $\sim 1 \times 10^6$K are conventionally referred to as 'hot' loops, whereas those formed at lower temperature are called 'cool' loops.

The range of temperature covered by the cool loops extends from $\sim 20,000$K to $\sim 1 \times 10^6$K; the lower temperature is characteristic of loops observed in Hα. Hot loops are those loops formed at coronal temperatures of a million degrees or more. Bray et al., (1991) discuss the different properties of hot loops and cool loops, and conclude that hot loops tend to be thicker, longer, higher, and longer lived than cool loops, with which they are not co-spatial - that is, quiescent hot loops do not have cool cores (Pneuman and Orral, 1986). However, Bray et al. (1991) indicate that

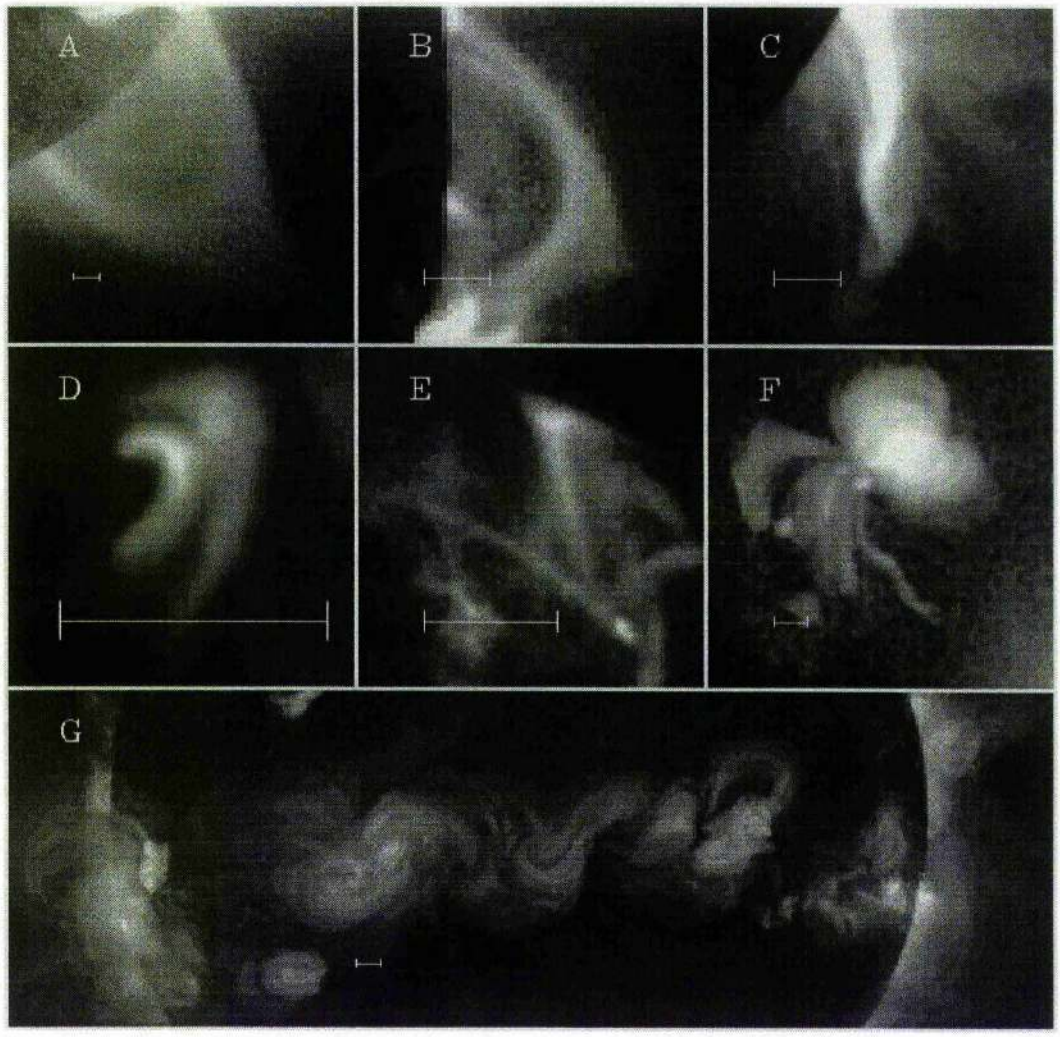

Figure 1.2: Variety of solar coronal features seen in Soft X-rays, showing loop structuring. A) Large Helmet type structure. B) Arcade of X-ray loops. C) Dynamic eruptive. D) Symmetrical flaring loops. E) Two cusped loops. F) Tightly beamed X-ray jet. G) The sinuous magnetic connection between active regions. (From SXT homepage: http://porel.space.lockheed.com/SXT/html/data.html)

the other morphological and physical properties, except temperature, are similar.

Priest (1982) divided loops into five broad categories namely (i) interconnecting loops, which link two active region, (ii) active region loops within active-regions, (iii) quiet region loops outside active-regions and (iv) simple-flare and (v) post-flare which are observed during and after solar flares (see Table 1.1).

Types of Loops	Length (Mm)	Temperature (K)	Density (m^{-3})	Pressure (Pa)
Interconnecting	$10 - 350$	$2 - 3 \times 10^6$	7×10^{14}	$0.02 - 0.03$
Quiet region	$10 - 350$	$1 - 8 \times 10^6$	$0.2 - 1.0 \times 10^{15}$	$0.005 - 0.025$
Active region	$10 - 50$	$10^4 - 2.5 \times 10^6$	$0.5 - 5.0 \times 10^{15}$	$7 \times 10^{-5} - 0.17$
Post-flare	$10 - 50$	$10^4 - 4 \times 10^6$	10^{17}	$0.01 - 5$
Simple-flare	$2.5 - 25$	$\lesssim 4 \times 10^7$	$< 10^{18}$	500

Table 1.1: Morphological Properties of different type of loops.

The next section will discuss prominences that occur within loop structures.

1.4 Prominence Observations

Solar prominences are one of the most noticeable of solar features. They are located in the solar corona with a temperature about a hundred times lower and a density about a hundred or more times higher than the corresponding coronal values.

In Hα they appear as bright features on the limb due to their own emission and in absorption on the disk as long and dark features (see Figures 1.3 and 1.4 respectively). The latter is called a filament.

Several attempts have been made to classify prominences depending on such properties as morphology, motions, spectra, or association with other activity (Secchi, 1875, Young, 1896; Pettit, 1925; Menzel and Evans, 1953; de Jager, 1959; and Zirin, 1979). Secchi (1875) classified them into two principal classes, quiescent and plage filament. de Jager has categorised them as moving and non-moving prominences. Menzel and Evans (1953) grouped them according to whether they were

Figure 1.3: Prominence in Hα at the limb. (Courtesy of Meudon Observatory)

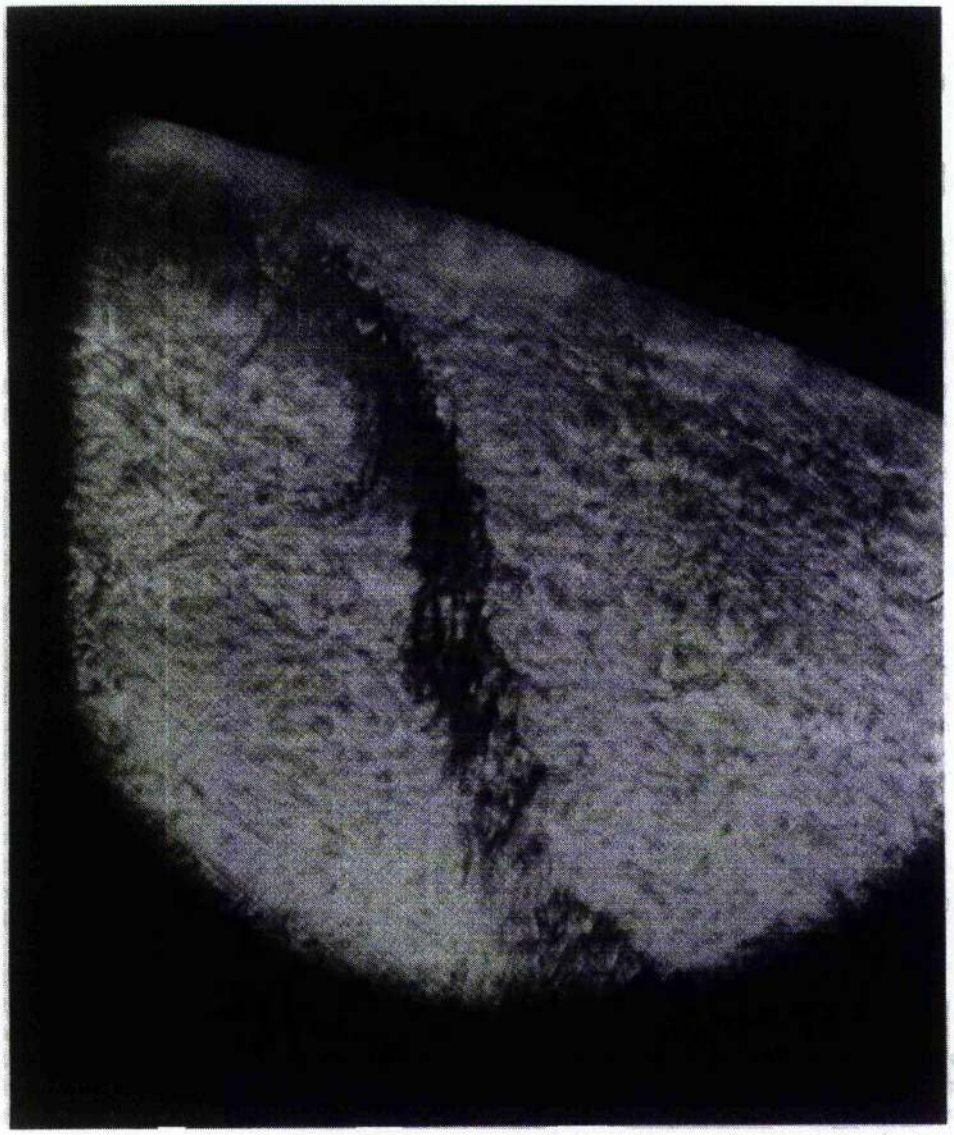

Figure 1.4: Prominence at high resolution on the disk showing fine structures. (Courtesy O. Engvold of Swedish Observatory, La Palma)

associated with sunspots or not, and to whether they appeared to originate in or below the corona. However, prominences may be divided into two principal types, namely active and quiescent prominences (Tandberg-Hanssen, 1974; Priest, 1982; Hirayama, 1985, Zirin, 1988). Table 1.2 shows this classification based on Zirin, (1988).

Class 1.	Quiescent prominences
	a) in or near active regions.
	b) in quiet regions.
	c) ascending prominences.
Class 2.	Active (Flare-associated, transient) prominences.
	a) limb flares.
	b) loops and coronal rain.
	c) surges.
	d) sprays.

Table 1.2: Classification of prominences (from Zirin, 1988).

1.4.1 Active Prominences

Active prominences are those located in active regions (i.e regions which are controlled by intense localised magnetic fields), and are normally associated with flares. They are dynamic structures with violent motions and have lifetimes from about a few minutes to a maximum of a few hours. They have a mean length of about 60Mm and they are normally associated with sunspots groups.

Typical active prominences are surges, sprays and loop prominences. Surges and sprays, are the principle manifestations of mass motions produced by solar flares. Surges are jets of material that are constrained and guided by the magnetic field, and which fall back to the Sun along the same path. Sprays are more explosive, fragmented ejections that escape from the active region and often from the Sun. In loop prominences the material appears to condense from the corona and fall under gravity into the Sun along magnetic field lines. The magnetic field strength ranges

from $20 - 100$G and an average active prominence will have an electron density of about $10^{17}\mathrm{m}^{-3}$.

1.4.2 Quiescent Prominences

Quiescent prominences are stable structures that can last from a few days to many months. They occur outside active regions. A typical quiescent prominence will have a temperature of about $7,000$K, an electron density of $10^{17}\mathrm{m}^{-3}$ and a magnetic field strength ranging from 5 to 10G. Their typical dimensions are length of about 2×10^{5}km, height of 5×10^{4}km high and width of 6×10^{3}km (See Table 1.3 for general ranges)

Parameter	Ranges
Length	60 - 600 Mm
Height	10 -100 Mm
Width	4 -15 Mm
Density	$10^{16} - 10^{17}\mathrm{m}^{-3}$
Magnetic Field	$3 - 30$G
Central Temperature	$5.000 - 8.000$K
Central Mean Molecular Weight	$0.6 - 0.9$

Table 1.3: Quiescent Prominences properties ranges.

It is important to note that the values for the temperature, density, and magnetic field strength are not uniform and will vary spatially and temporally within the prominence.

Observations show that prominences are always found to overlay the so-called photospheric neutral lines (Figure 1.5) i.e. the inversion line between regions of opposite magnetic polarity (Babcock and Babcock, 1955). In the chromosphere, a neutral line is characterised by having chromospheric fibrils aligned parallel to it. The fibril outlines a so-called filament channel.

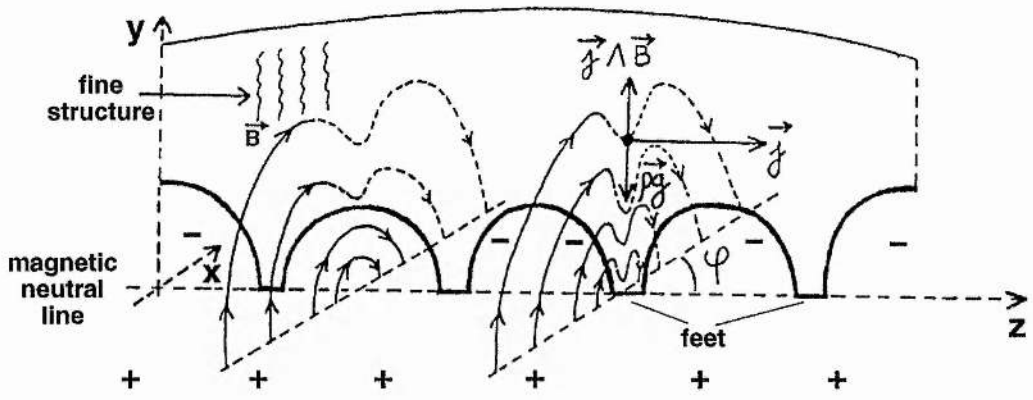

Figure 1.5: A schematic prominence (Schmieder, 1989)

A quiescent prominence is part of a much larger structure, a coronal helmet streamer (Figure 1.6). The central part of the helmet surrounding the prominence is less bright than the rest of the structure when it is observed in white light. This darker and less dense innermost volume is called a coronal cavity (Kawaguchi, 1967; Saito and Hyder, 1968; Saito and Tandberg-Hanssen, 1973). The cavities are also visible in X-ray, where they appear as long dark structures overlaying photospheric neutral lines. The mass of a quiescent prominence is not accurately known, but it is thought to be about one tenth the total mass of the corona (Tandberg-Hanssen, 1974).

Motions have been observed within and around prominences. Within the prominence, material seems to fall down, when it is observed at the limb (Dunn,1960; Engvold, 1976), but when it is viewed on the disk, upward motions are detected. Engvold (1976), found predominantly downward motions in the vertical threads with speeds of $15 - 35 \mathrm{kms}^{-1}$, although nearer the top of the prominence coarser knots move more slowly with speed of about $0.5 \mathrm{kms}^{-1}$. However, Doppler velocities in filament are generally small, between $1 - 3 \mathrm{kms}^{-1}$, steady, and mainly upwards, except at the feet of a hedgerow prominence, where speeds may reach $10 \mathrm{kms}^{-1}$ either up or down (Zirker, 1989).

Around a prominence, plasma is also observed to be in motion. The transition zone shows the same ascending behaviour with persistent large scale motions of about

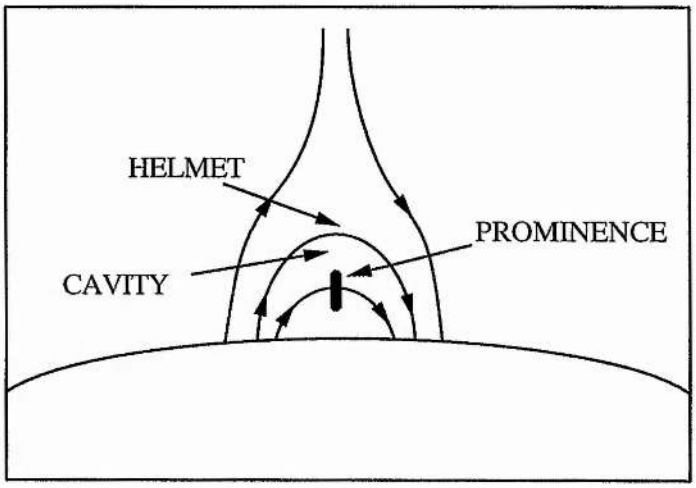

Figure 1.6: Formation times of various prominence features (adapted from Forbes, 1986)

$5-10\text{kms}^{-1}$ (Lites et al., 1976; Dere et al., 1986) and horizontal motions of the same order close to the prominences axis, with an inclination of $\simeq 20°$and parallel to the magnetic field lines.

Quiescent prominences are rather stable, as mentioned before, however parts of quiescent filaments can erupt, often followed by a reformation at the same place. During their lifetime, the filaments tend to become stretched in the east-west direction due to the action of the differential rotation.

Comparing, quiescent prominences to active prominences, the latter tend to be smaller by a factor of about $3-4$. The magnetic field strength tends to be greater by a factor of about ten. The density is similar to that found in quiescent prominences. Another important characteristic of quiescent prominences is the feet. These are regions where the prominence appear to have anchorage on the solar surface (Figure 1.7). The feet are spaced about $30,000$km apart, similar to the size of a supergranule cell. These feet are located at the boundaries of supergranules (Plocieniak and Rompolt, 1972; Martin, 1986) and are believed to be due to a plasma collapse (Nakagawa and Malville, 1969).

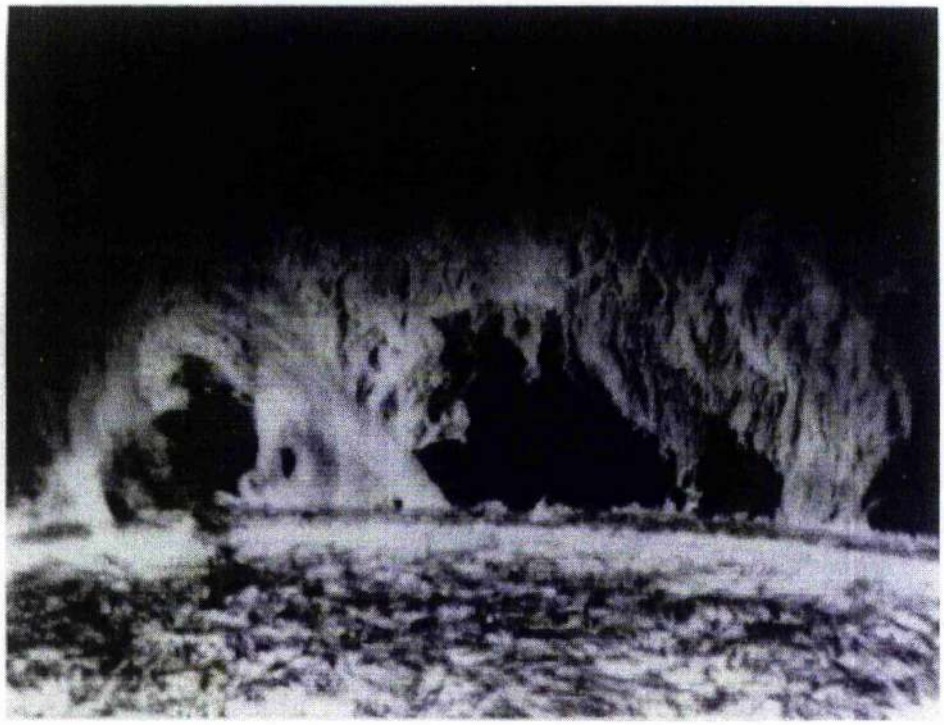

Figure 1.7: A prominence at the limb showing fine structure and feet that reach down to the surface. (Courtesy H. Zirin of Big Bear Solar Observatory)

1.5 Magnetic Fields of the Prominences

The magnetic field plays an important role in the formation and structure of the prominence. They are assumed to thermally insulate the prominence by strongly reducing the cross-field thermal conduction, keeping the prominence from heating up to coronal temperatures. The magnetic field also provides the support of the dense prominence material against gravity high up in the solar atmosphere. The magnetic field can be measured in two different ways based on the Zeeman and Hanlé effects. The first comes from the splitting of atomic levels in a magnetic field and allows the measurement of the line of sight component, while the second is a de-polarisation effect created by Larmor dipole precession coupled to de-excitation by collisions and gives the three components of the field. More details about these effects can be obtained in Tandberg-Hanssen (1974) and Kim (1990). Prominences are observed to lie on the neutral line of the longitudinal magnetic field which separates regions of opposite polarity (Babcock and Babcock, 1955). The field is uniform and more and less horizontal. Observations have shown that the angle between the horizontal magnetic field and the prominence axis is small, ranging from 15° (Tandberg-Hanssen and Anzer, 1970) to 25° (Leroy et al., 1983). The magnetic field strength in prominences lies between $3 - 30$G, typically 5G, and usually increases slightly with height, (Rust, 1967; Leroy, 1977), contrary to the coronal field outside the prominence (Kim, 1990).

Two kinds of magnetic field configurations are associated with prominences, normal and inverse polarity. Both of these configurations feature a closed arcade of magnetic lines overlying the prominence which connects the two regions of opposite polarity magnetic field either side of the prominence. In which in the normal polarity prominence the magnetic field lines pass through the prominence in the same direction as the overlying magnetic field line arcade whereas in the inverse polarity prominence the magnetic field lines pass through the prominence in the opposite direction. Figures 1.8 and 1.9 show these two type of configuration respectively. It is important to note that in a normal polarity prominence, there is a dip in the magnetic field, where the prominence plasma accumulates and is supported against gravity by magnetic tension. Without this dip, the dense prominence plasma would

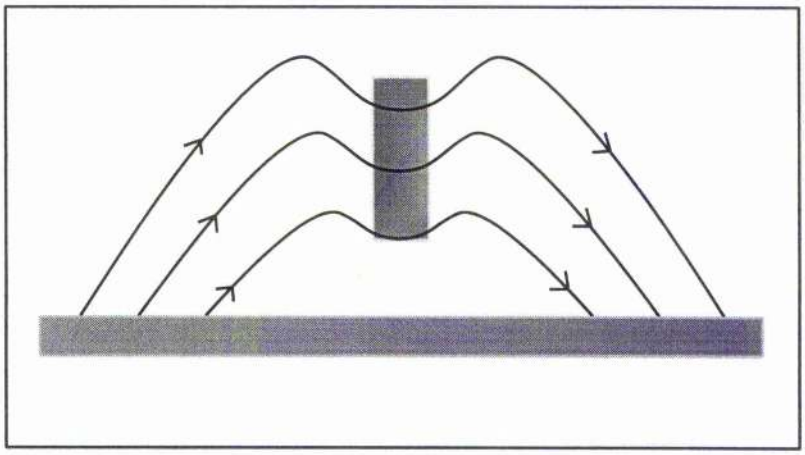

Figure 1.8: Sketch of the magnetic field configuration of the normal polarity prominence.

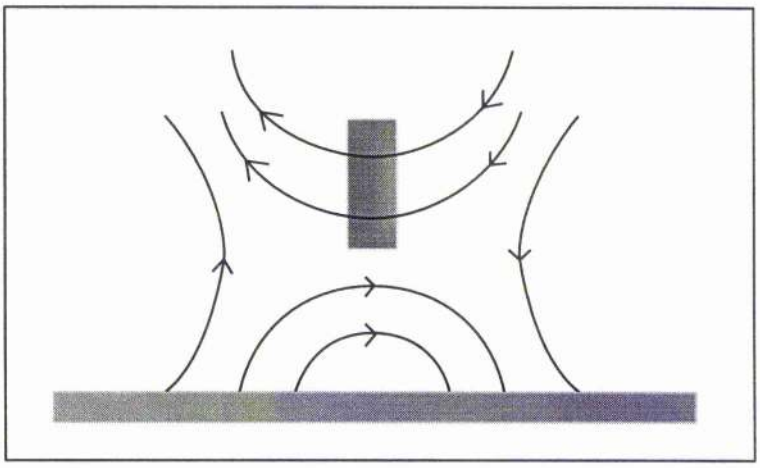

Figure 1.9: Sketch of the magnetic field configuration of the inverse polarity prominence.

just slide down the magnetic field. In studies made by Leroy (1989), he found that prominences with a height above 30Mm had a field strengths between 5 to 10 Gauss and an inverse magnetic configuration. For prominences with height below 30Mm, had a field strengths of about 20G and with normal polarity configuration.

These two configurations are also known as Kippenhahn-Schlüter type for normal polarity and Kuperus-Raadu type for inverse polarity (Leroy, 1989).

1.6 Fine Structure within a Prominence

On the limb it is possible to see that a prominence consists of vertical and sometimes horizontal threads and knots typically 5000km long.

Dunn (1960) gave the first indication of the thickness as less than 300km. Since then, several authors have also estimated the thickness of these threads, for example, Engvold (1976) suggested that the widths ranged between 400-1,500 km. The lifetimes of the fine structures are only of the order of minutes. However, Orral and Zirker (1961), detected no change in shape and brightness in the thread structure over an interval of about 10^4s, and they assumed that individual threads might persist ten times longer.

The filling factor, the fraction of the volume filled by fine structures, is usually taken to be between 0.01 and 0.1 (Engvold, 1976; Simon et al., 1986; Engvold et al., 1990). Engvold (1976) observed that the sizes of some threads and smaller prominence fine scale structures increase with height, this means that the threads are not necessarily of constant width down the prominence. Zirker and Koutchmy (1990), have estimated these threads to be less than 200km wide.

The smallest observed fine structure are of the same size as the instrumental resolution limit, and thread diameters as small as ten kilometers can not be ruled out (Hirayama, 1986). The number of threads per prominences is not clear. Zirker and Koutchmy (1989, 1990) suggest numbers less than twenty, but Zharkova (1989), considers that the number may be higher. Mein et al. (1989) using Doppler measurement, deduce statistically an average of 20 threads along the line of sight. Observations have shown oscillations in these threads (Zhang Yi and Engvold, 1991).

Poland and Mariska (1988), Démoulin et al. (1987), Priest et al. (1991), have discussed a number of mechanism for the formation of fine structure. Recently, Van der Linden (1993), has shown that the formation of field aligned structures can be explained in terms of a radiative instability (Field, 1965), if the thermal conductivity perpendicular to the magnetic field is included. Similar length scales of condensation can also be obtained by including resistivity in the calculation (Ireland et al., 1992).

1.7 Solar Prominence Formation

Martin (1990) has discussed conditions for the formation of prominences as inferred from magnetograms and filtergrams. These conditions are :

-1. A magnetic neutral line, i.e. an inversion line between photospheric fields of opposite magnetic polarity.

-2. A coronal arcade or a helmet above the neutral line.

-3. A sheared magnetic field almost parallel to the neutral line.

-4. An alignment of chromospheric fibrils in the vicinity of the magnetic neutral line.

-5. A long term (hours to days) converging flow of small patches of opposite polarity magnetic flux towards the neutral line.

-6. The cancellation of converging patches of magnetic flux of opposite polarity at the neutral line.

Individually, none of these conditions have proven to be sufficient for prominence formation. However, Martin (1990), proposed that condition 2 and the combination of conditions 5 and 6, if dynamically maintained for a sufficiently long time, will invariably result in the formation of a prominence.

Observations show that during the formation of the filament (prominence observed on the disk) the different parts of the filament do not appear together at the same time (Malherbe, 1989). The formation of the feet occurs in H_α before the appearance of the filament itself, as almost regularly spaced condensations of dark material above the photosphere (Rompolt, 1986). The growth of a large prominence

is thought to begin with the formation of a section on a time-scale of a few hours (Fig 1.10) and in the case of a quiescent prominence, several such sections may develop in half a day or more. These sections are composed of fine structures whose formation time is on the order of a few minutes (Forbes, 1986).

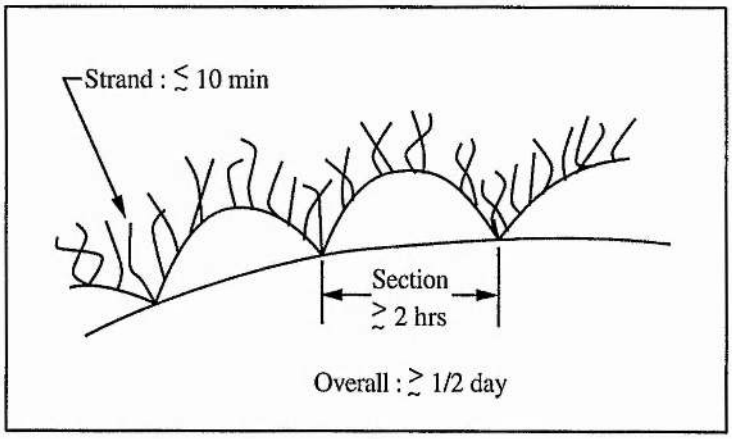

Figure 1.10: Formation times of various prominence features (adapted from Forbes, 1986)

Prominences usually are observed to finally erupt, i.e. to move upwards rapidly and gradually disperse into space. In two thirds of cases, the prominence reforms in the same place, and with the same shape, after a few days (Ballester, 1994). This indicates that many of the above conditions are still present long after the original quiescent prominence has been destroyed (Forbes, 1986).

As mentioned, prominences are denser and cooler than the surrounding plasma and possess a mass of about one tenth of the total corona. A natural question is how this amount of plasma can be concentrated in a relatively small region of the corona. There are three kinds of existing mechanism for the formation of prominences, namely condensation of coronal material, ballistic injection from the chromosphere, and evaporation from the chromosphere with a siphon mechanism. None of these mechanisms alone are likely to be sufficient, since there is not enough coronal plasma to supply the mass, and the direct injection of cold chromospheric plasma has never been observed (Forbes, 1986).

In the first one, the condensation, a small increase of the local density, or alter-

natively, a small decrease in the local temperature, leads to an enhancement of the radiative cooling rate. As a result, the surrounding hot coronal plasma flows towards the depression, leading to a higher density and a faster cooling rate. Therefore, it is the thermal instability (Parker, 1953; Field, 1965) which initiates the condensation of hot coronal plasma (Kuperus and Tandberg-Hanssen, 1967; Smith and Priest, 1977; Choe and Lee, 1992). The second one, cool plasma is launched ballistically from the chromosphere (spicule-type injection) into the corona. This mass may deform the field lines and form a dip where the chromospheric plasma can accumulate (An et al., 1988; Wu et al., 1990). The higher density leads to an enhanced radiative cooling rate and the condensation of the chromospheric plasma as described above. Finally the siphon mechanism, involving the evaporation of chromospheric material, has been studied in order to explain the transport of mass from the chromosphere into prominences (Pikel'ner, 1971; Poland and Mariska, 1986; Antiochos and Klimchuk, 1991).

1.8 Prominence Eruptions

Prominence eruption or a sudden disappearance is a common event in the life of a prominence. Prominences occasionally activate, erupt and disappear. In two thirds of cases, the prominence reforms in the same place and with the same shape after a few days (between 1 to 7 days). A filament disappearance caused by dynamic effect or by heating processes is called either dynamic disappearance (DBd) or thermal disappearance (DBt) respectively (Démoulin and Vial, 1992).

During a DBd the filament erupts by a loss of mechanical equilibrium whereas a DBt indicates that a heating of the cool material to coronal temperatures has taken place and the prominence is no longer visible in Hα (Mouradian et al., 1986).

Generally, the heating is not accompanied with high plasma velocities, and frequently the prominence forms again at low temperatures some hours later (Malherbe, 1989; Zirin, 1988). When a DBd takes place, the whole magnetic structure, with the prominence material is ejected from the upper corona. Once the eruption is in progress, thin threads exhibiting a "coiled" structure become visible within

the prominence. Rompolt (1990) have distinguished two different types of erupting prominences

a) eruption forming a twisted-like flux tube anchored at the solar surface. The erupting arch is nearly fully filled by a cool and dense Hα material.

b) eruption starts from one end of the prominence and progressively detaches prominences footpoints from the solar surface. The opposite prominence end stays anchored and the prominence becomes nearly vertical.

The process starts with constant upwards motions of the order of a few kms^{-1} $(1 - 10kms^{-1})$, then it accelerates to velocities of a few $100kms^{-1}$. Some time later, the prominence forms again, indicating that the previous magnetic field has been reformed (Tang, 1986). On the other hand, in a DBt the plasma is heated in such a way that the hydrogen is completely ionised and the prominence disappears in Hα but becomes visible in UV lines (Mouradian and Soru-Escaut, 1990). No change of the magnetic field occurs. The prominence does not erupt and upward velocities remain very low (less than $10kms^{-1}$) or absent. After sometime, due to the cooling of the plasma, the prominence reappears in the Hα line.

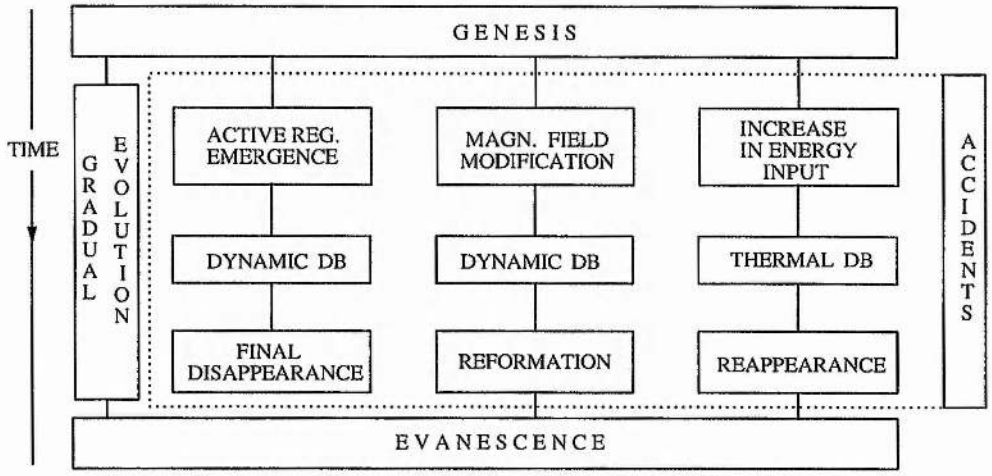

Figure 1.11: The time evolution scheme for solar prominences (adapted from Pojoga et al., 1994).

The development of solar prominences from genesis to evanescence was outlined by Mouradian and Soru-Escaut (1990). Figure 1.11 schematically shows their pro-

posed time development. Observations have shown that most (90%) of the prominences observed for two days or more develop without incident and disappear by a gradual fading and others have dynamical or thermal disappearances (Démoulin, 1993).

1.9 Aims of the Thesis

In this chapter, a brief review of the sun has been presented with some emphasis on observations of coronal loops and prominences.

In Chapter 2, the basic equations are introduced and described in details as well as the equations are reduced in the way that they will be used throughout this thesis.

Chapter 3, 4 and 5 study the equilibrium and evolution of coronal loops when the coronal heating function decay with altitude. In all these chapters the cross-sectional area of the loop (and hence, the magnetic field strength) is constant along the loop.

Chapter 3 investigates the thermal equilibrium at constant pressure of coronal loops. The energy balance equation together with boundary conditions is solved along a magnetic field line and the thermal structure is studied when three parameter are varied. The stability of a uniform solution of the energy equation up to the second order approximation is investigated.

In Chapter 4, the thermal evolution of coronal loop is studied. The effect of gravity is neglected and the evolution of the system is followed under isobaric conditions. It is shown that for given values of the parameter space, especially when the decay length of heating is smaller than a critical value, the loop evolves from a hot plasma to a cool condensation.

Chapter 5 extends the work of Chapter 3 to study the thermal equilibrium of coronal loops with the inclusion of gravity. The effect of gravity along a magnetic field line with or without a magnetic dip is investigated. It is shown that prominence-like solutions exist when gravity is included and the energetics for different type of loops solutions is studied.

In Chapter 6, the principal results of this thesis are summarised and suggestions for further work are presented.

Chapter 2

The Basic Equations

2.1 Introduction

The solar atmosphere is not a simple gas but a plasma. In this state the atoms have split into positive ions and electrons which can flow around freely, so the gas becomes electrically conducting and a current can flow.

Observations have shown that most of the structure and interesting behaviour on the Sun is produced by the magnetic field. Therefore, all this behaviour and structure must be explained by a theory involving the interaction between the plasma and the magnetic field. This has been discussed in the previous chapter.

The aim of this chapter is to describe the basic equations governing this interaction between the plasma and the magnetic field.

The chapter is organised as follows: In Section 2.2 the magnetohydrodynamics (MHD) equations have been presented and the cooling and heating function discussed.

In section 2.3 the MHD equations are reduced to an one-dimensional problem describing a low beta plasma (β) in the solar corona.

2.2 Basic Equations

The behaviour of solar plasma is governed by the MHD equations. It consists of the study of the interaction between a magnetic field and the plasma, treated as a single continuous fluid and a conducting gas, where the length-scale of the system is much

larger than the mean free path of the particles.

The electromagnetic equations are given by Maxwell's equations

$$\nabla \times \mathbf{B} = \mu \mathbf{j} + \frac{1}{c^2}\frac{\partial \mathbf{E}}{\partial t} \tag{2.1}$$

$$\nabla \cdot \mathbf{B} = 0, \tag{2.2}$$

$$\nabla \times \mathbf{E} = -\frac{\partial \mathbf{B}}{\partial t}, \tag{2.3}$$

and

$$\nabla \cdot \mathbf{E} = \frac{\rho^*}{\epsilon}, \tag{2.4}$$

where $\mathbf{E}$ is the electric field and $\mathbf{B}$ the magnetic in the presence of a current density $\mathbf{j}$ and a charge density ρ^*, $c = (\mu\epsilon)^{1/2}$ is the speed of light, $\mu(= 4\pi \times 10^{-7}\mathrm{Hm}^{-1})$ is the magnetic permeability and $\epsilon(\approx 8.854 \times 10^{-12}\mathrm{Fm}^{-1})$ is the electric permittivity.

Equation (2.4) is seldom used in the context of solar physics and allows one to calculate the charge density once the electric field is known.

To derive the form of the electromagnetic equations as they appear in the MHD theory one must take into account that all velocities are much less than the speed of light, so that relativistic effects are negligible.

By replacing the operator ∇ and $\partial/\partial t$ by $1/l$ and v/l (where l and l/v represent characteristic length and time of variations of the system), one notes that the two terms in equation (2.3) have magnitudes of order of E/l and vB/l, which implies that E is the order of vB . Thus, the displacement current in Equation (2.1) is smaller than the term on the left-hand side by a factor v^2/c^2 and can be eliminated from this expression which then reduces to

$$\nabla \times \mathbf{B} = \mu \mathbf{j}, \tag{2.5}$$

i.e.,

$$\mathbf{j} = \frac{1}{\mu}\nabla \times \mathbf{B}. \tag{2.6}$$

The last form can be used to calculate the current density in terms of **B**.

The Ohm's law for a classical fluid with scalar conductivity σ is

$$\mathbf{j} = \sigma\left(\mathbf{E} + \mathbf{v} \times \mathbf{B}\right), \tag{2.7}$$

where $\mathbf{v}$ is the velocity of the fluid element with respect to an inertial frame of reference in which the electric field is **E**.

Combining equations (2.3), (2.6) and (2.7) one obtains the induction equation

$$\frac{\partial \mathbf{B}}{\partial t} = \nabla \times (\mathbf{v} \times \mathbf{B}) - \nabla \times (\eta \nabla \times \mathbf{B}), \tag{2.8}$$

with

$$\eta = \frac{1}{\mu\sigma} = 5.2 \times 10^7 \log\Lambda \; T^{-3/2} \mathrm{m}^2\mathrm{s}^{-1}, \tag{2.9}$$

the magnetic diffusivity, and $\log\Lambda$ the Coulomb logarithm.

The first term on the right hand side of equation (2.8) describes the advection of the magnetic field by fluid motions, whereas the second term represents the diffusion of **B** through the plasma.

If η is taken uniform, then equation (2.8) reduces to

$$\frac{\partial \mathbf{B}}{\partial t} = \nabla \times (\mathbf{v} \times \mathbf{B}) + \eta \nabla^2 \mathbf{B}. \tag{2.10}$$

The ratio of the two terms on the right hand side of (2.10) is known as the magnetic Reynolds number, R_m, defined as

$$R_m = \frac{vl}{\eta}. \tag{2.11}$$

If $R_m \gg 1$, then (2.10) simplifies to

$$\frac{\partial \mathbf{B}}{\partial t} = \nabla \times (\mathbf{v} \times \mathbf{B}). \tag{2.12}$$

In this case, the magnetic flux through a closed contour moving with the plasma is constant, which implies that the lines of magnetic force move with the plasma and are said to be frozen into the plasma. If $R_m \ll 1$, then (2.10) becomes

$$\frac{\partial \mathbf{B}}{\partial t} = \eta \nabla^2 \mathbf{B}, \tag{2.13}$$

the well known diffusion equation. In this case, the field diffuses away on a timescale

$$\tau_d \sim \frac{l^2}{\eta}. \tag{2.14}$$

Now the equations (2.2) and (2.8) can give $\mathbf{B}$ if $\mathbf{v}$ is known.

The above set of electromagnetic equations have to be supplemented with a proper macroscopic description of the plasma, given by the hydrodynamic equations namely, continuity of mass, momentum and energy equations. The first one is written as

$$\frac{\partial \rho}{\partial t} + \rho \nabla \cdot \mathbf{v} + \mathbf{v} \cdot \nabla \rho = 0, \tag{2.15}$$

where ρ is the plasma density.

The momentum equation of a plasma under the action of pressure gradients, magnetic forces, gravity and others forces is

$$\rho \left[\frac{\partial \mathbf{v}}{\partial t} + (\mathbf{v} \cdot \nabla) \mathbf{v} \right] = -\nabla p + \rho \mathbf{g} + \mathbf{j} \times \mathbf{B} + \mathbf{F} \tag{2.16}$$

where p is the plasma pressure, $\mathbf{g}$ is the acceleration due to gravity and $\mathbf{j} \times \mathbf{B}$ is the Lorentz force per unit volume. $\mathbf{F}$ represents any further forces(e.g. viscosity) which are usually assumed to be negligible in the solar atmosphere and D/Dt is the convective derivative given by

$$\frac{D}{Dt} = \frac{\partial}{\partial t} + v \cdot \nabla. \tag{2.17}$$

The Lorentz force is normal to the field lines and can be decomposed as the sum of the terms $-\nabla(B^2/2\mu)$ and $(\mathbf{B} \cdot \nabla)\mathbf{B}/\mu$. The first term represents a magnetic pressure gradient where the magnetic pressure is given by $B^2/2\mu$. The second term is the tension force, with magnitude B^2/μ, analogous to the tension of an elastic string and is therefore called magnetic tension.

A useful parameter is the plasma beta defined as

$$\beta = \frac{2\mu p}{B^2}, \tag{2.18}$$

which measures the ratio of the gas pressure to magnetic pressure. The so-called low-β plasma is when $\beta \ll 1$, and refers to a configuration in which the magnetic field force $\mathbf{j} \times \mathbf{B}$ dominates over the pressure gradient term $(-\nabla p)$ in Equation (2.16).

In addition to these equations there is the equation of state which expresses the relationship between the gas pressure, the density and the temperature, namely

$$p = \frac{\mathcal{R}}{\tilde{\mu}} \rho T, \tag{2.19}$$

where $\mathcal{R}$ is the gas constant $(= 8.3 \times 10^3)$ and $\tilde{\mu}$ is the mean molecular weight (which has been taken as 0.6 in the solar corona). The energetics are governed by an energy equation, of the form

$$\frac{\rho^\gamma}{\gamma - 1} \frac{D}{Dt} \left(\frac{p}{\rho^\gamma} \right) = \nabla \cdot (\kappa \nabla T) - \mathcal{L}(\rho, T) + \frac{\eta}{\mu} |\nabla \times \mathbf{B}|^2, \tag{2.20}$$

where γ is the adiabatic index $(= 5/3)$, κ the thermal conduction tensor, $\mathcal{L}$ the generalised energy loss function per unit mass with energy gains defined as negative losses, and $\frac{\eta}{\mu} |\nabla \times \mathbf{B}|^2$ is the ohmic dissipation.

The anisotropic thermal conduction term is rewritten in terms of the coefficients of thermal conductivity parallel $(\kappa_\parallel)$ and perpendicular $(\kappa_\perp)$ to the magnetic field

$$\nabla \cdot (\kappa \nabla T) = \mathbf{B} \cdot \nabla \left(\kappa_\parallel \frac{\mathbf{B} \cdot \nabla T}{B^2} \right) + \nabla \cdot \left(\kappa_\perp \frac{\mathbf{B} \times (\nabla T \times \mathbf{B})}{B^2} \right), \tag{2.21}$$

where for sufficiently strong fields (Braginskii, 1965)

$$\kappa_\parallel = \kappa_\parallel(T) \approx 1.8 \times 10^{-10} (\log \Lambda)^{-1} T^{2.5} \mathrm{Wm^{-1}K^{-1}}, \tag{2.22}$$

and

$$\kappa_\perp = \kappa_\perp(\rho, T, B) \approx 8.2 \times 10^{-33} (\log \Lambda)^2 n^2 B^{-2} T^{-3} \kappa_\parallel, \tag{2.23}$$

where n the number density. In these formulae n is measured in $\mathrm{m^{-3}}$, temperature in Kelvin and the magnetic field in Tesla. Typically in the solar corona $\log \Lambda \approx 22$

and $\kappa_\perp \approx 10^{-12}\kappa_\parallel$ (Spitzer, 1962). Parallel thermal conduction is mainly due to electrons, whilst perpendicular thermal conduction is due to ions.

In the energy loss-gain function, an optically thin radiative loss term and an unspecified coronal heating function are included. It describes how the plasma is heated and how it cools. The energy loss-gain function can be written as

$$\mathcal{L} = C - H \tag{2.24}$$

where C is the radiative loss function and H heating function per unit volume.

For most plasmas, $\mathcal{L}$ will depend on the usual thermodynamics quantities, such as temperature; it may also depend upon the chemical composition of the plasma, its surroundings, its position and also upon the magnetic field.

The radiative loss function C can be defined as loss of internal energy by a unit volume per second (i.e. the amount of radiation emitted by the plasma from bound-bound, bound-free, and free-free transitions at a given temperature). It has been estimated by several authors such as Pottash (1965), Cox and Tucker (1969), Tucker and Koren (1971), McWhirter et al (1975), Raymond and Smith (1977). An analytical fit to the radiation was made by Hildner (1974) and is described by

$$C = n^2 Q(T) = \frac{\rho^2}{m_H^2} Q(T) \tag{2.25}$$

being

$$Q(T) = \chi T^\alpha \tag{2.26}$$

where χ and α are piecewise constant function of temperature and n is the ion number density. The values of χ and α are given in Table 2.1.

As can be seen from the form of the plasma cooling given by equation (2.25) and Figure 2.1 there is a peak at around 10^5K, such that the loss function is smaller at higher and lower temperatures.

The shape of this function is important to drive a radiative instability because Q decreases with temperature above this peak. The effect of this function will be discussed in section 4.1

Temperature Range (K)	χ	α
$< 1.5 \times 10^4$	4.92×10^{-67}	7.4
$1.5 \times 10^4 - 8.0 \times 10^4$	1.20×10^{-43}	1.8
$8.0 \times 10^4 - 3.0 \times 10^5$	8.00×10^{-35}	0.0
$3.0 \times 10^5 - 8.0 \times 10^5$	3.94×10^{-21}	-2.5
$8.0 \times 10^5 - 10^7$	5.51×10^{-30}	-1.0

Table 2.1: The constants χ and α for the radiative loss function $Q(T) = \chi T^{\alpha}$ (From Hildner, 1974)

The heating function in equation (2.20) represents the source of energy which is taken into account in order to balance the radiative and conductive losses. These losses have been estimated by Withbroe and Noyes (1977) in the solar corona to be:

Quiet region	300 Wm^{-2}
Active region	$(0.5 - 1) \times 10^4$ Wm^{-2}
Coronal hole	800 Wm^{-2}

In the corona this source of energy is not well known. Different forms of heating are possible such as the dissipation of acoustic waves generated in the convection zone (Kuperus, 1969), the damping of Alfvén waves (Wentzel, 1974), the ohmic dissipation of induced coronal currents (Tucker, 1973), and the possibility that the corona is heated by an episodic process due to microflares and nanoflares (Parker 1988, 1989) rather than continually has also been considered. However, so far observations have been unable to discriminate between them. Possibly several heating mechanisms may be operating simultaneously which would make discrimination much more difficult.

Klimchuk and Porter (1995) divide them into two general categories which are dissipation of waves and dissipation of stressed coronal magnetic fields.

Kuperus et al (1981), Wentzel (1981), Priest (1982), Hollweg (1990), Browning (1991), and Zirker (1993) have reviewed extensively the different heating theories.

Generally it is accepted that energy comes from the sub-photospheric region and it is also generally accepted that the magnetic field plays an important role in the transport and dissipation of this energy.

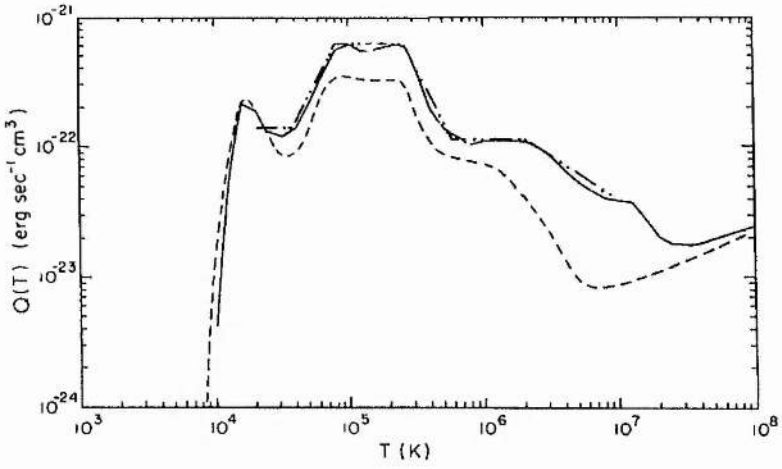

Figure 2.1: The radiative loss function $Q(T)$ as a function of the temperature as estimated by McWhirter, et al. (1975) [__]; Raymond (1978) [—]; and an analytic fit given by Rosner et al. (1978) [..–..].

Given that none of the present coronal heating theories have been accepted as the final theory explaining the heating mechanism in the corona, the heating will be assumed to be explicitly dependent on the spatial position s. The energy input is taken to have the general form

$$H = h_0 f(s) \rho^{\nu} \tag{2.27}$$

where the function $f(s)$ expresses the spatial variations in H and h_0 is the heat deposition at the base of the loop. This form contains both asymptotic cases, firstly, constant heating per unit volume, $f(s) \equiv 1$ and $\nu = 0$, and secondly, constant heating per unit mass, $f(s) \equiv 1$ and $\nu = 1$ (Antiochos and Noci 1986).

In the present work $\nu = 0$ and the function $f(s)$ is given by

$$\exp\left(-\frac{s}{s_H}\right) \tag{2.28}$$

where s_H is the spatial decay-length of the heating source. This means that more heat is provided to the footpoint rather than the summit.

This form of the heating is among of the models of heat interruption used by Pikel'ner (1971), Rosner et al (1978), Mok et al (1990), Antiochos and Klimchuk (1991) and Van Hoven et al (1992).

Rosner et al (1978) discussed an exponentially varying heating function ($H = h_0 \exp(-s/s_H)$) and concluded that it would be acceptable if the decay length of the heating s_H is not small when compared with the loop length.

The above heating function qualitatively represents the transformation (dissipation) of some upward travelling energy flux. As for example, the mechanical energy supply from the photosphere to the corona may be dissipated due to various local events, such as, the local plasma inhomogeneities or turbulence (through phase mixing of Alfvén waves, e.g. Heyvaerts and Priest, 1983; Hood et al, 1996).

Owing to the deposition of energy in the plasma along the upward path, the upper part of the loop experiences a decay of energy supply as a result of the advanced rate of absorption locally. However, it must be stressed, that the decay rate depends on the local conditions as well as on the not well understood heating mechanism; this will be treated as a free parameter in this thesis.

This functional form of the heating was used by Serio et al (1981), Mok et al (1990), and Woods et al (1990) in their modelling on solar coronal structures or formation of solar prominences.

Other different forms of $f(s)$ have also been taken, for example, Antiochos and Klimchuk (1991) in their simulation of prominence formation considered a gaussian function.

The form of an exponential heating function can be justified for the dissipation of Alfvén waves in an uniform medium due to viscosity.

Combining the linearised momentum equation with the induction equation a dispersion relation can be obtained as (cf. Roberts, 1985; see also Appendix A):

$$k_s^2 v_A^2 - \omega^2 = i\omega\nu k_s^2 \tag{2.29}$$

where k_s is the complex wave number of propagation in the direction of the magnetic field (s direction), ω is the wave frequency, $v_A^2 = B_0^2/\mu\rho_0$ is the speed of Alfvén waves and ν is the coefficient of kinematic viscosity.

For $\nu\omega/v_A^2 \ll 1$ the above dispersion relation yields approximately the complex wave number

$$k_s \approx \frac{\omega}{v_A}\left(1 + \frac{1}{2} i \frac{\omega\nu}{v_A^2}\right), \tag{2.30}$$

which gives a heating term of the form

$$H \sim \exp\left[-\frac{s}{s_H}\right], \tag{2.31}$$

where $s_H = v_A^3/\omega^2\nu$.

However, although the above simple example demonstrates an exponential decay in the heating due to wave damping, it is known to be inefficient for heating the solar corona. This is because of the fact that in solar corona the large Alfvén speed and small kinematic viscosity yields a very large value of $s_H = v_A^3/\omega^2\nu$, which is larger than the typical length scale of the solar corona structure.

Special wave damping mechanism such as, the phase mixing of Alfvén waves (cf. Heyvaerts and Priest, 1983; Hood et al, 1996) are therefore, proposed as more efficient heating mechanism in solar corona. The principle behind phase mixing is that the Alfvén waves propagating in an inhomogeneous medium, will develop different wavelengths on neighbouring field lines causing the Alfvén waves to move out of phase with respect to each other. As a result large spatial gradients build up in the direction of the inhomogeneity, so that dissipation comes into play, allowing the energy in the wave to heat the plasma.

When considering phase mixing alone, the functional form of heating rate still follows an exponential form indicating a localised heating at the footpoint of the loop, such as in our form in equation (2.28). The spatial variation of the heating rate is however much faster than equation (2.28) and is given by

$$H \sim \exp\left[-\left(\frac{s}{s_H}\right)^3\right] \tag{2.32}$$

As is mentioned above, the solar coronal situation is much too complex to consider a single heating mechanism as the sole mechanism responsible for solar coronal heating.

In such a complex situation there is no reason to favour some particular form of heating function such as in Equation (2.32) that is based on a particular heating mechanism. In this thesis, we therefore use a general exponential form of heating form such as equation (2.28) as a phenomenological heating model without any further justification. We however, would come back to the particular heating form of Equation (2.32) only briefly in Chapter 6 in order to get preliminary results for future work.

Figure 2.2 shows the dependence of the heating with the position. The different curves are labelled with the variable s_H. When the decay-length of the heating s_H is very large the heating considered in the system is uniform whereas s_H is small the heating will be concentrated to the footpoint. Now, one can see that the variation of heating through this parameter s_H covers a range values of the heating with different spatial dependences.

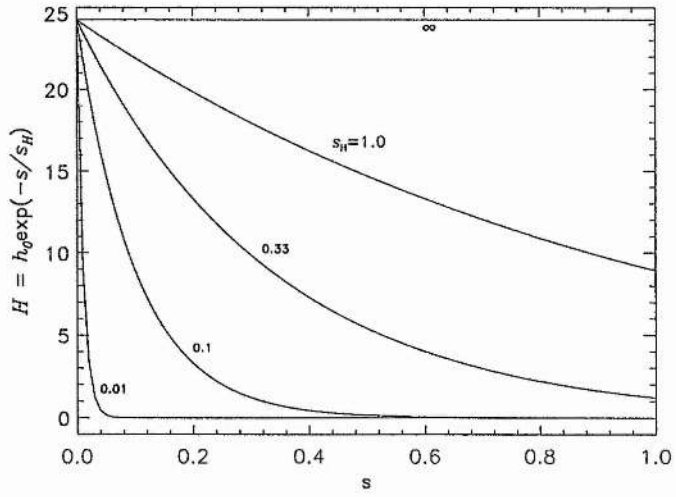

Figure 2.2: Form of the spatial dependence of the heating function.

2.3 Reduced Equations

As mentioned in Chapter 1, the magnetic field plays an important role in the solar corona, producing in it a complex network of individual loop-like structures. The coronal plasma beta (β) is much smaller than unity (typical value is $\sim 10^{-2}$). Therefore, for this thesis, one can assume that a strong magnetic field confines the plasma so that it provides a symmetric loop geometry that channels the mass flow and heat flux. So, that the governing equation of this system need only be solved in one dimension. Thus, if one takes s to be the position measured along a magnetic field line, with constant cross-sectional area, the equations for mass, momentum, and energy conservation reduce to

$$\frac{\partial \rho}{\partial t} + \frac{\partial}{\partial s}(\rho v) = 0, \tag{2.33}$$

$$\rho\left(\frac{\partial v}{\partial t} + v\frac{\partial v}{\partial s}\right) + \frac{\partial p}{\partial s} = -\rho g(s), \tag{2.34}$$

$$\frac{1}{\gamma - 1}\left(\frac{\partial p}{\partial t} + v\frac{\partial p}{\partial s}\right) + \frac{\gamma}{\gamma - 1}p\frac{\partial v}{\partial s} + \mathcal{L}(\rho, T, s) - \frac{\partial}{\partial s}\left(\kappa\frac{\partial T}{\partial s}\right) = 0, \tag{2.35}$$

$$p - \frac{\rho}{\tilde{\mu}}\mathcal{R}T = 0. \tag{2.36}$$

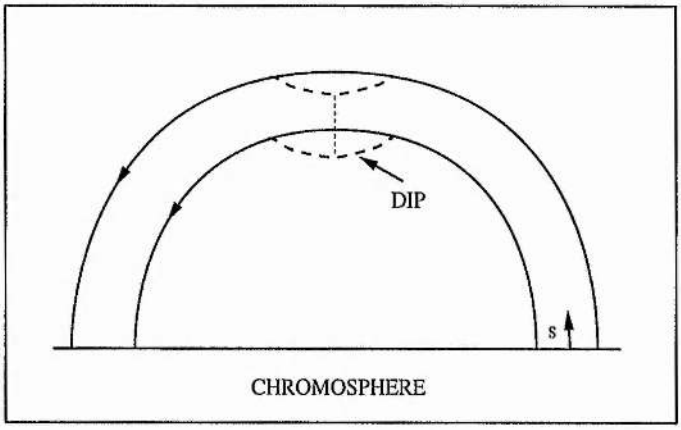

Figure 2.3: Coronal loop geometry showing the dip where the distortion is formed when condensation occurs. The coordinate s is along the magnetic field.

The gravitational acceleration g is assumed to be a function of s since it is the component of the gravitational force along the magnetic field and for our model contains two terms

$$g = g_0 \cos\frac{\pi s}{2L} + g_d(s). \tag{2.37}$$

The first term of (2.37) assumes that the confining magnetic field has a semicircular shape, where $g_0 = 2.74 \times 10^2 \mathrm{ms}^{-2}$ is the solar-surface gravity. The second term g_d is due to the dip (Figure 2.3) which is introduced to simulate the fact that the magnetic field will be distorted where the condensation occurs (Mok et al, 1990).

The equations presented in this section correspond to the reduced equations and will be used throughout the following chapters with the assumption that the radiative losses can be described by an optically thin steady state treatment and the coronal heating having a spatial dependence.

Chapter 3

The Thermal Equilibria of Uniform-Pressure Coronal Loops

3.1 Introduction

It was mentioned in Chapter 1 that observations of the solar corona in X-ray and EUV have shown that it consists of a large number of loops which outline the coronal magnetic field in form of magnetic flux tubes that confine the plasma. Often these loops are observed to form arcades and other structures. Also, these coronal loops possess lifetimes which are frequently greater than the timescales defined by thermal conduction and radiation losses. These time scales suggest that coronal loops exist in a quasi-static state which suggests the presence of some form of steady energy input. In consequence, several types of coronal loop structure have been proposed based on a static model in which the mechanical energy deposited into each volume element is exactly balanced by a radiative loss flux (F_R) and by conductive energy flux (F_c) into (or out of) the element (Figure 3.1).

Since energy or mass transport across the loop is strongly inhibited by the magnetic field the conduction is assumed to take place only along the field lines.

Rosner et al. (1978), using an order of magnitude analysis, derived scaling laws between the loop length, the plasma pressure, and the maximum temperature along the loop. They assumed that the base conductive flux vanishes at a particular temperature and the flux also vanishes at the loop summit, from symmetry arguments.

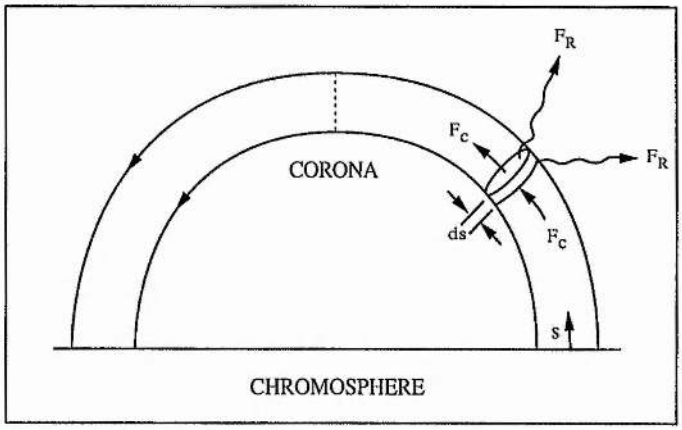

Figure 3.1: Coronal loop geometry. The coordinate s is along the magnetic field. A volume element dV having dimension ds along the magnetic field is shown with radiative (F_R) and conduction fluxes (F_c) indicated schematically.

The scaling laws derived have the form

$$T_s \approx 1.4 \times 10^3 (pL)^{1/3},$$

for the summit temperature and the heating

$$h \approx p^{7/6} L^{-5/6}.$$

Craig et al (1978) also demonstrated that a relationship must exist between the thermodynamic properties of a loop and its length, when the pressure is constant, of the form

$$T_s^{9/4} \approx N_s L.$$

Hood and Priest (1979) solved the problem of thermal equilibrium along a coronal loop when gravity is neglected. They found the existence of cool solutions with summit temperatures below 10^5 K when either the external gas pressure p, or the length L of the field lines increases (due to motions of the footpoints) or the heating decreases and suggest that they may explain the existence of active region prominences.

Priest and Smith (1979) applied these techniques to an arcade consisting of a succession of loops. Gravitational effects were considered by Vesecky et al (1979),

Wragg and Priest (1981a,b; 1982) and many others but gravitational effects will be studied in more detail in Chapter 5.

Hood and Anzer (1988) studied the problem of thermal equilibrium qualitatively. They used a phase plane diagram approach to identify the different types of solution that are possible. The advantage of this technique was that their conclusions were not sensitive to the actual choice of boundary condition adopted, which only determines the actual contour.

Steele and Priest (1990a) confirmed and extended the work of Hood and Anzer (1988) by seeking numerical solutions to the different types of loops and determined the parameter regimes for which they exist. Four different kinds of loops may exist, namely hot loops, warm loops, hot-cool loops and cool loops. They defined regions of the parameter space in which each type of solution occurs depending on both a physical parameter related to the length of the loop and the heating. Regions with only one solution have either a hot or a cool solution; two solution regions have one hot and one hot-cool; a three solution region has one hot solution, one warm and one cool solution. There are also regions in the solution space with no physically realistic solutions.

3.2 Equation of Thermal Equilibrium and Boundary Conditions.

Before presenting the basic equations for thermal equilibrium a dimensional analysis is made in order to show that static modelling is reasonable for the coronal atmosphere. From the energy equation one can calculate the conductive time-scale. If L_0 denotes the scale length of the plasma then

$$\tau_{cond} = \frac{p_0 L_0^2}{\kappa_{\|} T_0^{7/2}}. \tag{3.1}$$

Then, for typical values in the corona: $T_0 = 10^6$K, $\rho_0 = 2.26 \times 10^{-12}$kgm^{-3} and $L_0 = 10^7$m, $\tau_{cond} \approx 312.6$s.

In the same way, when Q is approximated by $Q = \chi T^{\alpha}$ where χ and α are the

coronal values given by Hildner, the radiative time scale is given by

$$\tau_{rad} = \frac{p_0}{\chi \rho_0^2 T_0^\alpha}. \tag{3.2}$$

Hence, taking the same parameters as before yields $\tau \approx 3107$s.

Comparing these two timescales with the observed lifetimes of coronal loops of hours to days it is clear that they are shorter. Therefore, a quasi-static model with a steady input of energy can be considered. Since coronal loops experience only a slow change, the equations (2.33)-(2.36) for a static coronal loop can be simplified to

$$\frac{dp}{ds} = -\frac{\tilde{\mu} p}{\mathcal{R} T} g(s), \tag{3.3}$$

$$\frac{d}{ds}\left(\kappa \frac{dT}{ds}\right) = \left(\frac{\tilde{\mu} p}{\mathcal{R}}\right)^2 \chi T^{\alpha-2} - h(p, T, s), \tag{3.4}$$

where s represents the distance along the loop, $g(s)$ is the component of gravity along the loop, p is the gas pressure, T is the plasma temperature, h is the unknown heating function that may depend on p, T and s, and κ is the coefficient of thermal conduction, i.e. $\kappa \approx 10^{-11} T^{5/2}$ Wm^{-1}K^{-1} Spitzer (1962). The first term on the right-hand side of equation (3.4) is the radiative loss term, where $\chi T^{\alpha-2}$ is the piecewise continuous function given by Hildner (1974) as was pointed out in Chapter 2.

Equation (3.3) expresses the balance between gravity and the pressure gradient along the loop, and equation (3.4) represents the balance between the energy gain due to coronal heating, the losses due to radiation, and the gains or losses due to thermal conduction.

Equations (3.3) and (3.4) can be written in dimensionless form by setting

$$\tilde{s} = s/L_0, \qquad \tilde{T} = T/T_0 \qquad \text{and} \qquad \tilde{p} = p/p_0 \tag{3.5}$$

in which T_0, p_0 are taken at typical coronal or chromospheric values, and L_0 is the half-length of the loop. Therefore

$$\frac{d\tilde{p}}{d\tilde{s}} = -\frac{\tilde{p}}{\tilde{T}} \tilde{g}(\tilde{s}), \tag{3.6}$$

$$\frac{d}{d\tilde{s}}\left(\tilde{T}^{5/2} \frac{d\tilde{T}}{d\tilde{s}}\right) = L_*^2 \left[\tilde{p}^2 \tilde{\chi} \tilde{T}^{\alpha-2} - \tilde{h}\right], \tag{3.7}$$

where

$$\begin{aligned} \tilde{g}(\tilde{s}) &= \frac{\tilde{\mu} L_0}{\mathcal{R} T_0} g_0 g(s), \\ L_*^2 &= L_0^2 \frac{\tilde{\mu}^2 p_0^2 \chi_0 T_0^{\alpha_0 - 11/2}}{\mathcal{R}^2 \kappa_0}, \\ \tilde{h} &= \frac{\mathcal{R}^2 h(\tilde{p}, \tilde{T}, \tilde{s})}{\tilde{\mu}^2 p_0^2 \chi_0 T_0^{\alpha_0 - 2}}, \\ \tilde{\chi} &= \frac{\chi T_0^{\alpha}}{\chi_0 T_0^{\alpha_0}}. \end{aligned} \tag{3.8}$$

In order to solve equations (3.6) and (3.7), boundary conditions must be provided. It is assumed that the temperature $\tilde{T} = \tilde{T}_b$ and pressure $\tilde{p} = \tilde{p}_b$ at the footpoints of the loop are fixed and by symmetry, there is a zero temperature gradient at the loop summit. There are other choices of boundary conditions for example $d\tilde{T}/d\tilde{s} = 0$ at the base with $\tilde{p}_b$ adjusting to the value necessary for a solution to exist (Vesecky et al 1979, Rosner et al 1978). Since the mechanism of coronal heating $\tilde{h}$ is unknown, its form is assumed (discussed in Chapter 2) to be

$$\tilde{h} = h_* \exp\left(-\frac{\tilde{s}}{s_*}\right), \tag{3.9}$$

where $\tilde{s} = 0$ corresponds to the base of the loop (footpoint) and the dimensionless parameters h_* an s_* are given by

$$\begin{aligned} h_* &= \frac{\mathcal{R}^2 h_0}{\tilde{\mu}^2 p_0^2 \chi_0 T_0^{\alpha_0 - 2}}, \\ s_* &= \frac{s_H}{L_0}. \end{aligned} \tag{3.10}$$

A similar heating function for the decay from the other footpoint is given by

$$\tilde{h} = h_* \exp\left(-\frac{1 - \tilde{s}}{s_*}\right). \tag{3.11}$$

In this case the summit is located at $\tilde{s} = 0$ and the footpoint at $\tilde{s} = 1$.

In (3.6) the equation for $\tilde{g}(\tilde{s})$ denotes the ratio of loop length to base scale height. For typical loop heights and temperatures, the gravitational scale height

$\Lambda = \mathcal{R}T_0/\tilde{\mu}g_0$ is large compared to the size of the loop structure then, if

$$\tilde{g} \ll 1, \tag{3.12}$$

the force balance equation (3.3) reduces to the result that the pressure is approximately constant throughout the loop, and, therefore, the plasma structure is only determined by energy balance.

So, with gravity neglected equation (3.7) simplifies to

$$\frac{d}{ds}\left(T^{5/2}\frac{dT}{ds}\right) = L_*^2\left[p^2\chi T^{\alpha-2} - h_* \exp\left(-\frac{s}{s_*}\right)\right], \tag{3.13}$$

where all tildes have been removed for convenience. In this equation three dimensionless parameters are involved namely L_*, the ratio of the conduction to radiation timescales, h_*, the ratio of heating to radiation and s_*, the ratio of the length of the loop to the decay-length of the heating.

Equation (3.13) is solved numerically, together with the boundary conditions

$$\begin{aligned} \frac{dT}{ds} &= 0 \qquad \text{at} \qquad \textit{summit}, \\ T &= T_b \qquad \text{at} \qquad \textit{footpoints}. \end{aligned} \tag{3.14}$$

However, before solving the above equations in full, it is helpful to get qualitative information concerning their behaviour, by considering a phase diagram (see Figure 3.2) where additionally the heating is assumed to be a constant (Hood and Anzer, 1988; Steele and Priest, 1990a).

Setting

$$V = T^{5/2}\frac{dT}{ds}, \tag{3.15}$$

equation (3.13) becomes

$$\frac{dT}{ds} = VT^{-5/2}, \tag{3.16}$$

$$\frac{dV}{ds} = L_*^2\left[p^2\chi T^{\alpha-2} - h_*\right], \tag{3.17}$$

with critical points defined by the conditions

$$V = 0 \qquad \text{and} \qquad T = \left[\frac{h_*}{p^2\chi}\right]^{\frac{1}{\alpha-2}} = T_{crit}.$$

Figure 3.3 shows the variation with temperature of $\chi T^{\alpha-2}$ (full lines) and two values of h_* indicated by broken lines. Where the full and broken lines cross (i.e. the two terms on the right hand side of equation (3.17) are equal) a critical point exists. From Figure 3.3, is apparent that when $h_* < 10^{4.4}$ two different values of T_{crit} are found, a saddle point at T_c and a centre point at T_h (see Appendix B).

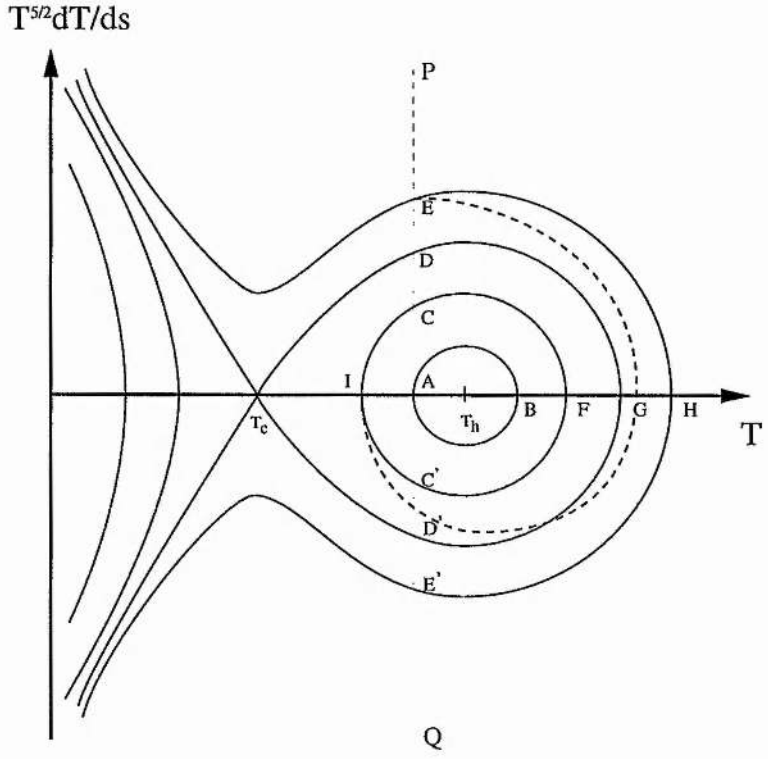

Figure 3.2: The form of the phase plane for the solution of Energy Balance Equation. The vertical line illustrates a typical base temperature and the dashed line correspond to a solution when h has a spatial dependence $\sim \exp(-s/s_*)$.

When $h_* > 10^{4.4}$ no critical point exists. If $h_* < 10^{4.4}$ the saddle point T_c lies at a value of T less than $T_b = 10^{-2}$ (in units of $2 \times 10^6 K$). Therefore, the footpoint lies along the line PQ and, as the temperature gradient is assumed to be positive, it lies

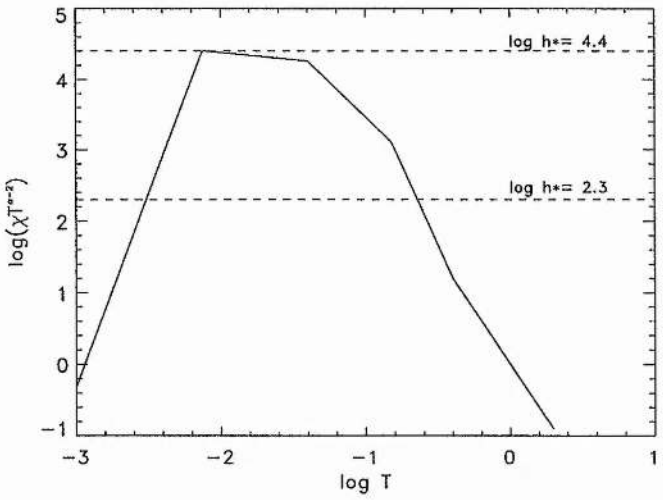

Figure 3.3: The relative strengths of the radiation loss term (full line) and the heating term (broken line) in equation (3.7).

between point A and point E. The point corresponding to the loop summit (where $dT/ds = 0$) will lie on the T axis (Figure 3.2).

Starting from point A (or a point very close to it) on the phase diagram one finds a hot summit at point B (this solution is known as a hot solution) and a cool summit when contour is extended onwards around the centre point and back to A. Thus, the loop has a cool summit but is hot along part of its length, it is referred to as a hot-cool solution (Hood and Anzer 1988 and Steele and Priest 1990a).

Beginning at point C gives a hot solution with a summit at point F and a hot-cool solution with the summit at point I. This existence of both a hot solution and a hot-cool solution will occur for all footpoints between A and D where the hot-cool solution at point T_c has the coolest possible summit temperature for the particular value of h_*. Starting from higher temperature gradient such as at point E, one finds a hot solution with summit at point H but no hot-cool solution. Other possible solutions can be found, such as a cool and warm solution. They are described in Steele and Priest (1990a).

When h_* is changed from a value where two critical points exist to another smaller value, the two new critical points are separated from each other so that the temperature at the saddle point, T_c, and the temperature T_h decrease and increase their values respectively. This effect can be seen in Figure 3.4 where the phase

diagram with dashed lines corresponds for a smaller value in h_* (only closed contours are shown). Therefore, contours starting with some temperature gradient outside the separatrix in the solid lines phase diagram, are inside the separatrix in the dashed lines phase diagram, such as A moving onwards to B, then one applies an instant variation of the heating to a smaller value in h_* will start moving along the new contours (dashed lines) that are now inside of the separatrix of the new phase diagram, reaching the point C. The solution at this point is hot. However, a cool summit is found when the contour is extended onwards to D.

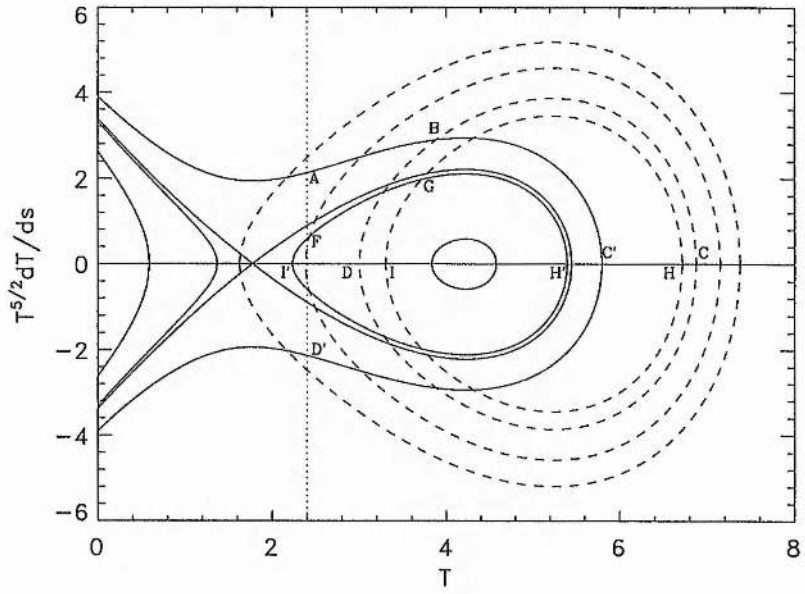

Figure 3.4: The form of the phase plane diagram for two different values of h_*. The dashed lines phase diagram corresponds to smaller values of the heating than the solid lines phase diagram. The dotted line indicates a typical boundary temperature. Notice that the temperature and flux scales have been arbitrarily chosen and are for reference only.

In the description given above, a hot solution (or hot loops) with the same temperature gradient at the footpoint has a hotter summit when a heating variation is applied. Also, a hot-cool solution is obtained when a heating variation is incorporated. The contour $FGHI$ is a hot-cool loop with summit temperature at I. This case gives a hotter summit than hot-cool loops without heating variation i.e., $FGH'I'$.

On the other hand, when heating is considered to be proportional to $\sim \exp(-s/s_*)$, the same description can be carried out by assuming as a series of instantaneous variations. Therefore, it is found, that an open contour on the phase diagram can be changed into a closed one if the heating decreases along the field line, since the cool temperature T_c is now reduced. This behaviour can be easily seen in Figure 3.2 for the dashed line which starts at the point E and finishes at I. In addition, the maximum temperature, no longer at the summit, may increase as T_h increases.

3.3 Numerical Results

In the previous section, the properties of the possible solutions of equation (3.13) were given in terms of phase plane diagrams with the conductive flux being shown as a function of temperature. In this section the numerical solution is sought in order to find the parameter regimes for which they exist. The solution of equations (3.13) and (3.14) is governed by the value of the three dimensionless parameters L_*, h_* and s_*.

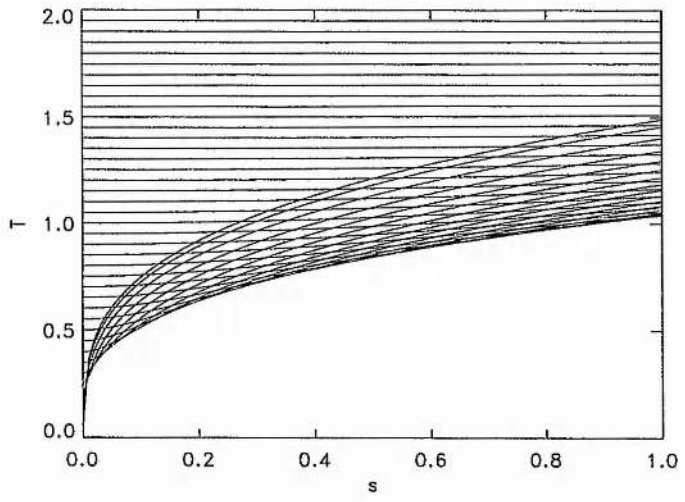

Figure 3.5: Temperature profiles $T(s)$ considering different boundary temperature for $L_* = 0.48$, $h_* = 101$ and $s_* = 0.01$.

Figure 3.5 is a plot of temperature as a function of the position. It shows families of solutions to the equation (3.13) with the boundary conditions (3.14) for the particular values of the parameter L_*, h_* and s_* indicated. When the boundary

temperature T_b (at $s = 1$) decreases the summit temperature T_s decreases, until T_b reaches a minimum value. From this value when the boundary temperature increases, the summit temperature decreases. i.e., two families of solutions exist, which have the same boundary temperature but different summit temperatures.

The presence of the parameter s_* in the heating term of the equation (3.13) makes it difficult to study the main characteristic of the solution of this energy equation. However, one can plot the summit temperature (T_s) as a function of the boundary temperature (T_b) in order to visualise the main features of the solutions of the equations (3.13) and (3.14) when the values of the parameters L_*, h_* and s_* are changed.

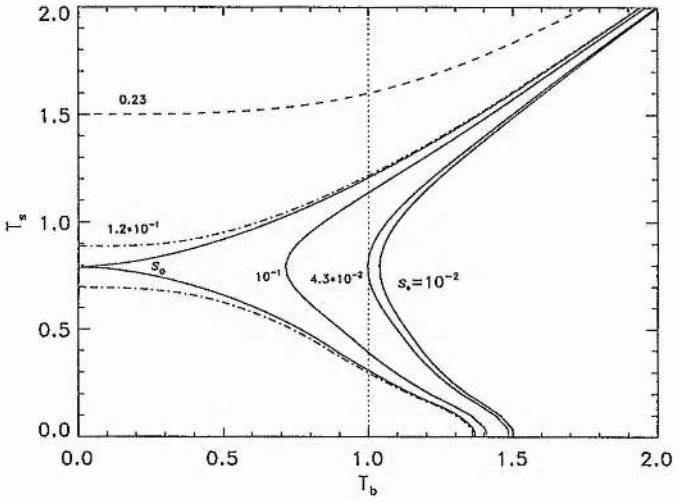

Figure 3.6: The summit temperature T_s as a function of the boundary temperature T_b for different values of the decay length of the heating s_*. The dotted line indicates the particular boundary condition $T_b = 1$.

Figure 3.6 shows the summit temperature T_s as a function of the boundary temperature T_b for $L_* = 4.8 \times 10^{-1}$, and $h_* = 101$. The different curves are labelled with the corresponding value of s_*. Every point in the curve of this figure corresponds to a static solution, whereas every curve is a family of solutions (in contrast to the Figure 3.5, where every curve is a static solution of the energy equation). The dashed and dashed-dot lines correspond to the family of solutions for which $s_* > s_0$, s_0 being the value of the scale-length for the heating decay for which there is a gap in the values of T_s. That is there are no solutions with these values of T_s. For any value of

$s_* < s_0$ (s_0 being the value of decay scale length of the heating for which $T_b = 0$ at the turning point) there is a minimum value $T_b = T_{bt}$ [turning point at $T_s = T_{st}$] below which solutions of equations (3.13) and (3.14) do not exist (Ibañez et al, 1992). Two different solutions exist between $T_{bt}(s_*) < T_b < T_{b0}(s_*)$ (T_{b0} being the value of T_b at which the summit temperature approaches to zero) and one solution when $T_b > T_{b0}(s_*)$. In the upper branch ($T_s > T_{st}$) the summit temperature T_s increases when the boundary temperature T_b increases. On the lower branch, the summit temperature T_s decreases when the boundary temperature T_b increases. Therefore, it is seen in Figure 3.6 that the effect of increasing the parameter s_* is to shift the turning point to lower values of T_b.

When one considers the case where a particular boundary condition is taken, for example $T_b = 1$, solutions at equilibrium exist only when $s_* \geq s_{*c}$ ($= 4.3 \times 10^{-2}$). From this value upwards there are many-valued solutions where summit temperature increases in the upper branch while it decreases in the lower branch. If the value of s_* is increased, there is a value at which a hot solution exists. Very high values of s_* would correspond to a uniform heating, as expected.

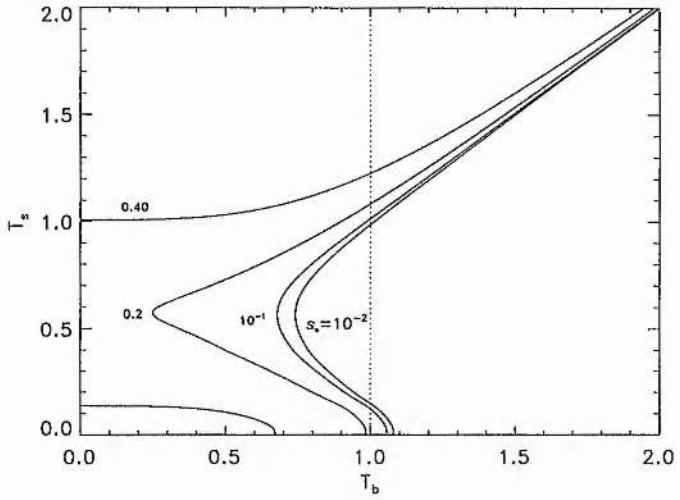

Figure 3.7: The summit temperature T_s as a function of the boundary temperature T_b for different values of the decay-length of the heating s_*. The dotted line indicates the particular boundary condition $T_b = 1$. Parameters used are $L_* = 2 \times 10^{-1}$ and $h_* = 1.01 \times 10^2$

In the Figures 3.7 and 3.8 the summit temperature as a function of the boundary

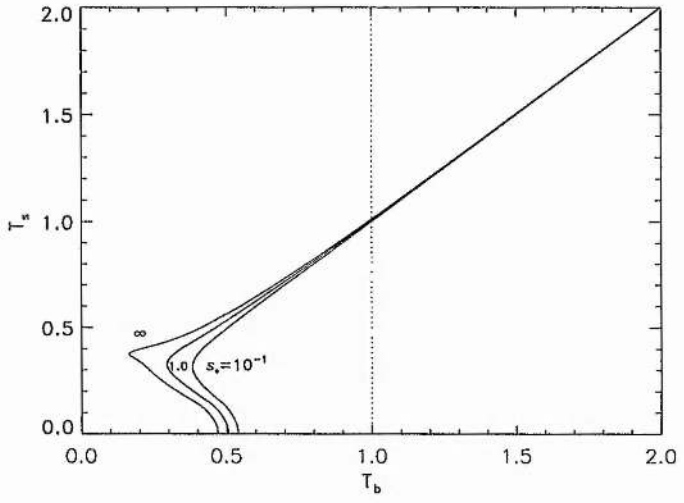

Figure 3.8: The summit temperature T_s as a function of the boundary temperature T_b for different values of the decay-length of the heating s_*. The dotted line indicates the particular boundary condition $T_b = 1$. Parameters used are $L_* = 2 \times 10^{-2}$ and $h_* = 1.01 \times 10^2$

temperature has been plotted for $L_* = 2.0 \times 10^{-1}$ and 2.0×10^{-2} respectively. The main feature observed in Figure 3.6 remains, when s_* is varied. The turning points shift to the left when s_* is increased. But these turning points are shifted to lower values of T_s when L_* decreases.

Figure 3.7 shows that for a given boundary temperature, for instance $T_b = 1$, solutions are found for any value of s_*. Hence, no critical decay-length of the heating exists. However, by reducing the value of T_b allows the existence of this critical value where thermal non-equilibrium appears (Roberts and Frankenthal, 1980; Priest, 1982).

In Figure 3.8 one sees that considering a given boundary temperature $T_b = 1$ only one solution exists for any value of s_*. In addition, a gap is no longer present when s_* is large.

For a given loop structure of small length in contact with a hot boundary the thermal conduction is very effective and will remove any temperature gradient. Therefore, low boundary temperature has to be taken in order to find a critical value of s_*. But, if this value is taken too low, for example, $T_b = 10^{-2}$ (see Figure 3.8) no hot solution is found.

A general plot can be drawn by considering the effect of changing the length of the loop and keeping fixed the heating decay-length and the base value of the heating. Figure 3.9 shows families of solutions for $s_* = 5 \times 10^{-2}$ and $h_* = 101$, for different values of the length of the loop. The effect of decreasing L_* is to shift the turning points to lower values of T_s and T_b. Therefore, one sees that low temperatures at the base can be obtained when length of the structure is reduced when s_* and h_* remain unchanged. Additionally by considering a particular boundary condition $T_b = 1$ one can see that no equilibrium solution exists when L_* is greater than a critical value.

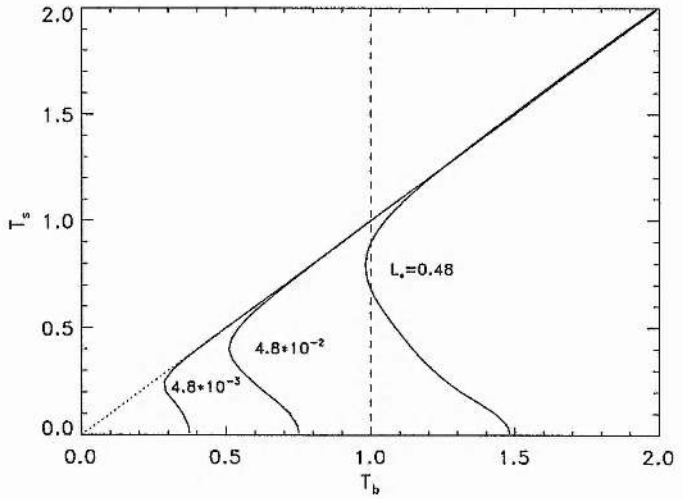

Figure 3.9: The summit temperature T_s as a function of the boundary temperature T_b for different values of the loop length L_*. The dashed and dotted lines indicate the particular boundary conditions $T_b = 1$ and $T_b = T_s$, respectively.

Another important feature of the solution of the equations (3.13) and (3.14) is the variation of the parameter h_* when s_* and L_* are kept constant. Figure 3.10 shows this effect; one may conclude that the effect of changing the value of the parameter h_* is similar to that of changing the parameter s_*, as can be seen in the Figure 3.6, where an increase of h_* shifts the turning point to lower values of T_b, and the two branches are separated by a gap when $h_* = h_{*0}$, h_{*0} being the value of the heating at the base where $T_b = 0$.

It has been seen that multiple solutions can be obtained by solving (3.13) and (3.14). Cool summits can be found, for example in the Figure 3.7 if a parallel line to

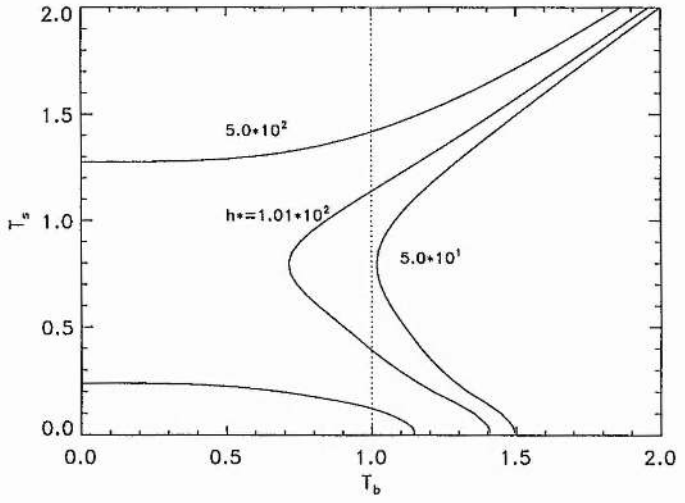

Figure 3.10: The summit temperature T_s as a function of the boundary temperature T_b for different values of the heating deposition h_*. The dotted line indicates the particular boundary condition $T_b = 1$. Parameters used are $L_* = 0.48$ and $s_* = 0.1$.

the T_b-axis is drawn. So, low summit temperatures exist for different values of the decay length s_* but having different boundary temperatures.

In the above $T_s(T_b)$ graphs (Figures 3.6 - 3.10) there exists a slight bend in the lower branch of the curves, suggesting a lower branch at very low summit temperature. Indeed, it has been found after improving the numerical calculations that this lower branch must exist but it becomes very difficult to resolve numerically.

In section 3.4 it will be shown that considering a simplified cooling function allows the lower branch to appear. This result confirms that the numerical code cannot resolve the lower branch when the full cooling function is used, but implies that this solution can be found by using another technique, as is shown in the next section, where starting from the known values of low summit temperature one can get the parameters L_*, s_* and h_* that satisfy the equations (3.13) and (3.14).

3.3.1 Hot-cool Solution

In contrast to Steele and Priest (1990a), the heating function used in this work depends explicitly on the position along the loop s. The energy equation cannot be treated as they did because is a non-autonomous system. But, one can use the

fact that the temperature and density of the prominence are known and start the integration of the temperature profile from the summit. Then, in order to explore the hot-cool solution, namely prominence-like solutions, equation (3.13) is integrated from $s = 0$, $T = 0.2$ (in units of $10^5 K$), $dT/ds = 0$, and the integration is continued until $T = 0.2$ (the footpoint temperature is taken at chromospheric values), say at $s = s_1$, then one may set $s' = s/s_1$, to make (3.13) becomes

$$\frac{d}{ds'}\left(T^{5/2}\frac{dT}{ds'}\right) = L'^2\left[\chi T^{\alpha-2} - h' \exp\left(-\frac{1-s'}{s'_*}\right)\right] \tag{3.18}$$

with $L' = L_* s_1$, $h' = h_* \exp[(1-1/s_1)/s_*]$ and $s'_* = s_*/s_1$ and all boundary conditions imposed on equation (3.14) are satisfied.

Figure 3.11 shows the temperature as a function of s when T_b is chosen at the chromospheric value $T_b = 0.2$ for the values of the parameters given in Table 3.1. All these curves show a cool summit at temperatures of $T_s = 0.2$ but they are hot along at least part of their length. The maximum temperatures are located between the summit and the footpoint. Using this technique one finds the values of the parameters L', s'_* and h' that produce prominence-like solutions.

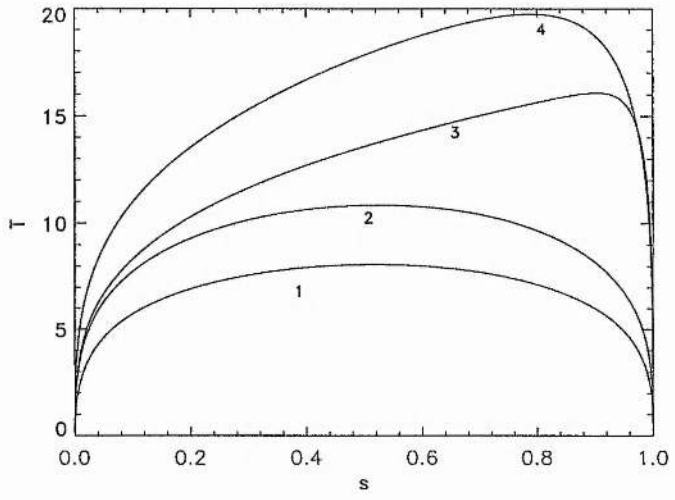

Figure 3.11: The variation of temperature along a loop from the summit at $s = 0$ to the footpoint at $s = 1$. The numbers refer to the listed values given in Table 3.1.

In Figure 3.11 one sees that when the length of the loop L' is increased the maximum temperature increases and is shifted to the footpoint (it must be remembered

that the summit temperature is located at $s = 0$). The latter effect is mainly due to the parameter s'_*. When s'_* is small more heat is provided to the footpoint than the summit.

	L'	s'_*	h'	T_{max}
	49.78	6.27×10^{-2}	1.53×10^{1}	5.48
	105.67	2.95×10^{-1}	4.31×10^{-1}	5.81
	211.23	1.48×10^{1}	3.84×10^{-2}	6.11
	264.49	1.46×10^{1}	3.07×10^{-3}	6.57
	292.35	1.52×10^{1}	2.77×10^{-2}	6.78
	344.32	9.06×10^{-1}	4.39×10^{-2}	7.58
1	484.06	2.85×10^{0}	2.01×10^{-2}	8.08
2	1236.53	1.89×10^{0}	9.09×10^{-3}	10.82
	1240.75	3.11×10^{-1}	3.89×10^{-2}	12.30
3	1422.72	2.71×10^{-2}	3.68×10^{0}	16.08
	2216.11	8.45×10^{-2}	2.49×10^{-1}	17.24
4	3527.49	8.84×10^{-2}	1.46×10^{-1}	19.74
	5092.81	9.19×10^{-2}	9.57×10^{-2}	21.97
	5216.49	4.49×10^{-2}	3.39×10^{-1}	23.09

Table 3.1: Parameters Obtained For Prominences solution using Equation (3.18)

3.4 Simplified Cooling Function

This section will discuss the thermal equilibrium of the system (3.13)-(3.14) by considering a simplification of the cooling function. The cooling function will be assumed to be a two range piecewise function:

$$Q(T) = \chi T^{\alpha-2} = \begin{cases} T_a^{-7}\, T^{7/2}, & T < T_a, \\ T^{-7/2}, & T > T_a, \end{cases} \tag{3.19}$$

where T_a is the temperature at which the powers in the radiative loss function change value; for a maximum in the loss function at about 10^5 $T_a = 10^5/T_0$. This function

satisfies the basic requirement of the general cooling function as shown in Chapter 2, namely that the radiation has a peak at 10^5K. Thus, one expects the qualitative features of the solution to (3.13) and (3.14) to carry over when the function (3.19) is replaced by a more accurate form.

Figure 3.12 is a plot of summit temperature as a function of the boundary temperature resulting from the numerical integration of equation (3.13) and (3.14) for a constant value of the heating term or equivalently a large value of s_*. The different curves are labelled with the corresponding value of L_*^2. As is seen in this figure two points in which all the curves intersect are found at $T_b = 0.07$ and $T_b = 0.138$. These points correspond to two thermal equilibrium states given by the solutions of $\mathcal{L} = 0$.

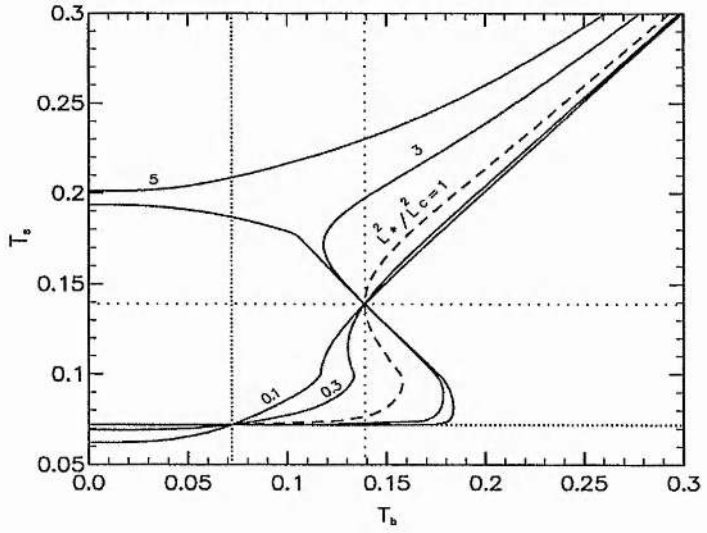

Figure 3.12: The summit temperature T_s as a function of the boundary temperature T_b for different values of the loop length L_*^2. The close spaced dot and wide spaced dot lines indicate the two thermal equilibria as a result of $\mathcal{L} = 0$.

For L_*^2 small ($< 0.1L_c^2$) the relation $T_s(T_b)$ is a single-valued function while for $L_*^2 > L_c''^2$ ($\approx 0.1L_c^2$) it becomes a three valued function with an S-type characteristic. In particular, at $T_b = T_e$, T_e being the temperature at equilibrium (in this case $T_e = 0.138$) and for $L_*^2 > L_c'^2$ ($\approx 0.39L_c^2$), the multiple solutions are the thermal equilibrium state and two additional states in nonthermal equilibrium. For large values of L_*^2 ($L_*^2 > L_{*0}^2$, L_{*0}^2 being the value for which $T_b = 0$ at the turning point) a gap for the summit temperature T_s appears where no solution exists.

For values of $L_*^2 < L_c''^2$ the summit temperature is a monotonically increasing function of T_b. For any value of L_*^2 in the range $L_c''^2 < L_*^2 < L_{*0}^2$, however, there are two turning points (or catastrophe points) that divide the curve $T_s(T_b, L_*^2)$ in the branches corresponding to three different solution of equations (3.13) and (3.14). In the upper and lower branches, the summit temperature T_s increases when the boundary temperature T_b increases, and in the middle branch the summit temperature decreases when the boundary temperature increases.

When $L_*^2 > L_{*o}^2$ only the lower turning point remains, and it separates the middle and lower branches and, as was pointed out above, a gap for T_s exists. The width of such a gap increases when L_*^2 increases. When the value of L_*^2 is considered to be equal to L_c^2 (the dashed curve in Figure 3.12) one can see that the upper turning point coincides with the temperature at thermal equilibrium. This value of L_*^2 is the critical one found in the Section 3.5.1 below making use of a simple first order stability analysis.

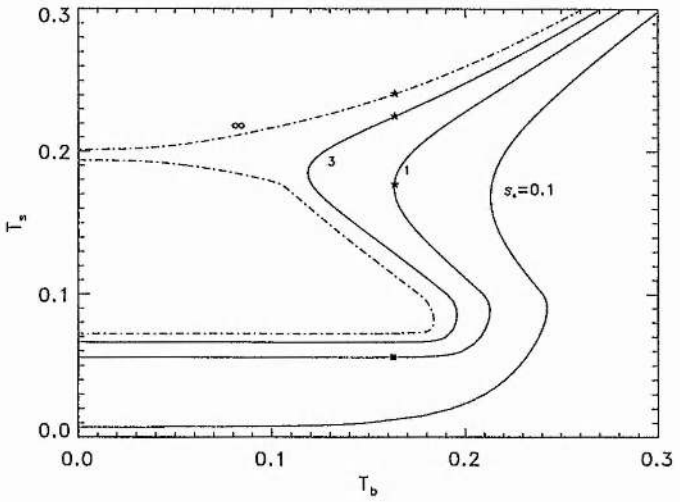

Figure 3.13: The summit temperature T_s as a function of the boundary temperature T_b for different values of the decay-length of the heating s_*. The dotted-dash line corresponds to a uniform heating. The filled star and square indicate the summit temperature at a fixed value of T_b.

Figure 3.13 shows several families of the static solution for $L_*^2 = 5L_c^2$ and the labelled values of s_*. The dotted-dash line is the family of static solutions when the heating is considered constant or s_* is very large. It represents the general trends that

have been shown previously, including the gap. If s_* is decreased the gap disappears and the turning point is shifted to the right hand side. When s_* is decreased one can observe that the lower branch in those curves are shifted to lower values of T_s as expected. The filled star and square in Figure 3.13 correspond to the solution of the equation (3.13) with (3.14) for a particular value T_b. It can be seen how the temperature at the summit decreases with decreasing s_*. Here one can assume that the thermal structure at coronal temperatures evolves through a sequence of equilibria that satisfy the energy equation (3.13). If s_* is very small (as has been described previously), no static solution exists for that particular T_b and the thermal structure will evolve to an equilibrium with a lower temperature at the summit (at a value of T_s showed with a filled square).

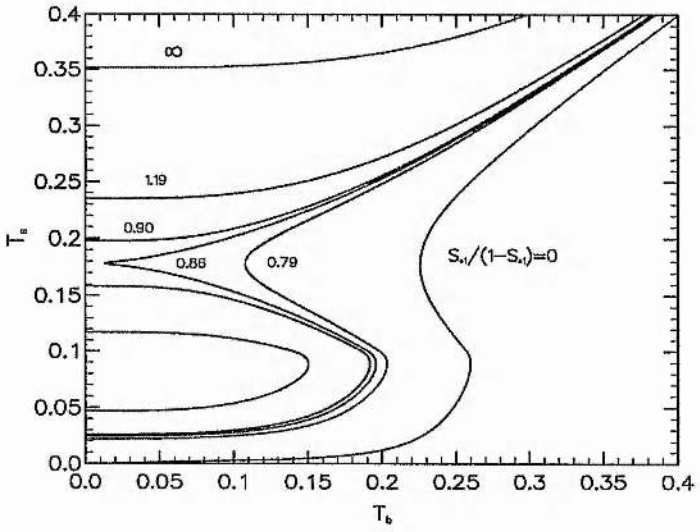

Figure 3.14: The summit temperature T_s as a function of the boundary temperature T_b for different values of the ratio $s_{*1}/(1-s_{*1})$.

Figure 3.14 shows the summit temperature as a function of boundary temperature for different values of the ratio of $s_{*1}/(1-s_{*1})$ when a step function form of the heating is considered (Figure 3.15). In section 3.2 a phase plane diagram for two different values of h_* was described and analysed qualitatively to find what happened to the solution when an instant variation of the heating was applied. When s_{*1} is increased from 0 to 1 one can observe the same general effect studied previously with the exponential variation of the heating.

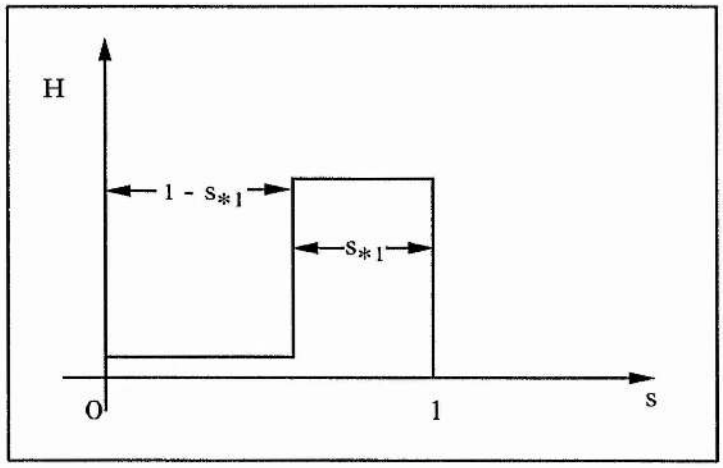

Figure 3.15: Schematic functional form for the spatial dependence of the heating function.

3.5 The Stability of the Static Solutions

In previous sections, static solutions of the energy equation were obtained. Multiple solutions for given values of the parameters and boundary conditions were found. Now, an interesting problem would be to study the stability of the static solutions of the energy equation. In order to determine the stability of a given equilibrium (or static solution), the method proposed by Landau (1944) for studying turbulence will be used (see also Drazin and Reid 1981; Ibañez, Parravano and Mendoza 1993; Ibañez and Rosenzweig 1995).

The aim of this method is to examine the conditions prevailing just at the onset of the nonlinear regime and to analyse the scope of the well-known linear criteria for thermal instability, instead of following the evolution of a particular thermal structure during a well advanced stage of the nonlinear regime.

One assumes that the dimensionless time-dependent energy equation at constant pressure ($p = 1$),

$$\frac{\partial T}{\partial t} = T \left\{ \frac{\partial}{\partial s} \left(T^{5/2} \frac{\partial T}{\partial s} \right) - L_*^2 (\chi T^{\alpha-2} - H) \right\} \tag{3.20}$$

has solutions of the form

$$T(s,t) = \overline{T}(s) - \delta T(s,t), \tag{3.21}$$

$$\delta T(s,t) = \sum_{i=1}^{\infty} A^i(t) f_i(s), \tag{3.22}$$

$$\frac{d \mid A(t) \mid}{dt} = \sum_{i=1}^{\infty} a_i \mid A(t) \mid^i, \tag{3.23}$$

where $\overline{T}(s)$ is the solution to the static equation

$$\frac{\partial}{\partial s}\left(T^{5/2}\frac{\partial T}{\partial s}\right) - L_*^2(\chi T^{\alpha-2} - H) = 0 \tag{3.24}$$

with boundary conditions

$$\begin{aligned} \frac{\partial T}{\partial s} &= 0 \qquad \text{at} \qquad s = 0 \quad \text{(summit)}, \\ T &= T_b \qquad \text{at} \qquad s = 1 \quad \text{(boundary)}, \end{aligned} \tag{3.25}$$

$A(t)$ is a function of time, and $f_i(s)$ are functions of the coordinate s that satisfy the boundary conditions

$$\begin{aligned} \frac{df_i}{ds} &= 0 \qquad \text{at} \qquad s = 0, \\ f_i(s) &= 0 \qquad \text{at} \qquad s = 1. \end{aligned} \tag{3.26}$$

Both $A(t)$ and $f_i(s)$ are to be determined. Strictly speaking, the series (3.22) and (3.23) contain an infinite number of terms. In practice, however, the first few terms are enough to examine the stability near the critical states.

3.5.1 First-Order Approximation

If $\overline{T} = T_e$ is a trivial solution, the linear analysis of stability can be carried out analytically. In fact, substituting (3.21) and (3.22) in equation (3.20) and setting

terms of first order in A equal, one obtains the equation

$$\frac{d^2 f_1}{ds^2} + \frac{1}{T_e^{7/2}} \left(-(\alpha - 2) L_*^2 \chi T_e^{\alpha - 2} - a_1 \right) f_1 = 0 \tag{3.27}$$

with boundary conditions

$$\begin{aligned} \frac{df_1}{ds} &= 0 \qquad \text{at} \qquad s = 0, \\ f_1(s) &= 0 \qquad \text{at} \qquad s = 1, \end{aligned} \tag{3.28}$$

(see Appendix C for the derivation of equation (3.27)).

The solutions of equation (3.27) - (3.28) are

$$f_1(s) = \cos[(2N - 1)\frac{\pi}{2} s] \tag{3.29}$$

where $N = 1, 2, ...$

On the other hand, $A(t)$ in equation (3.23) up to first order becomes

$$A(t) = A_0 e^{a_1 t} \tag{3.30}$$

where the rate a_1 is given by

$$a_1 = -(\alpha - 2) L_*^2 \chi T_e^{\alpha - 2} - b_N^2 T_e^{7/2} \tag{3.31}$$

A_o is a constant, T_e is any solution of the equation $\mathcal{L} = 0$, and b_N is $(2N - 1)\pi/2$, respectively.

From equations (3.30) and (3.31) one concludes that the thermal structure is thermally stable ($a_1 < 0$) if

$$-(\alpha - 2) L_*^2 \chi T_e^{\alpha - 3} - b_N^2 T_e^{5/2} < 0. \tag{3.32}$$

For the two range cooling function and Hildner cooling function, the thermal equilibrium is absolutely stable if $(2 - \alpha)$ is negative as far as the linear approximation is concerned. But for $(2 - \alpha) > 0$ the trivial solution becomes unstable provided that

$$L_*^2 > \frac{b_N^2}{-(\alpha-2)\chi T_e^{\alpha-11/2}}. \tag{3.33}$$

On the other hand, when the instability sets in the fastest mode is the fundamental one ($N = 1$), for which the equation (3.31) defines a critical value of L_*^2 for the marginal state ($a_1 = 0$) i.e.

$$L_*^2 = L_c^2 \equiv \frac{b_1^2}{(2-\alpha)\chi T_e^{\alpha-11/2}} \tag{3.34}$$

Note that L_c defined by equation (3.34) has physical meaning only if $2 - \alpha > 0$. For the simplified cooling function $(2 - \alpha) > 0$ corresponds to $T > T_a$, therefore the critical value for the marginal state is $L_c^2 = \pi^2 T_e^7/14$.

Therefore, if $L_*^2 > L_c^2$, a_1 is positive and the solution is unstable.

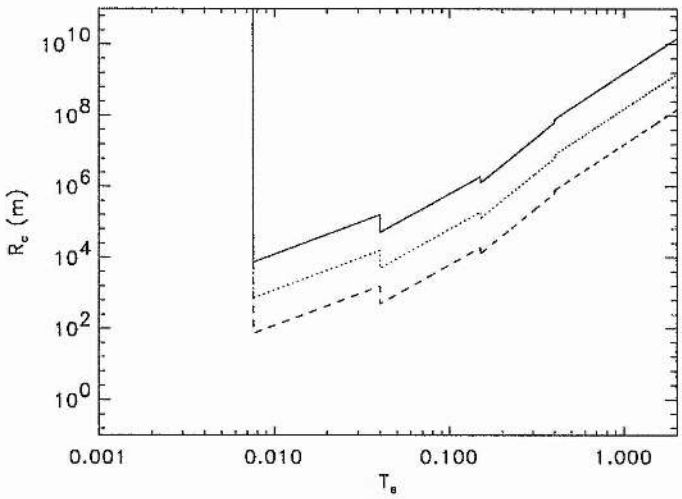

Figure 3.16: Critical dimension of the structure as a function of temperature separating regions of thermal stability and instability. The oblique solid, dotted and dashed line, correspond to a plasma at pressure $p_0 = 0.01,\ 0.1$ and 1.0 pascals respectively.

From the equation

$$L_*^2 = \frac{L_0^2 \tilde{\mu}^2 p_0^2 \chi_0 T_0^{\alpha-11/2}}{\mathcal{R}^2 \kappa_0} \tag{3.35}$$

and equation (3.34) one can determine the division of marginally stable homogeneous structures in thermal equilibrium as :

$$R_c = L_0 = \frac{\mathcal{R}b_1}{\tilde{\mu}p_0}\left[\frac{\kappa_0}{(2-\alpha)\chi_0\chi T_e^{\alpha-11/2}T_0^{\alpha_0-11/2}}\right]^{1/2}. \tag{3.36}$$

Structures with a dimension greater than R_c will be thermally unstable.

Figure 3.16 shows R_c as a function of temperature according to equation (3.36), for pressures $p_0 = 0.01,\ 0.1,\ 1.0$ pascals. For a temperature between $\sim 1.5 \times 10^4$ and 10^6 K, perturbations on the scale-size below the diagonal broken line are stable. The broken shape of this line is due to the piecewise nature of the radiation cooling function given by Hildner (1974). In the range of $T < 1.5 \times 10^4$ K perturbations are also stable given that $(2-\alpha) < 0$.

3.5.2 Second-Order Approximation

For the trivial solution T_e, substituting (3.21) and (3.22), and setting terms of second order in A equal, one obtains the equation

$$\frac{d^2f_2}{d\tilde{s}^2} + \omega^2 f_2 = -\frac{5}{2T_e} + \frac{a_2}{b_N^2 T_e^{7/2}}\cos\tilde{s} + \left\{\frac{6}{T_e} + \frac{L_*^2(\alpha-2)\chi T_e^{\alpha-3}}{b_N^2 T_e^{7/2}}\left[1+\frac{1}{2}(\alpha-3)\right]\right\}\cos^2\tilde{s} \tag{3.37}$$

with the boundary conditions

$$\begin{aligned} \frac{df_2}{d\tilde{s}} &= 0 \qquad \text{at} \qquad \tilde{s} = 0, \\ f_2(\tilde{s}) &= 0 \qquad \text{at} \qquad \tilde{s} = \frac{\pi}{2}, \end{aligned} \tag{3.38}$$

where $\tilde{s} = (\pi/2)s$ $\omega^2 = 2 + L_*^2(\alpha-2)\chi T_e^{\alpha-11/2}/b_N^2$ and $b_N = (2N-1)\pi/2$. As is well known, the fundamental mode $N = 1$ is the fastest growing mode.

The general solution of equation (3.37) with boundary (3.38) is

$$f_2(\tilde{s}) = -\frac{5}{2T_e\omega^2}(1-\cos\omega\tilde{s}) + \frac{a_2}{b_1^2 T_e^{7/2}(\omega^2-1)}(\cos\tilde{s}-\cos\omega\tilde{s})$$

$$+\frac{1}{\omega^2(\omega^2-4)}\left[\left(\frac{6}{T_e}\right)+\frac{L_*^2(\alpha-2)\chi T_e^{\alpha-3}[1+\frac{1}{2}(\alpha-3)]}{b_1^2 T^{7/2}}\right]$$

$$\times\left[(2-\omega^2)\cos\omega\tilde{s}+\omega^2\cos^2\tilde{s}-2\right]+\overline{c_1}\cos\omega\tilde{s}, \tag{3.39}$$

where $\overline{c_1}$ is an arbitrary constant and

$$a_2 = T_e^{7/2}b_1^2\frac{(\omega^2-1)}{\cos(\frac{\pi}{2}\omega)}\left\{\frac{5}{2T_e\omega^2}[1-\cos(\frac{\pi}{2}\omega)]+\frac{1}{\omega^2(\omega^2-4)}\right.$$

$$\left[\left(\frac{6}{T_e}\right)+\frac{L_*^2(\alpha-2)\chi T_e^{\alpha-3}[1+\frac{1}{2}(\alpha-3)]}{b_N^2 T^{7/2}}\right]$$

$$\left.\times\left[(2-\omega^2)\cos\frac{\pi}{2}\omega-2\right]+\overline{c_1}\cos(\frac{\pi}{2}\omega)\right\} \tag{3.40}$$

is the Landau constant.

Close to the marginal state, defined by equation (3.34), the equations (3.39) and (3.40) simplify to

$$f_2(\tilde{s}) = -\frac{5}{2T_e}(1-\cos\tilde{s}) - \frac{a_2}{2L_*^2(\alpha-2)\chi T_e^{\alpha-2}}\tilde{s}\sin\tilde{s}$$

$$-\frac{1}{3}\left(\frac{5}{T_e}-\frac{(\alpha-3)}{2T_e}\right)(\cos\tilde{s}-\cos^2\tilde{s}-2)+\overline{c_1}\cos\tilde{s} \tag{3.41}$$

$$a_2 = -\frac{2}{3b_N}L_*^2(\alpha-2)\chi T_e^{\alpha-2}\left(-\frac{5}{2T_e}+\frac{(\alpha-3)}{T_e}\right) \tag{3.42}$$

respectively.

On the other hand, from the integration of equation (3.23) up to the second-order, one obtains

$$A(t) = A_0\left[-\left(\frac{a_2}{a_1}A_0\right)+\left(1+\frac{a_2}{a_1}A_0\right)e^{-a_1 t}\right]^{-1} \tag{3.43}$$

A_0 being the value of $A(t)$ at $t = 0$.

As is well-known, for $L_*^2 > L_c^2$ ($a_1 > 0$), supercritical stability (Landau, 1944; Drazin and Reid, 1981) sets in when $a_2 < 0$. Then, the trivial solution becomes linearly unstable, but it tends to a new static solution eventually because the amplitude $A(t)$ equilibrates to $A_e = \mid a_1 \mid / \mid a_2 \mid$ when $t \to \infty$. Therefore, as follows from equation (3.43), the perturbation saturates to the value A_e as $t \to \infty$, i.e., the uniform thermal structure smoothly evolves to a nonuniform static state. On the other hand, subcritical instability occurs when $a_2 > 0$ and $a_1 < 0$ ($L_*^2 < L_c^2$). In this case, $A(t) \to 0$ as $t \to \infty$ if $A_0 < A_e$ (threshold value). But, if $A_0 > A_e$ the solution (3.42) breaks down at the time

$$t_2 = \frac{1}{\mid a_1 \mid} \ln \frac{A_0 / \mid A_e \mid}{\mid 1 - (A_0 / \mid A_e \mid) \mid} \tag{3.44}$$

Obviously, first-order disturbances $f_1(s) = -\cos \pi s/2$ also are solutions to the equations (3.27), and the corresponding second-order analysis leaves a change of sign for a_2, i.e. if the loop under consideration is supercritically stable for disturbances increasing the summit temperature, it becomes superexponentially unstable for disturbances decreasing the summit temperature, as far as the second approximation holds.

a_1	a_2	Definition
$-$	$-$	Asymptotical Stability
$-$	$+$	Subcritical Instability
$+$	$-$	Supercritical Stability
$+$	$+$	Superexponential Instability

Table 3.2: Definition for the combination between sign of a_1 and a_2.

Additionally, one may conclude that when loops in thermal equilibrium are subcritically unstable ($a_1 < 0, a_2 > 0$) for positive first-order disturbances (or increasing the summit temperature), it will be asymptotically stable for negative disturbances (or decreasing the summit temperature) (see Table 3.2).

In Figure 3.12, for the upper thermal equilibrium solution $T = T_e$ one finds that close to L_c^2 for $L_*^2 < L_c^2$ ($a_1 < 0$), for positive disturbances, $a_2 < 0$, but for negative disturbances, $a_2 > 0$. Therefore, the above solution is asymptotically stable for positive disturbances, and subcritically unstable for negative disturbances, with a threshold value for the amplitude given by $\mid a_1 \mid / \mid a_2 \mid$, i.e. the loop is stable with respect to an increase in its temperature, but it cools down catastrophically when it suffers large enough negative disturbances. For $L_*^2 > L_c^2$ ($a_1 > 0$), $a_2 < 0$ for positive disturbances. Therefore, the solution T_e is supercritically stable and will evolve towards its saturated states, i.e. to stable solutions. For negative disturbances $a_2 > 0$, the structure becomes superexponentially unstable, i.e. when one increases the temperature of the loop the structure goes to an inhomogeneous solution, but when the temperature is reduced the loop cools down catastrophically. The above result shows the evolutionary tendency in the neighbourhood of the thermal equilibrium solution T_e. It is obvious that a higher order of approximation would be required to follow the above evolution.

The above considerations on the stability of the trivial solution suggest that the positive slope branches (upper and lower branches) on the plane (T_s, T_b) are stable solutions and the middle negative slope branch as the locus of the unstable static solutions of (3.24) and (3.25). Therefore, supercritical stability and subcritical instability appear when the relation $T_s(T_b)$ shows turning points. Otherwise, the structure is absolutely stable as is apparent from Figure 3.12 for $L_*^2 < 0.3L_c^2$.

T (K)	a_1	a_2
$< 1.5 \times 10^4$	$-$	$+$
$1.5 \times 10^4 - 8.0 \times 10^4$	$+$	$-$
$8.0 \times 10^4 - 3.0 \times 10^5$	$+$	$-$
$3.0 \times 10^5 - 8.0 \times 10^5$	$+$	$-$
$8.0 \times 10^5 - 10^7$	$+$	$-$

Table 3.3: Nature of the thermal stability for the different range in the Hildner's cooling function.

Table 3.3 summarises the behaviour of the thermal stability for the different range

in the piecewise cooling function given by Hildner (1974).

It is interesting to remark that while the linear analysis of thermal equilibrium may predict thermal stability, eventually, the nonlinear analysis with the second order approximation allows one to deduce how the structure evolves once it becomes linearly unstable.

3.6 Constant Total Heating

The previous section considered the heating function decaying with the distance from the chromosphere along the loop to the summit with the functional form

$$H(s) = h_0 \exp\left(-\frac{1-s}{s_*}\right). \tag{3.45}$$

h_0 had been taken as the heat deposition at the base of the loop and s_* is the free parameter which determines the spatial scale of the heating decay.

The total energy input is not kept constant in the loop when different values of s_* were taken.

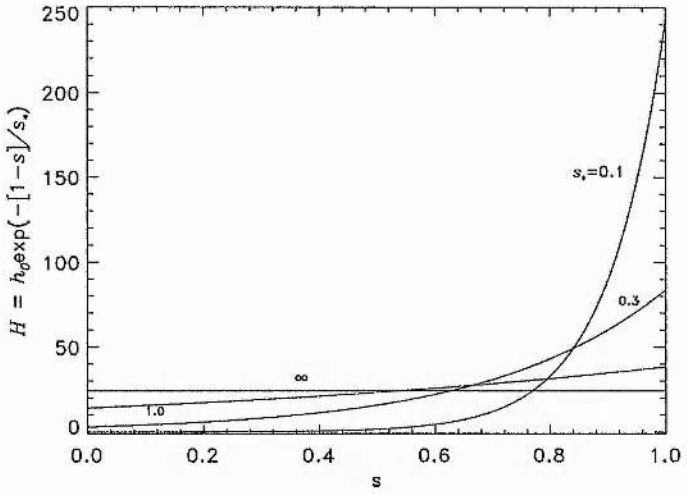

Figure 3.17: Form of the heating function keeping the total heating constant.

In the present section an assumption upon this condition is considered and the value of h_0 is chosen such that the total energy input into the loop remains constant.

The value of h_0 is determined by requiring

$$\int_0^1 H(s)ds = \widetilde{H}, \tag{3.46}$$

where $\widetilde{H}$ is the total dimensionless energy input. Therefore

$$h_0 = \frac{\widetilde{H}}{s_*[1 - \exp(-\frac{1}{s_*})]}. \tag{3.47}$$

Figure 3.17 shows the variation of heating along the loop for different values of s_* keeping the total heat input constant. As can be seen from Figure 3.17, the base value of the heating h_0 increases as s_* decreases in order to keep the total heating $\widetilde{H}$ constant.

Figure 3.18 shows the results of this new consideration. The case for $s_* = 0.1$ studied previously in Figure 3.13 is indicated with dotted line for comparison.

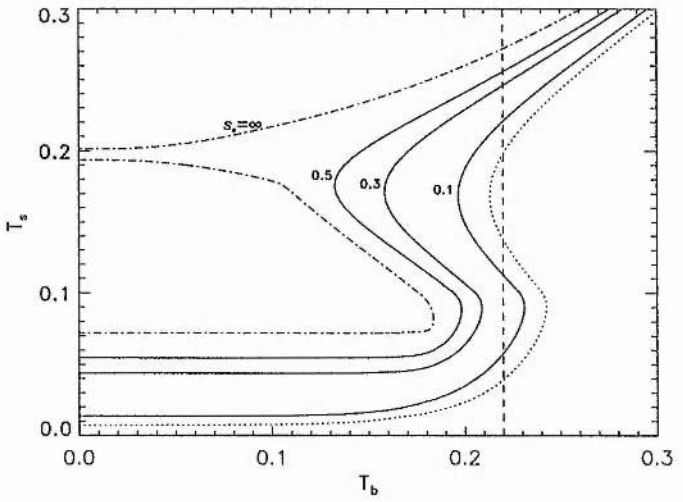

Figure 3.18: The summit temperature T_s as a function of the boundary temperature T_b for different values of the decay length of the heating s_*. The dashed line indicates a particular boundary condition. The curve with dotted line corresponds to $s_* = 0.1$, when the total heating is non-constant.

When s_* is increased the turning point shifted to the left, as was obtained in section 3.3. However, by comparing the two curves for the same values of $s_* = 0.1$ it is seen that for total heating input constant the turning point shifts to lower values of T_b. But if a fixed boundary condition is taken, namely $T_b = 0.22$ a hot summit (dotted line) becomes hotter (solid line). A summit temperature in the lower

branch also presents an increase in temperature when constant total heating input is considered. However, the summit temperature in the middle branch shows a decrease in temperature.

The increase in temperature in the upper and lower branch is expected when the total energy in the loop is larger and one may identify them as stable solutions. However, the decreasing in the middle branch temperature suggest that those solutions are unstable.

3.7 Summary of the Chapter

In this chapter the static solutions of thermal equilibrium at constant pressure along a symmetric coronal loop have been investigated. Here, the coronal heating function, which depends only on the spatial variable, has been considered. These solutions have been initially identified by using a phase diagram technique. The phase diagram, under consideration of spatially dependent heating function, represents a non-autonomous system. It was seen that a prominence-like condensation can be produced when a reduction of the heating along the field lines is applied.

Furthermore, the static solutions were studied numerically and the effect of the parameters L_*, h_* and s_* were analysed. It was found that there is a critical value of the decay-length of the heating and the base value of the heating, below which thermal equilibrium with a hot summit does not exist. This lack of thermal equilibrium is also present when the length of the field line is greater than a critical value. Hood and Priest (1979), Roberts and Frankenthal (1980) and Priest (1982) have been concerned with this kind of feature, suggesting that the system will evolve quasi-statically to a cool solution because of the catastrophic cooling. Based on this fact, and because the graphs $T_s(T_b)$ showed an apparent bend in the lower branch, attention was focussed on investigating the prominence-like solutions. The prominence properties, namely temperature and pressure were considered, and the thermal profiles were calculated by integrating the energy equation from the loop apex to the footpoint, from which the parameters L_*, h_* and s_* were determined.

On the other hand, a simplified cooling function was considered and this case allowed us to demonstrate that the lower branch exists. However, the lower branch

is not resolved numerically for a more accurate cooling function, such as, the one given by Hildner (1974).

Moreover, the stability of the uniform static solutions of the energy equation were studied up to the second order approximation, the results suggest that for the S-shaped type configuration in the graph $T_s(T_b)$ the upper and lower branches are stable and the middle branch is unstable. In addition, it was concluded that the linear approximation predicts that the instability depends on the size of the structure, but the second order approximation predicts that the stability or instability, additionally depends on the size of the structure and whether the disturbance decreases or increases the initial temperature.

Finally, the effect of the spatial variation of the heating but keeping the total energy input of the loop constant was studied. The results found in this case showed similar behaviour to those found when the total energy input was not kept constant when s_* was varied.

The next chapter will be concerned with the time-dependent evolution of the static structure studied here by means of numerical simulations.

Chapter 4

Thermal Evolution of Coronal Loops

4.1 Introduction

As was mentioned in Chapter 1, prominences consist of a cool and dense plasma which forms in the hot solar atmosphere. The study of the formation of prominences is tackled in two different ways. The first of these is related to the cooling and condensation of plasma, which is attributed to thermal instability and the second of these depends on dynamic effects. These two mechanisms are now discussed in turn.

In the coronal plasma, the loss of energy per volume by radiation C is proportional to the density squared and is a function of temperature, which increases with decreasing temperature in a certain temperature range (Cox and Tucker, 1969; Hildner, 1974). If one considers a small decrease in temperature an energy loss is presented since $\mathcal{L} > 0$ and so the plasma cools, thus causing a further reduction in the temperature. In a perturbed plasma, the temperature's disturbance will grow in time. Without any additional heating, the plasma cannot return to its initial state. Hence, an instability will result.

As can be seen in the form of the cooling function given by the equation (2.26), whenever $\alpha < 0$, a temperature drop will result in an increase in cooling and hence a thermal instability is possible. Notice also the effect of the plasma's density on the thermal instability. This can drive the thermal instability, since whenever the

density of the plasma increases, so too will the cooling.

The most common type of the instability found in the solar corona is the isobaric instability. This occurs when the instability evolves at constant pressure, since the plasma has time to set up flows that can balance the changes in pressure. The thermal instability mechanism continues until the plasma reaches a temperature of around 7,000 K at which a new equilibrium is reached since the radiative loss now decreases with decreasing temperature ($\alpha > 0$). The plasma's radiation becomes optically thick and thermal stability is achieved. The condensation by thermal instability has been studied analytically (Parker, 1953; Field, 1965; Chiuderi and Van Hoven, 1979; Van Hoven and Mok, 1984; An, 1985; 1986) and numerically (Hildner, 1974; Sparks et al., 1990).

Field (1965) studied analytically the condensation by this thermal instability. His work clarified the stability criteria and extended the linear analysis to include effects other than radiation loss such as magnetic fields, thermal conduction, rotation and density stratification. On the other hand, Oran et al. (1982), explored the non linear properties of thermal instabilities by numerical simulations. They found that the non linear regime is characterised by a bifurcation of the plasma into a cool dense condensation surrounded by a hot tenuous corona. Both of the work of Field (1965) and Oran et al. (1982) postulates the existence of a constant, uniform heating process.

The second way of prominences formation studies is related to dynamic mechanisms which can lead perturb plasma strong enough for the onset of thermal instability. An et al. (1988) investigated a chromospheric injection process but have demonstrated that this mechanism alone cannot account for quiescent prominence formation. Wu et al. (1990) extended the above work incorporating the effect of condensation and thermal conduction on the formation of prominences and concluded that such formation should be considered as a dynamic process, which needs both condensation and mass injection.

Choe and Lee (1992) showed that the increase of magnetic shear in an arcade produces an expansion of the structure and can create an initial adiabatic cooling. The radiative cooling function is locally increased leading to the onset of thermal instability and the condensation of coronal plasma.

Poland and Mariska (1986) considered a model in which an evaporative upflow of chromospheric material is produced by suppressing the coronal heating mechanism everywhere in the loop except at the footpoints. This forms an initial condensation in a dip at the top of the loop; however, the heating rate in the loop must be increased once the prominence has begun to form in order to supply sufficient mass.

Mok et al. (1990) modelled prominence formation in a coronal loop assuming that the heating has a spatial variation. The heating was taken to decrease with length along the loop and an energy imbalance at the loop summit led to an accelerating local isobaric cooling. They considered an one-dimension simulation with a full expression for the solar gravity. The prominence formed in the absence of a magnetic depression which was only added for support, after the condensation process had begun.

Van Hoven et al. (1992) extended the work made by Mok et al. (1990) adding a half dimension to the problem through the perpendicular motion of plasma and studied the dynamic formation and magnetic levitation of prominence. This occurs in two linear stages, beginning with the condensation of coronal plasma as a result of the modification of the energy supply, then proceeding with the mass load bending of the ambient magnetic field.

Antiochos and Klimchuk (1991) proposed a model for the formation of prominence condensations in hot coronal loops based on the heating being initially uniform, before being increased. The increment in the heating is spatially dependent, so that it is localised nearer to the chromospheric footpoints than the loop midpoint. They argued that increasing the heating causes cooling because the density increases due to evaporation such that the radiation losses at the loop midpoint surpasses the heating rate there, causing a catastrophic cooling and the formation of condensation.

Mendoza and Hood (1996) have also examined the prominence formation taking into account spatial dependence of the heating but studying the thermal equilibrium in order to find the critical parameters which can induce a quasi-static evolution up to the point where condensation forms. This evolution was also followed using a time-dependent numerical simulation.

In this chapter, results concerning the numerical simulation on the formation of prominence in a symmetric loop whose heating function has a spatial dependence are

presented. The effect of varying the parameters involved are investigated with strong emphasis on the variable related to the decay-length of the heating. The evolution of the thermal structures starting from different initial conditions is considered, and the analytical results obtained in Section 3.5 are confirmed by numerical solutions.

4.2 Basic Equations for the Thermal Evolution

The reduced equations (2.33)-(2.36) for a coronal loop in dimensionless quantities for the simplest case i.e., when gravity is zero, are:

$$\frac{\partial \tilde{\rho}}{\partial \tilde{t}} + \frac{\partial}{\partial \tilde{s}}(\tilde{\rho}\tilde{v}) = 0, \tag{4.1}$$

$$\gamma \frac{v_0^2}{c_s^2}\tilde{\rho}\left(\frac{\partial \tilde{v}}{\partial \tilde{t}} + \tilde{v}\frac{\partial \tilde{v}}{\partial \tilde{s}}\right) + \frac{\partial \tilde{p}}{\partial \tilde{s}} = 0, \tag{4.2}$$

$$\frac{1}{\gamma}\left(\frac{\partial \tilde{p}}{\partial \tilde{t}} + \tilde{v}\frac{\partial \tilde{p}}{\partial \tilde{s}}\right) + \tilde{p}\frac{\partial \tilde{v}}{\partial \tilde{s}} + L_*^2[\tilde{p}^2\tilde{\chi}\tilde{T}^{\alpha-2} - \tilde{h}] - \frac{\partial}{\partial \tilde{s}}\left(T^{5/2}\frac{\partial \tilde{T}}{\partial \tilde{s}}\right) = 0, \tag{4.3}$$

$$\tilde{p} - \tilde{\rho}\tilde{T} = 0, \tag{4.4}$$

where

$$\tilde{T} = \frac{T}{T_0}, \quad \tilde{p} = \frac{p}{p_0}, \quad \tilde{v} = \frac{v}{v_0}, \quad \tilde{s} = \frac{s}{L_0} \quad \text{and} \quad \tilde{\rho} = \frac{\rho}{\rho_0},$$

The physical quantities T_0, ρ_0, and $p_0 = \mathcal{R}\rho_0 T_0/\tilde{\mu}$ have been taken as typical coronal values. The variable L_0 is the half-length of the loop, $v_0 = L_0/\tau_0$ is the typical velocity and τ_0 is the conduction time-scale given by

$$\tau_0 = \frac{\gamma p_0 L_0^2}{(\gamma - 1)\kappa_0 T_0^{7/2}}.$$

The sound speed has been defined as $c_s = (\gamma p_0/\rho_0)^{1/2}$ and the heating function as described in Section 2.2 is given by

$$\tilde{h}(\tilde{s}) = h_* \exp(-\frac{\tilde{s}}{s_*}). \tag{4.5}$$

The dimensionless parameters L_*, h_* and s_* as well as $\tilde{\chi}$ have been defined in Section 3.2.

In the study for the present simulation, the heating (cooling) time will be assumed much longer than the pressure relaxation time. This means that density and temperature perturbations can be considered evolving in pressure equilibrium with their surroundings, so that one can consider that the sound speed c_s is much greater than the velocity v_0, and Equation (4.2) reduces to

$$\frac{\partial \tilde{p}}{\partial \tilde{s}} = 0. \tag{4.6}$$

A similar approach has been used by Meerson (1989) to describe the nonlinear evolution of thermally unstable disturbances in a plasma.

Therefore, taking $\tilde{p} = constant = 1$, equations (4.1)-(4.4) simplify to

$$\frac{\partial v}{\partial s} = \frac{\partial}{\partial s}\left(T^{5/2}\frac{\partial T}{\partial s}\right) - L_*^2\left[\chi T^{\alpha-2} - h_* \exp\left(-\frac{1-s}{s_*}\right)\right], \tag{4.7}$$

$$\frac{\partial T}{\partial t} = -v\frac{\partial T}{\partial s} + T\frac{\partial v}{\partial s}, \tag{4.8}$$

where the density has been eliminated by using (4.4) and all tildes have been omitted.

Similarly to the static case, Chapter 3, it is assumed that the loop is symmetric about the apex and therefore one needs to consider only one-half of the loop, i.e. from a footpoint to the summit.

The equations (4.7) and (4.8) are solved numerically with the following boundary and initial conditions

$$\begin{aligned} &\frac{\partial T}{\partial s} = 0, \quad v = 0 \quad \text{at} \quad s = 0, \\ &T = T_b \quad \text{at} \quad s = 1, \end{aligned} \tag{4.9}$$

$$v(s,0) = 0, \quad T = T(s,0) \quad \text{at} \quad t = 0. \tag{4.10}$$

In the next section the numerical results of the simulation will be presented.

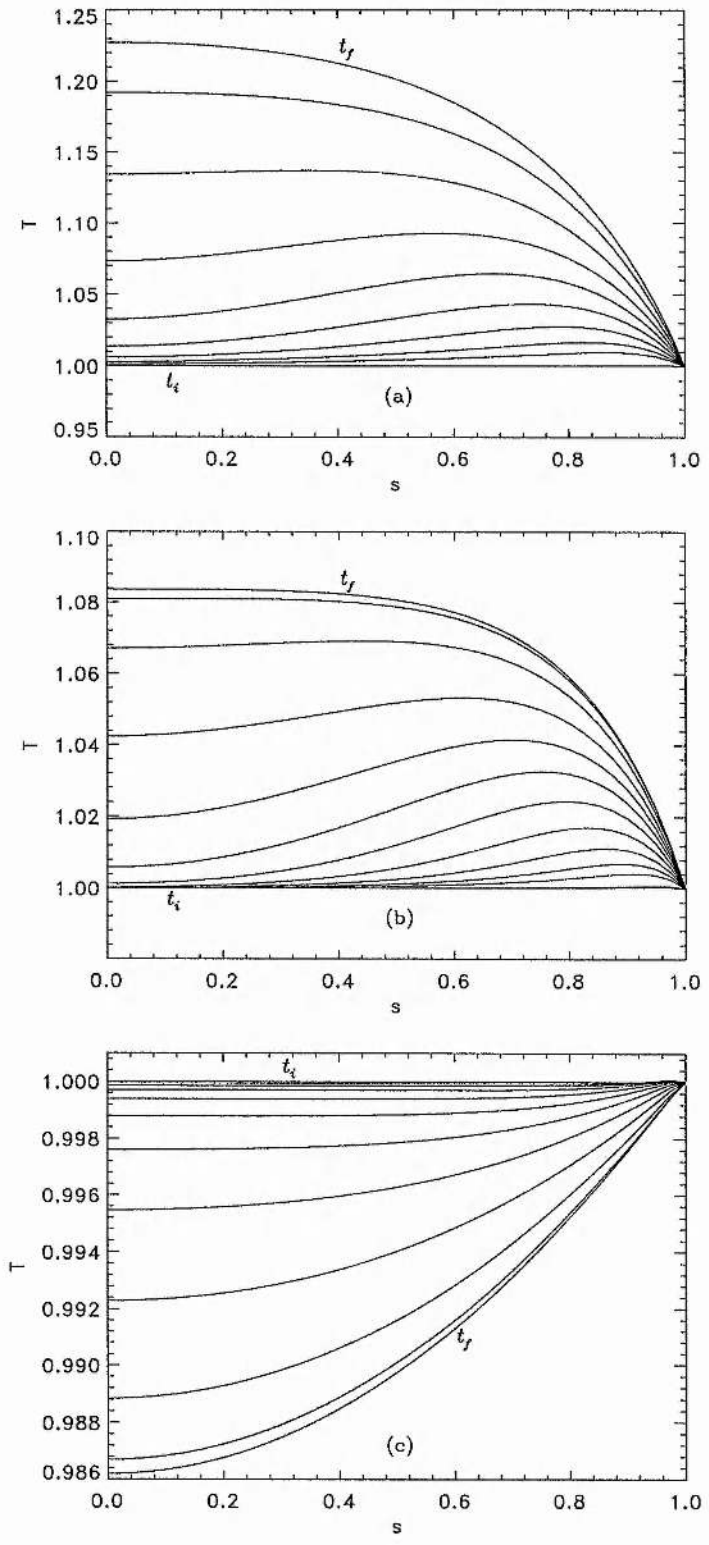

Figure 4.1: Temperature profile at selected times from t_i to t_f. For a) $s_* = 0.4$, b) $s_* = 0.2$ and c) $s_* = 0.01$.

4.3 Numerical Results

The solutions for T as a function of s and time for the initial state $T(s,0)$ and boundary conditions $T(1,t) = 1$ and $\partial T/\partial s(0,t) = 0$ were explored for a broad range of values of the parameters L_*, h_*, and s_*.

Figure 4.1 shows the temporal evolution of the temperature profile i.e. T as a function of s, for $L_* = 0.16$, $h_* = 101$ and for different values of s_*. These parameters correspond to a loop length of 3.5×10^7m, a heating of $10^{-4}\mathrm{Wm}^{-3}$. The parameter s_* decreases from Figure 4.1a to Figure 4.1c. When s_* is decreased, the final temperature profile has a lower temperature at the summit. It is apparent in this figure that for $s_* = 10^{-2}$ the lowest temperature profile obtained at the end of the evolution has a summit temperature at coronal values.

The value of L_* was increased, keeping the other parameters fixed. A critical value of L_* was found for which a hot summit was no longer obtained. In order to see this effect Figure 4.2 shows the summit temperature as a function of L_* (the heating has been neglected for simplicity).

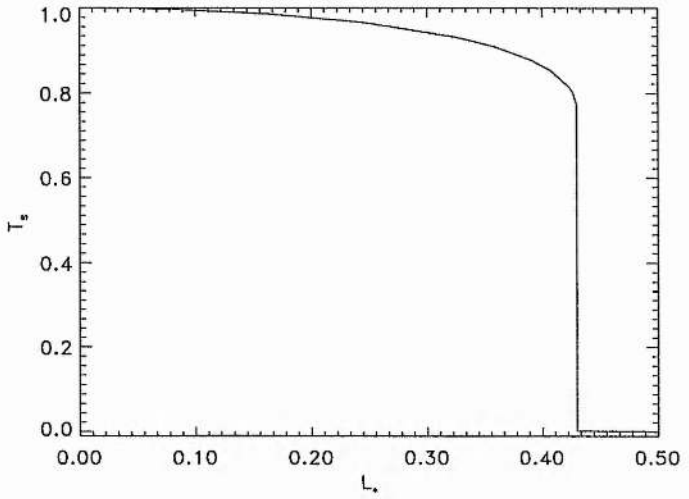

Figure 4.2: The summit temperature T_s as a function of the parameter L_* for a special case when the heating term is neglected.

It is observed that the summit temperature is hot when $L_* < L_{*c}$, but for values greater than this critical value the temperature drops to a cool summit.

In Figure 4.3 the temporal behaviour of the temperature profile is plotted for

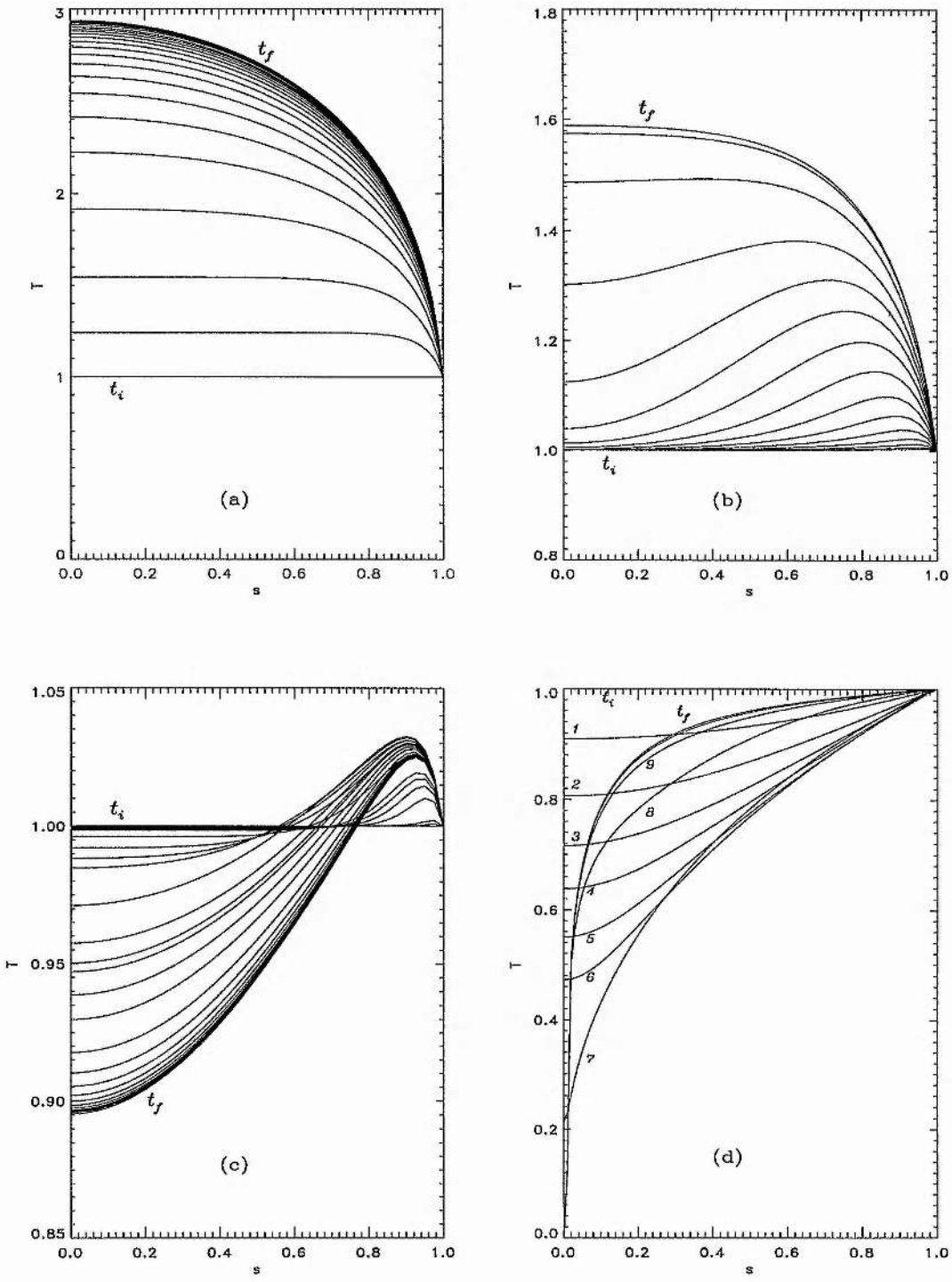

Figure 4.3: Temperature profiles at selected times from t_i to t_f. For a) a large value of s_*, b) $s_* = 0.23$, c) $s_* = 0.05$ and d) $s_* = 0.01$.

$L_* = 4.8 \times 10^{-1}$, $h_* = 101$, and for different values of s_*.

Similarly (as was shown in Figure 4.1), the final temperature profile in Figure 4.3 has a lower summit temperature when s_* is decreased. It is also found that when $s_* < s_{*c}$ ($s_{*c} = 4.3 \times 10^{-2}$ is the critical value below which no static hot solution is found for the particular boundary conditions) the temperature, starting from coronal values, begins to decrease smoothly, but at a time $t = 5$ the temperature at the summit sharply decreases (Figure 4.3d). This cooling is evident in Figure 4.4 where the evolution of the temperature at the summit is shown for the case $L_* = 4.8 \times 10^{-1}$, $h_* = 101$ and $s_* = 1.0 \times 10^{-2}$.

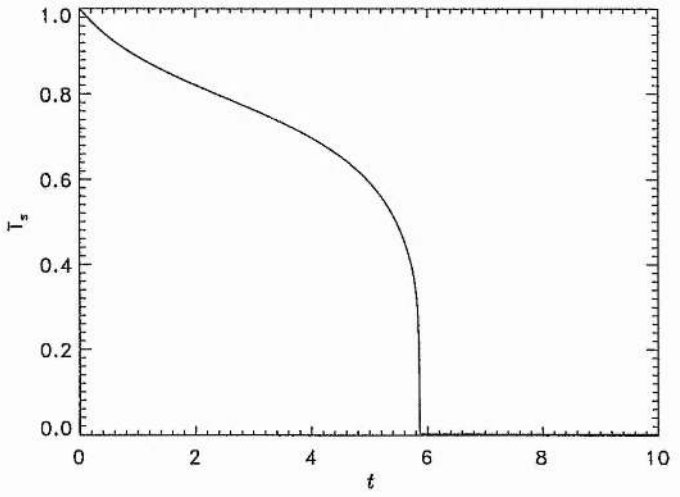

Figure 4.4: Evolution of the summit temperature T_s for $s_* = 0.01$.

It is interesting to note that when simulations are done for $s_* < s_{*c}$ the final states obtained are steady and not static. These results have also been noted by Mok et al. (1990), Van Hoven et al. (1992), Antiochos and Klimchuk (1991). In order to reach static thermal structures in the loop a further increase of the heating rate, by increasing the value s_*, is required. This requirement has also been noticed by Van Hoven et al. (1992). In this simulation the increment of the decay length of the heating s_* has to be greater than critical value s_{*c} (which correspond to values of the parameter s_* where a static solution at hot summit can be found as discussed in Chapter 3).

Figure 4.5 shows the evolution of the temperature at different locations in the loop. In this figure the heating function is changed by modifying the decay-length

of the heating. One starts with the initial value $s_* < s_{*c}$ ($s_* = 3.7 \times 10^{-2}$). The summit temperature decreases smoothly from coronal values during time $t < 12$. When $t \sim 13$ the summit temperature decreases significantly from coronal values. The heating is increased by increasing the value of s_* to 4.43×10^{-1} and the loop finally finds a static state (after $t \sim 15$). The summit temperature $T(0)$, as can be seen in Figure 4.5, shows no significant change. At other locations between the summit and the footpoint, the temperature variation with time is very small for a time $t < 14$, but when the system receives an increase in the heating, the temperature configuration noticeably changes. The temperature increases until the system finds thermal balance after $t \sim 15$.

It is important to remark here that after the condensation is formed it is quite stable even when the decay length of the heating is increased.

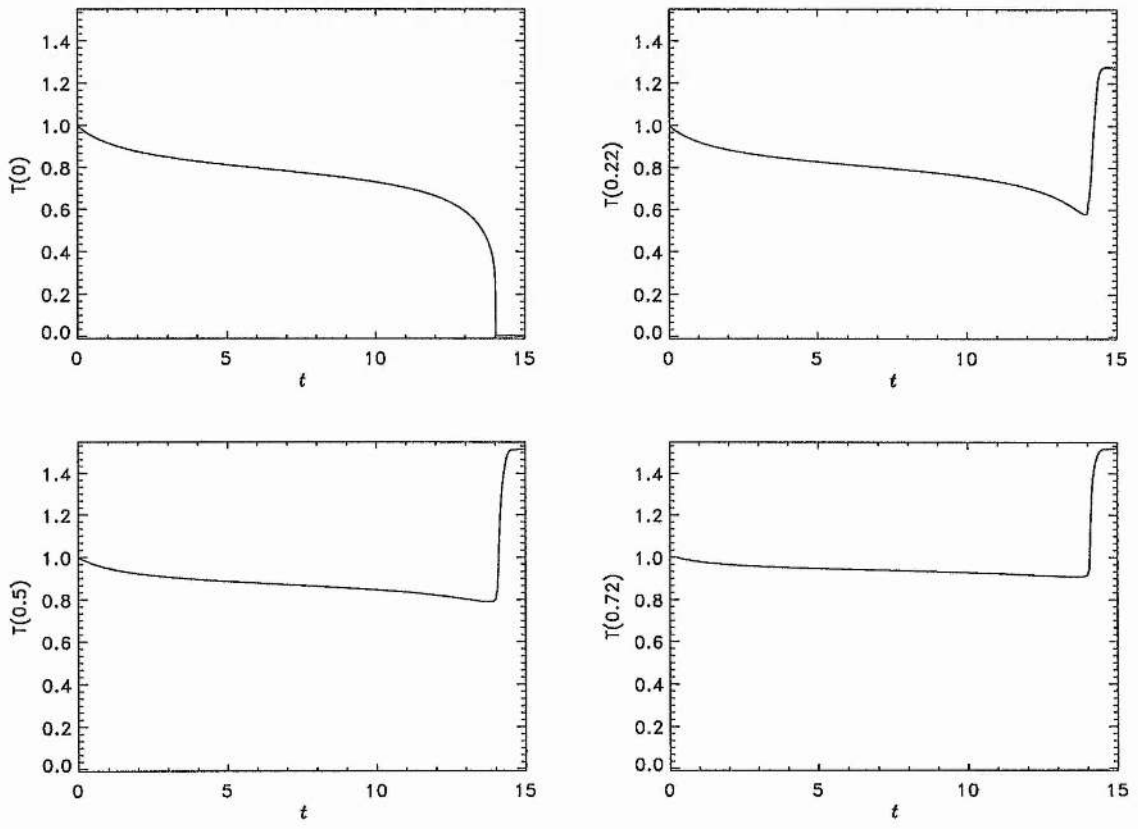

Figure 4.5: Evolution of the temperature at different locations along the loop.

It is believed that static final solution exist when $s_* < s_{*c}$ and could be found

due to the results obtained in Chapter 3 when a simplified cooling function was considered. The problem here is due to the fact that the time dependent code cannot resolve the final solution with the full cooling function given by Hildner (1974).

Almost certainly the same problem is encountered by Van Hoven et al (1992) since they must increase the heating through an increase of s_*. Antiochos and Klimchuk (1991) also presented this difficulty when they reached a steady state solution after formation of a condensation and their simulation breaks down. Due to the difference between their form of the heating function and the function used in this simulation no direct comparison can be done.

Other authors have found this kind of solution: for example, Choe and Lee (1992) obtained a prominence solution that is not in static equilibrium, and believe that this is due to a dynamic interaction of the prominence with its surroundings. We believe that it is a numerical artifact and that there is no steady equilibrium unless the heating is subsequently increased. The lack of physical steady flow comes from the fact that mass continuity equation implies $\rho v = constant$ in space since $\partial\rho/\partial t = 0$, however, the summit boundary condition implies that the velocity is zero everywhere.

4.4 Numerical simulation using different initial conditions

In this section different initial conditions are taken in order to study how the temperature profile evolves to different final solutions.

It is likely that two final static solutions exist for given values of the parameter L_*, h_*, and s_*. In Chapter 3 it was shown that multiple solutions exist to the static energy equation. For example, consider an initial temperature profile of the form

$$T(s,0) = (T_{ch} + T_{cor} + (T_{cor} - T_{ch})\tanh(b(s - b_0)))/2, \tag{4.11}$$

where T_{ch} and T_{cor} are temperature values at the summit and the footpoints respectively, b_0 is the translation point, and b the parameter that governs the steepness of the temperature transition from T_{ch} to T_{cor}. This is not in equilibrium. However, the effect of considering the above initial condition and following the evolution of

the system to the final static state can be seen in Figure 4.6.
This shows the evolution of the temperature profile as a function of s for different times, where $L_* = 0.48, h_* = 101$ and $s_* = 4.43 \times 10^{-1}$.

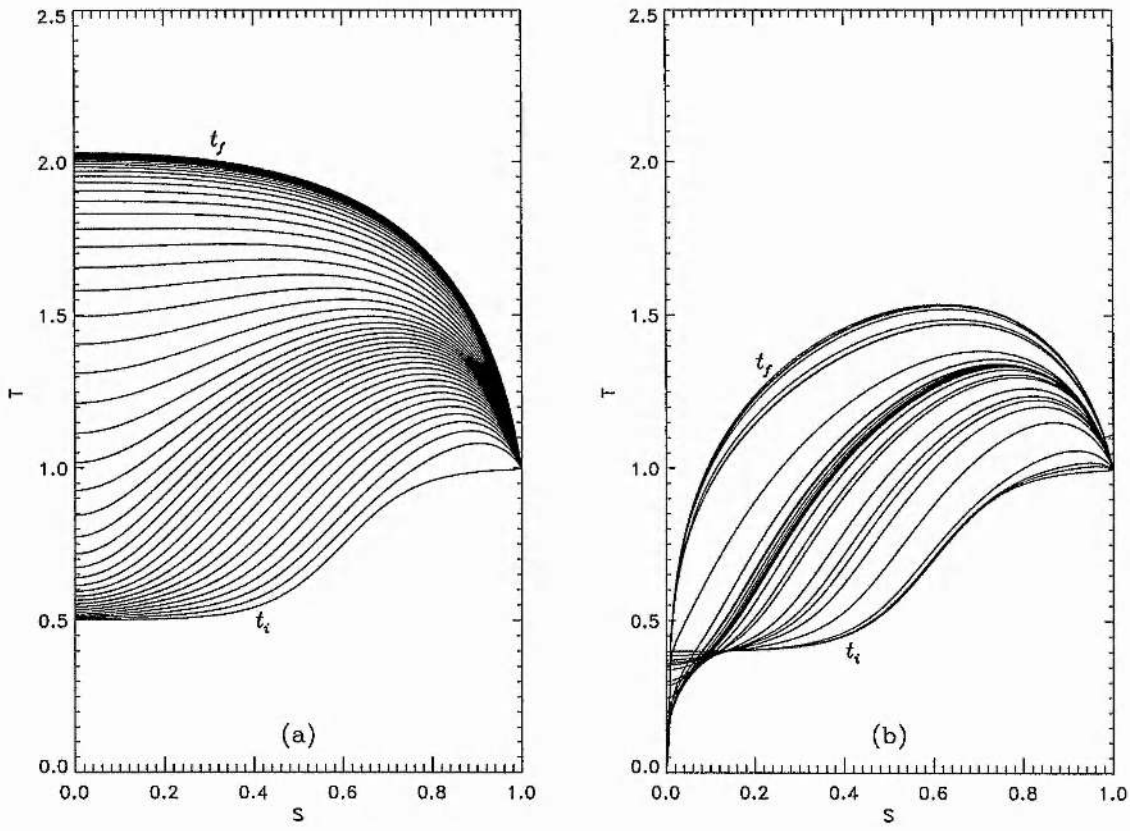

Figure 4.6: Temperature profiles at selected times from t_i to t_f starting with different initial conditions.

The initial conditions were $T_{ch} = 0.5$ and $T_{cor} = 1$ in Figure 4.6a, and $T_{ch} = 0.4$ and $T_{cor} = 1$ in Figure 4.6b.

From Figure 4.6a one can see that the temperature profile evolves to a final state with a hot summit. But, a cool summit is obtained when the second initial condition is taken (see Figure 4.6b). Obviously there is an unstable equilibrium with a summit temperature near $T_{ch} = 0.45$.

Figure 4.7 plots the final temperature profiles, after considering different initial conditions, for different values of s_*. Figure 4.7a shows the final temperature profiles already obtained in Figure 4.6. Figures 4.7b - 4.7d correspond to $s_* = 0.23$, 0.20, and 0.19 respectively. These figures have been plotted using different values for T_{ch}

and T_{cor} corresponding to the suitable values to allow the evolution to firstly a hot and secondly a cool summit.

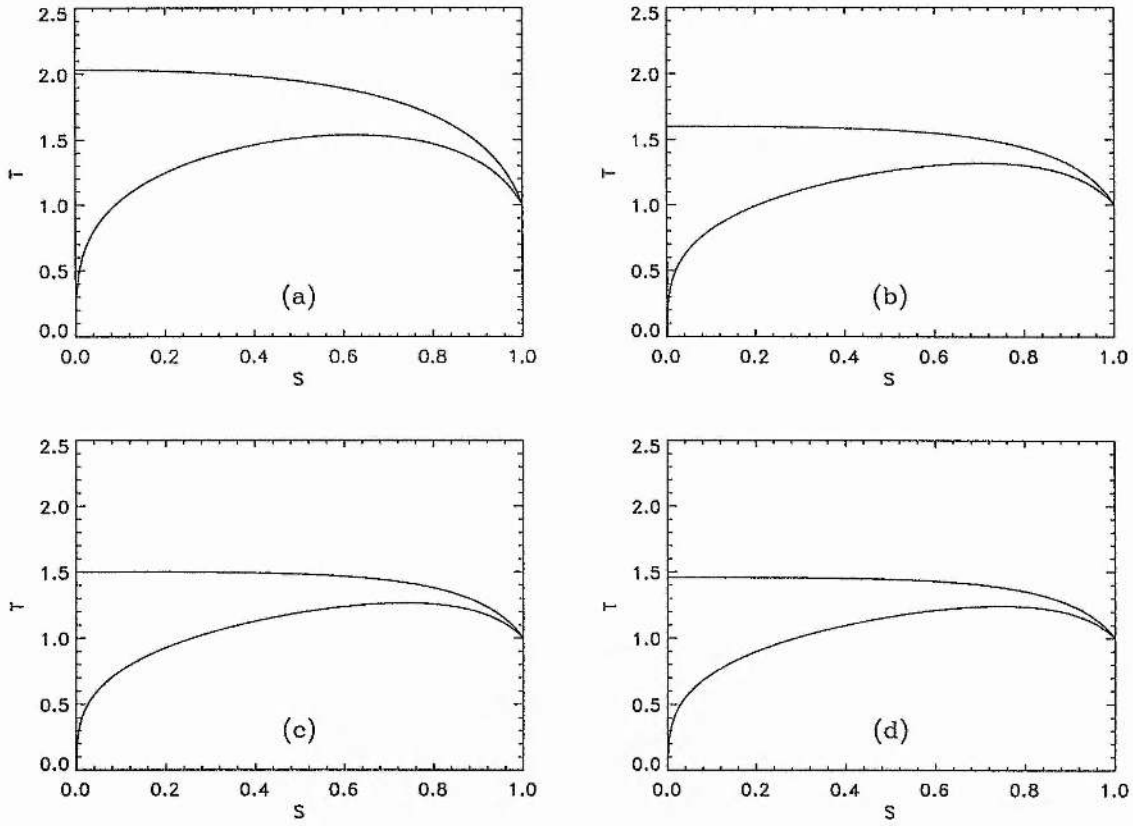

Figure 4.7: Final temperature profile for other values of the decay length of the heating with $s_* =$ a) 0.44, b) 0.23, c) 0.20 and d) 0.19.

It is likely there exists a threshold initial profile as an initial condition in which one could say a marginal initial condition exists. By using a mechanical analogy one can explain schematically how this process occurs. The system represented in Figure 4.8 by a black sphere can either increase or decrease its temperature depending on whether it moves to the right or to the left side respectively. The two potential wells at T_c and T_h would represent two stable solutions with cool and hot summits respectively.

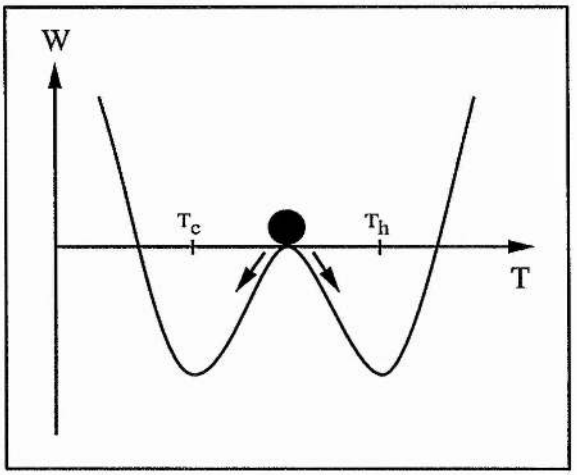

Figure 4.8: Schematic potential curve showing the stable states at T_c and T_h.

4.5 Thermal Evolution of a Structure

Section 3.5 was concerned with the analytical analysis of the stability of the energy equation. Some criteria for thermal instability were obtained. Additionally, it was found that the response of the thermal structure not only depends on the amplitude of the disturbance, but also on whether the disturbance increases or decreases the initial static temperature.

In this section the evolution of a thermal structure will be examined numerically for different values of the parameter L_*. Here, the simplified cooling function which has been discussed in the Section 3.4, and a constant heating function are considered. This study allows us to introduce a physical quantity which can be expressed in terms of its unperturbed and perturbed quantity as

$$T = T_e + T_p, \tag{4.12}$$

where T_e is the temperature equilibrium considered as the trivial solution $T_e = 0.138$ and $T_p = \epsilon\, T_e \cos(\pi s/2)$ (ϵ being the perturbation amplitude which can be positive or negative).

4.5.1 Evolution for $L_* > L_c$

As mentioned in Section 3.4, when $L_* > L_c$, three possible solutions exist. One of the solutions is the trivial solution T_e, which is located in the middle branch. The first approximation of the stability analysis predicts that the trivial solution is unstable, but the second order approximation presents two possibilities for the evolution depending on whether the perturbation is positive or negative. The perturbed solution would then evolve towards its saturated states i.e., to the stable solution.

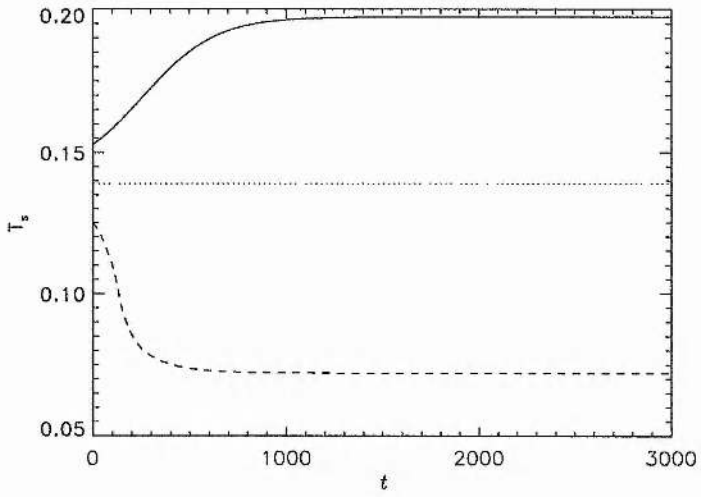

Figure 4.9: The summit temperature T_s as a function of time for $L_* > L_c$.

Figure 4.9 shows the plot of the summit temperature as a function of time for an increase (solid line) or decrease (dotted line) of temperature. When $\epsilon = +0.1$ the summit temperature T_s starts to rise until it reaches a saturated state which corresponds to the static solution found in section 3.4. The value of ϵ was increased and reduced from this value but the separation from the trivial solution T_e (dotted line) was still observed.

However, when the temperature was reduced by considering $\epsilon = -0.1$ in Equation 4.12 the summit temperature began to decrease further from the trivial solution reaching a lower temperature value. This value corresponds to the lowest temperature found in section 3.4 which represents a non-isothermal profile. Therefore, the isothermal solution T_e is unstable for $L_* > L_c$.

4.5.2 Evolution for $L_c' < L_* < L_c$

For $L_c' < L_* < L_c$ (see, Section 3.4, p.64 for definitions of L_c' and L_c), the thermal structure again presents three possible solutions; one isothermal solution T_e, and two non-isothermal with summit temperature $T_s < T_e$.

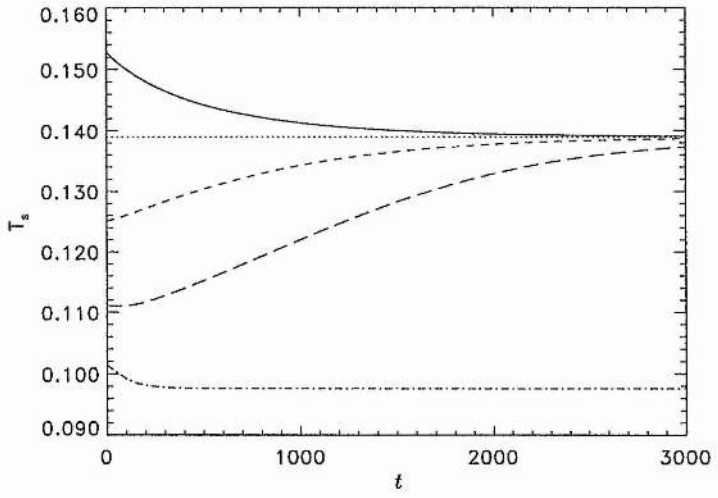

Figure 4.10: The summit temperature T_s as a function of time for $L_c' < L_* < L_c$.

If the temperature is increased when $\epsilon = +0.1$, the summit temperature decreases with time, approaching asymptotically to the trivial solution T_e as can be seen in Figure 4.10 for the case plotted with solid line. On the other hand, if $\epsilon = -0.1$, the dashed line in Figure 4.10 shows that the temperature increases, approaching the trivial solution T_e (dotted line).

The magnitude value of ϵ was reduced and a threshold value was found for which the temperature instead of increasing, decreased towards a lower value (dotted-dash line). This lower value of the summit temperature corresponds to the value found in the lower branch in Figure 3.12 of Section 3.4. Therefore, the trivial solution as well as the lowest temperature are stable solutions to the energy equation.

4.5.3 Evolution for $L_* < L_c'$

In this interval of L_* the graph $T_s(T_b)$ plotted in Figure 3.12 shows a monotonic increasing function of T_b. If one perturbs the temperature positively, it decreases

asymptotically to the trivial solution as can be seen in Figure 4.11. Furthermore, if larger values of ϵ are considered, the same result is obtained. On the other hand, when $\epsilon = -0.1$ is considered, the summit temperature increases towards the trivial solution. This value of ϵ was increased negatively and the summit temperature increased asymptotically to the trivial solution. Therefore, T_e presents a stable behaviour when positive or negative disturbances of different amplitude are considered.

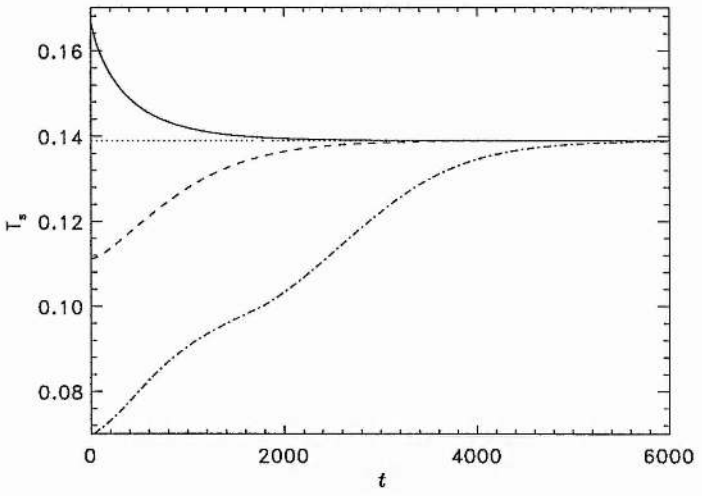

Figure 4.11: The summit temperature T_s as a function of time for $L_* < L_c'$.

4.5.4 Evolution for $L_* = L_c$

In this case the trivial solution for the critical value of L_* is disturbed by increasing the temperature above T_e with $\epsilon \geq +0.1$. Figure 4.12 shows that the summit temperature decreases asymptotically, returning to the equilibrium value T_e. But, if it is decreased below T_e, namely with $\epsilon \leq -0.1$, the temperature will fall further reaching a low value of T_s.

In Section 3.5 this case was studied analytically up to the second order approximation. This trivial solution is marginally stable to the linear approximation, but, if one considers a second order approximation, it is quadratically unstable (Hood and Priest, 1979). The Landau constant a_2 for a positive perturbation is always negative and the temperature will return to the isothermal solution. However, when negative disturbances are considered, the Landau constant a_2 is positive, so that the temperature will drop and the gas cools.

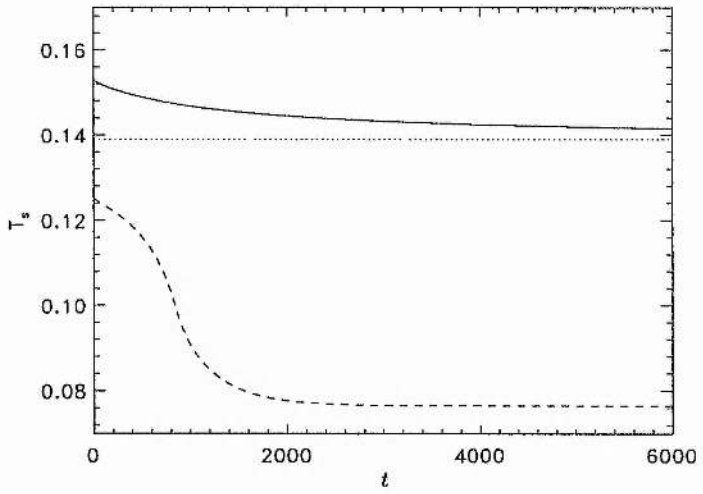

Figure 4.12: The summit temperature T_s as a function of time for $L_* = L_c$.

4.6 Summary of the Chapter

This chapter has investigated the formation of cool (prominence-like) condensations in a symmetric coronal loop when the heating function depends on the spatial deposition of the heat. This form of heating function is based on the damping of waves, so the energy deposited in the loop decays from the footpoints. Its form was taken as exponential and the evolution of the loop due to different decay lengths was investigated.

It was found that the temperature at the apex decreases when the decay length of the heating is decreased up to a critical value where the decreasing of the temperature is not significantly different from coronal values. But if s_* is taken to be less than a critical value, namely s_{*c}, the temperature drops further, away from coronal values to chromospheric values.

In the formation of this condensation, it was observed that the final numerical result was not a static solution. In order to reach a static solution the heating was increased by increasing the value of s_*.

Several simulations were done in order to understand the behaviour of these condensations and it was found that they are remarkably stable when s_* was increased. In addition, it is interesting to note that for the same value of s_*, a hot summit can be found as well as a cool summit; therefore, simulations with different initial

conditions were considered and it was observed that the temperature increased or decreased according to whether the initial profile was above or below a threshold one.

This result stresses the importance of this form of heating function for the formation of cool condensations because the drop in temperature requires only that the decay-length of the heating is smaller than a critical value. This condition can be obtained by, for example, decreasing the damping length of Alfvén waves due to increasing magnetic shear (Mok and Einaudi 1985)

Furthermore, in this chapter the results obtained by analytical analysis of the thermal stability equations (Section 3.5) were verified by numerical simulations. These results also agree with the results obtained in Section 4.4 for which different initial conditions can affect the evolution of a thermal structure. It is also important to mention here that despite the fact that the simulations were done with a simplistic code, in which the inertial terms were assumed small, it was still possible to follow the evolution of the system from a hot plasma to the formation of a prominence using only a small amount of computational memory and time .

Chapter 5

The Thermal Equilibria of Hydrostatic Coronal Loops

5.1 Introduction

In Chapter 3 it was argued that gravity had a small effect so that the thermal structure of loops can be studied at constant pressure. However, for long loops, i.e. greater than the pressure scale height, gravity must be considered.

In the study of the thermal structure of coronal loops, different basic processes have been taken into account. Rosner et al. (1978), Hood and Priest (1979), Craig et al. (1978), Hood and Anzer (1988), Steele and Priest (1990a) have modelled loops for which solar gravity can be neglected. In this category Hood and Anzer (1988), Steele and Priest (1991a) included the effect of cross-section area variation. Steele and Priest (1990b, 1991b) included the consideration of a coronal arcade rather than simple loop.

The effect of solar gravity was included by Vesecky et al. (1979), Wragg and Priest (1981), Serio et al. (1981), She et al. (1986), Hood and Anzer (1988) and Steele and Priest (1994)

Vesecky et al. (1979) studied the thermal equilibrium of coronal loops numerically, including both area variation and the effect of gravity. They found that increasing the variation in cross section decreases the summit temperature. The base temperature was taken to be as low as 10^4K and the base conductive flux was

assumed to vanish there.

Wragg and Priest (1981a, 1981b, 1982) solved the thermal equilibrium equations with gravity included, extending the work by Hood and Priest (1979). Their calculations were concerned with hot equilibrium and the absence of it under certain circumstances. They also studied the effect of the loop's geometry and field line divergence.

Serio et al. (1981) extended the work of Rosner et al. (1978) by including gravity and considering a spatially dependent heating. They derived a scaling law similar to that found by Rosner et al. (1978), which related the base pressure (p_0) and loop length (L) to the base heating (h_0), the heating deposition (s_H) and the pressure scale height (Λ), as

$$T_s \approx 1.4 \times 10^3 (p_0 L)^{1/3} \exp\left[-0.04L(2/s_H + 1/\Lambda)\right]$$

for the summit temperature and the heating

$$h_0 \approx 10^5 p_0^{7/6} L^{-5/6} \exp\left[0.5L(1/s_H - 1/\Lambda)\right]$$

They examined two classes of loops, those with a temperature maximum at the summit and those loops which have a local temperature minimum at the summit.

She et al. (1986) investigated the quasi-static thermal structures of loops, but especially put emphasis on the effects of the chromosphere-corona transition zone on the determination of the possible thermal states. They also looked for plasma condensations.

Hood and Anzer (1988) studied the effect of gravity on the thermal equilibrium solution by using a phase plane diagram. They considered simplified energy and hydrostatic equations and concluded that gravity is a hindrance in getting prominence-like solutions.

Steele and Priest (1994) solved the equation for thermal equilibrium along a coronal magnetic loop with constant cross-sectional area and in the presence of gravity. They used a phase volume diagram because the inclusion of gravity makes the pressure fall along the loop from footpoint to summit and therefore the pressure is considered on its own as a free parameter. This phase volume is formed from an

infinite number of phase planes, each at a constant pressure. They found that the effect of the gravity is to reduce the number of solutions available. The most affected were the prominence-like solutions (hot-cool loops).

The hydrostatic thermal equilibrium have also been investigated for stellar coronal loops (Landini and Monsignori Fossi 1975, 1981; Collier-Cameron 1988). Collier-Cameron (1988) studied the thermal equilibrium on a rapidly rotating lower main-sequence star and found two types of loop solutions namely, hot and warm loops.

In the present chapter the temperature structure along a coronal magnetic loop is studied in the presence of gravity. The cross-sectional area is considered constant and a heating function which decays with altitude is assumed. Since one of the motivations in this thesis is to model prominences, great emphasis will be put on finding those solutions which give hot-cool loops.

5.2 Hydrostatic Thermal Equilibrium

When the condition of constant pressure is relaxed, the variation of temperature and pressure along a loop obeys the equations for hydrostatic equilibrium and the energy equation. To obtain the temperature and the pressure profiles along the loop one has to solve the dimensionless equations numerically

$$\frac{dp}{ds} = \frac{p}{T} g(s), \tag{5.1}$$

$$\frac{d}{ds}\left(T^{5/2}\frac{dT}{ds}\right) = L_*^2\left[p^2\chi T^{\alpha-2} - h_* \exp\left(-\frac{1-s}{s_*}\right)\right], \tag{5.2}$$

with boundary conditions,

$$\begin{aligned} &\frac{dT}{ds} = 0 \qquad \text{at} \qquad s = 0 \qquad \textit{summit}, \\ &T = T_b, \qquad p = p_b \qquad \text{at} \qquad s = 1 \qquad \textit{footpoint}, \end{aligned} \tag{5.3}$$

where $g(s)$ represents the component of solar gravity along the magnetic field. The obvious consequence is that the pressure is no longer constant and that it must decrease along the loop from footpoint to summit.

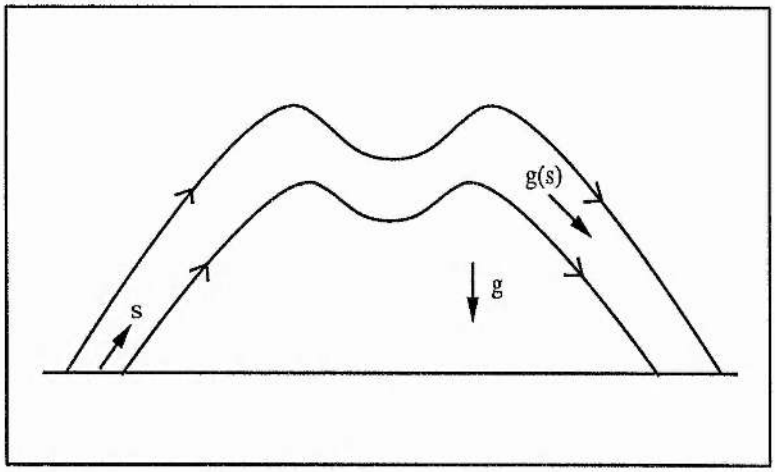

Figure 5.1: Schematic drawing of the magnetic field configuration, indicating the component of the solar gravity.

Figure 5.1 shows the structure of the loop. As mentioned in Section 2.3, it is assumed that the gravity has two components, one describing the general semicircular shape of the field and is given by

$$\frac{L_0}{\Lambda} \sin \frac{\pi}{2} s,$$

where L_0 is the half-length of the loop and Λ is the gravitational scale-length, and the other component represents a dip containing a cool condensation and is discussed in Section 5.3.2.

5.3 Numerical Results

5.3.1 General Features

Figure 5.2 shows the temperature and pressure as a function of the position s from the summit to the footpoint, for fixed values of $L_* = 0.48$, $h_* = 101$ and $s_* = 0.05$. The asymptotic case when gravity is zero ($g = 0$) is also shown. Two solutions can be obtained in both cases: one with high temperature and another with a lower temperature at the summit (see Figure 5.2a). Hood and Anzer (1988) and Steele and Priest (1994) have also found two solutions in their modelling. The curves with solid lines correspond to the case when $g = 0$. It can be seen in this figure that when

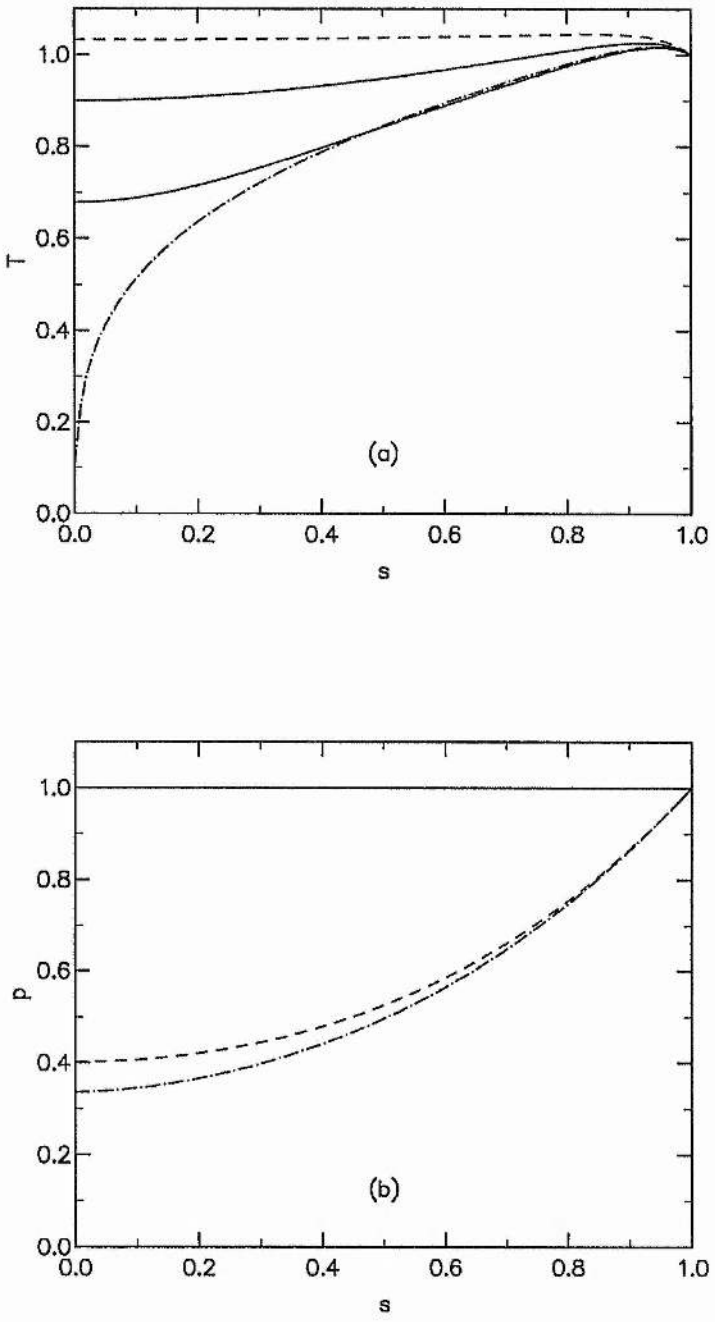

Figure 5.2: Temperature (a) and pressure (b) profiles For $s_* = 0.05$. The solid line correspond when gravity is zero. The dashed and dash-dotted line correspond to the case with gravity.

gravity is switched on, the hotter solution increases the summit temperature and the cooler solution decreases the summit temperature, in comparison to the respective solution with $g = 0$. The pressure, as was expected, increases with s from the summit to the footpoint as can be seen in Figure 5.2b.

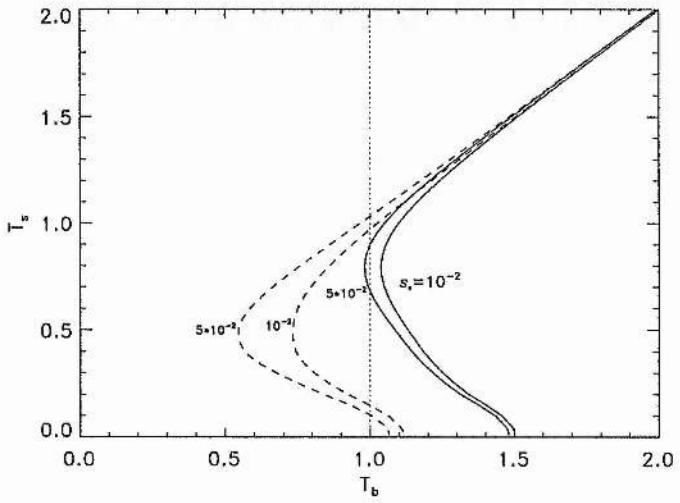

Figure 5.3: The summit temperature T_s as a function of the boundary temperature T_b for two values of the decay length of the heating s_*. The solid and dashed lines show families of solutions with no gravity and with gravity respectively. The dotted line indicates the particular boundary condition $T_b = 1$.

Figure 5.3 shows the summit temperature T_s as a function of the base temperature T_b. It can be seen how the effect of including gravity is to cause the turning point to move towards the left side of T_b where thermal equilibrium is found if particular boundary conditions are assumed.

In particular, for the given values of the parameters L_*, h_*, s_* and the boundary condition $T_b = 1$ (which corresponds to a typical coronal value), for $s_* = 1.0 \times 10^{-2}$, no solution is found when gravity is zero, but when gravity is taken into account there are two solutions. For $s_* = 5.0 \times 10^{-2}$ the two solutions are shifted, the hot one to a higher value and the cool one to a lower value of T_s. From this result, it can be deduced that when gravity is included, a smaller value of s_* is necessary in order to find a critical value of s_* below which no hot solution exists. Hence, under hydrostatic equilibrium the pressure falls off with altitude and makes the equilibrium

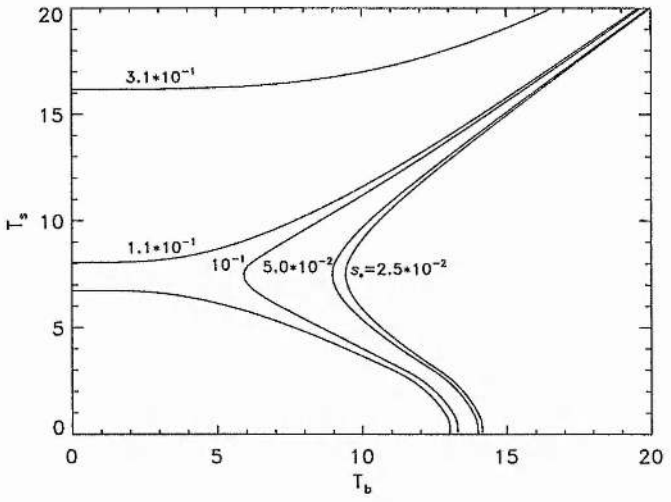

Figure 5.4: The summit temperature T_s as a function of the boundary temperature T_b for different values of the decay length of the heating s_*. Parameters used are $L_* = 1248.0$ and $h_* = 3.96 \times 10^{-2}$, normalised at chromospheric values. Temperatures are given in units of 10^5K.

move further away from critical conditions.

The general features described for constant pressure (Chapter 3) are also presented when gravity is included, as seen in Figures 5.4 and 5.5, where the summit temperature is plotted as a function of the boundary temperature for various values of the parameters s_* (Figure 5.4) and h_* (Figure 5.5).

In Figure 5.4 and 5.5 it is clearly seen that the turning points shift to the left when s_* and h_* are increased, respectively. As discussed in Chapter 3, it is noticeable that there is a bend in the lower branch of the curves, suggesting the existence of an even lower branch.

5.3.2 Hydrostatic Thermal Equilibrium with a Magnetic Dip

The thermal balance of loops has been studied by assuming that the magnetic configuration of the loop is specified through the function $g(s)$ which is the component of the gravity along the field line. This function $g(s)$ for a semicircular loop has already been investigated in the previous section. In this section, we are interested in

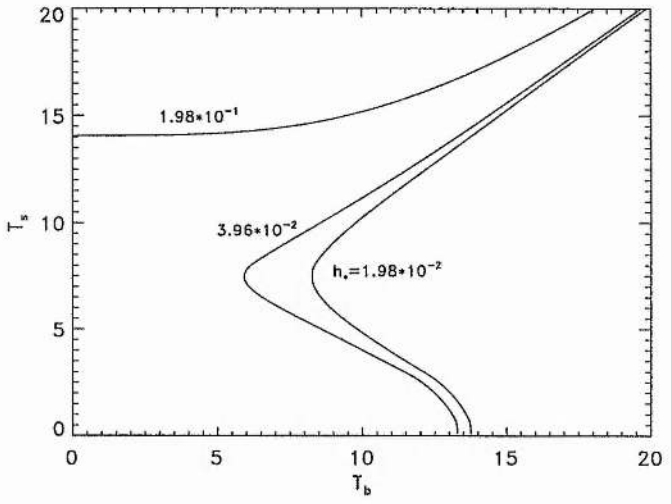

Figure 5.5: The summit temperature T_s as a function of the boundary temperature T_b for different values of the heating deposition h_*. Parameters used are $L_* = 1248.0$ and $s_* = 5.0 \times 10^{-2}$.

focussing our attention on the effect of a dip on the magnetic configuration, which is of great importance for supporting prominences material (Kippenhahn and Schlüter 1957; Kuperus and Raadu 1974). A number of models of prominence formation showing the additional effect of the dip have been presented by several authors (Poland and Mariska 1986; Mok et al. 1990; Antiochos and Klimchuk 1991; Van Hoven et al. 1992).

Poland and Mariska (1986) constructed the initial equilibrium with a gravitational potential well at the midpoint whereas other authors viz., Mok et al. (1990) and Van Hoven et al. (1992) added the distortion of the projected gravitational force as the condensation forms. In particular, it was added when a substantial condensation (with density $\gtrsim 5$ times the nearby coronal value) formed. Mok et al. (1990) also found prominence formation without dip and argued that it was not clear in Poland and Mariska's case whether the reversed gravity is essential to draw the plasma to the centre during the condensation process.

In this section the hydrostatic model is employed and the effect of a dip on the magnetic configuration is studied. Now, the gravity component with a dip can be expressed as

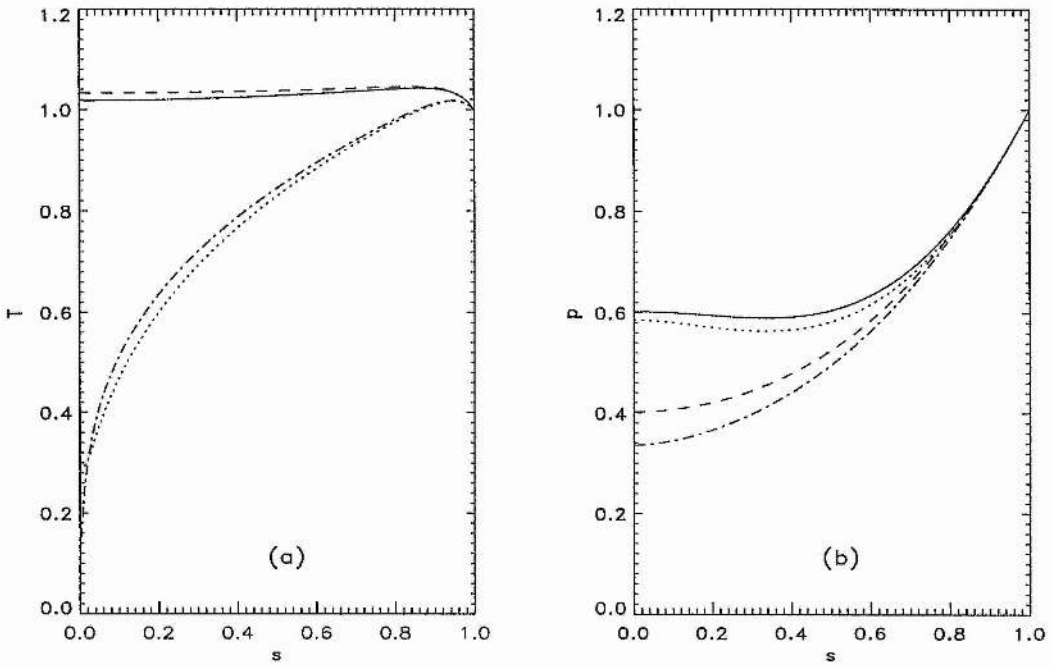

Figure 5.6: Temperature and pressure profiles for the case when a dip is included. The solid line and dotted line correspond to gravity with dip, and dashed and dash-dotted line to gravity without dip.

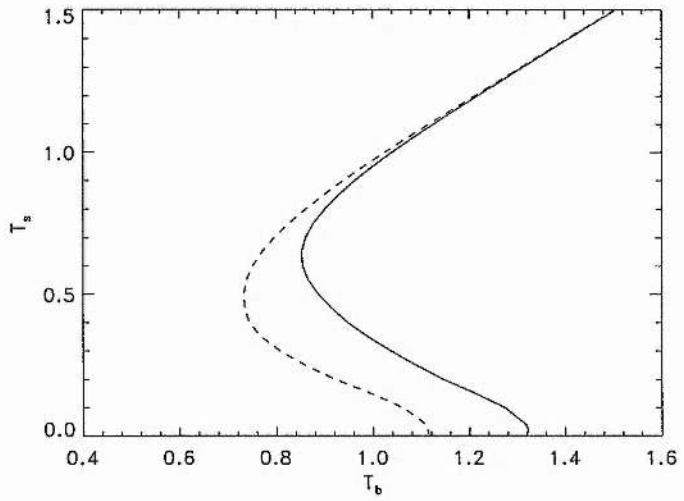

Figure 5.7: The summit temperature T_s as a function of the boundary temperature T_b for the case gravity without dip (dashed line) and with dip (solid line).

$$g(s) = \frac{1}{1+g_1}\frac{L_0}{\Lambda}\left(\sin\frac{\pi}{2}s - g_1 \sin\frac{3\pi}{2}s\right)$$

where the second term simulates the dip and g_1 is the amplitude of the distortion which is taken in this thesis as $g_1 = 0.5$.

Figure 5.6 shows the temperature and pressure profiles for a particular case when $L_* = 0.48$, $h_* = 101$ and $s_* = 0.05$. In this figure the case of gravity without dip has also been plotted for comparison. Two solutions have been found. The curves with dashed and dash-dotted lines correspond to solutions where the dip is neglected. It can be seen in this figure that when the dip is included the solution with a hot summit has a slightly lower temperature, when compared with the respective solution without dip. The pressure presents an interesting behaviour, as it first decreases from the footpoint and then increases close to the summit. This is expected when the dip is considered, because the gravity changes sign close to the summit. For this case the change of sign occurs at $s = 0.33$.

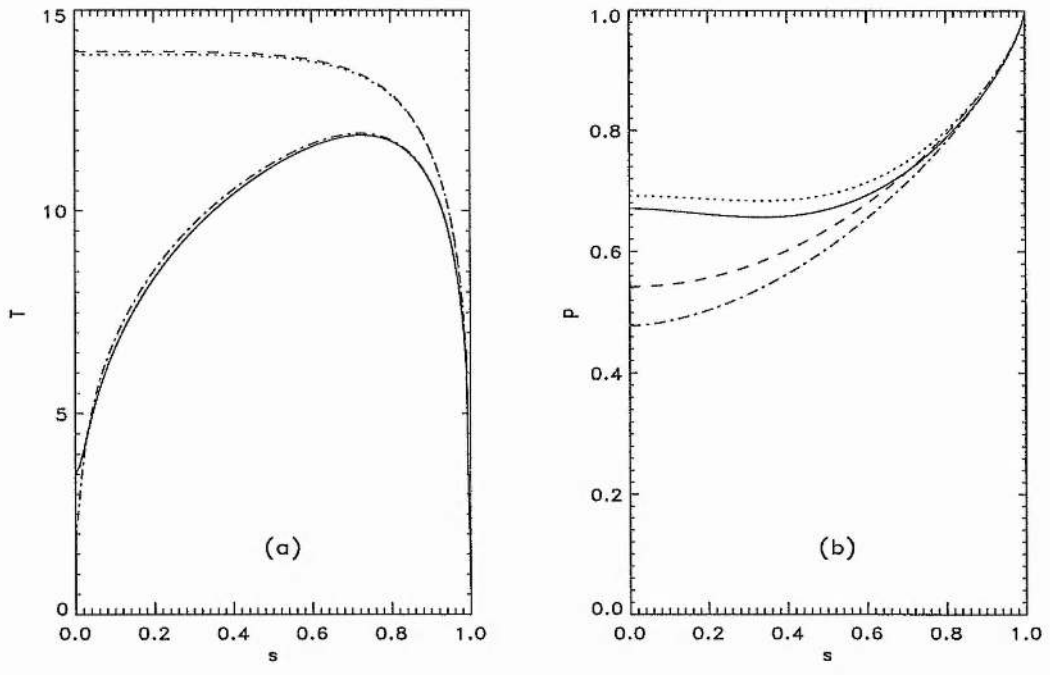

Figure 5.8: Temperature and pressure profiles when the base temperature is taken at chromospheric values. Solid and dotted lines correspond to the gravity case with a dip. Dashed and dashed-dotted curves no dip case.

The summit temperature as a function of boundary temperature is shown in

Figure 5.7. This figure shows the effect of the dip; if one locates at the turning point then it is shifted to the right when the dip is included. This effect is very interesting because for fixed values of the parameters the effect of the inclusion of the dip is to reduce the existence of thermal equilibrium.

Figure 5.8 shows the temperature and pressure profiles but the temperature and pressure at the base have been taken to be at chromospheric values. As can be seen no major changes can be noted in the trend of the profiles when the base temperature is lowered, (apart from now it is connected to the chromosphere instead of the corona).

The pressure and temperature profiles have been plotted in Figure 5.9 for different values of s_*. In this case only the hot solution for those values of s_* have been drawn. In Figure 5.9a, the temperature profile shows that the summit temperature decreases when s_* decreases, however, for $s_* < 0.147$ thermal equilibrium is no longer found. The temperature also decreases when s_* decreases in Figure 5.9b, but the value of s_* at which there is no thermal equilibrium is at $s_* < 0.16$. As can be seen in this figure, the effect of including a dip is to shift the critical decay length of the heating for the appearance of non-equilibrium to higher values. It is seen from this result that a coronal loop under particular conditions namely, fixed values of L_*, s_* and h_*, could suffer a catastrophic cooling when a dip starts to form.

5.3.3 Hot-Cool Solutions

Gravitational effects were considered by Hood and Anzer (1988) and Steele and Priest (1994). Nonetheless, hot-cool solutions were not found. Steele and Priest (1994) by considering a small value of gravity, found several solutions, but hot-cool solutions were difficult to find and were only possible for unrealistic values of gravity. More recently, van den Oord and Zuccarello (1996) arrived at the same conclusion that for loops in hydrostatic equilibrium a hot-cool solution cannot be found. However, when the heating function has a spatial dependence, as considered in this thesis, cool condensations (hot-cool solutions) can be obtained. First of all, assuming that the typical prominence values are known from observations, then the integration is started from the summit to the footpoint. Secondly, in contrast to Section 3.3.1., the values of the parameters L_* and h_* were fixed, and an iteration of the parameter

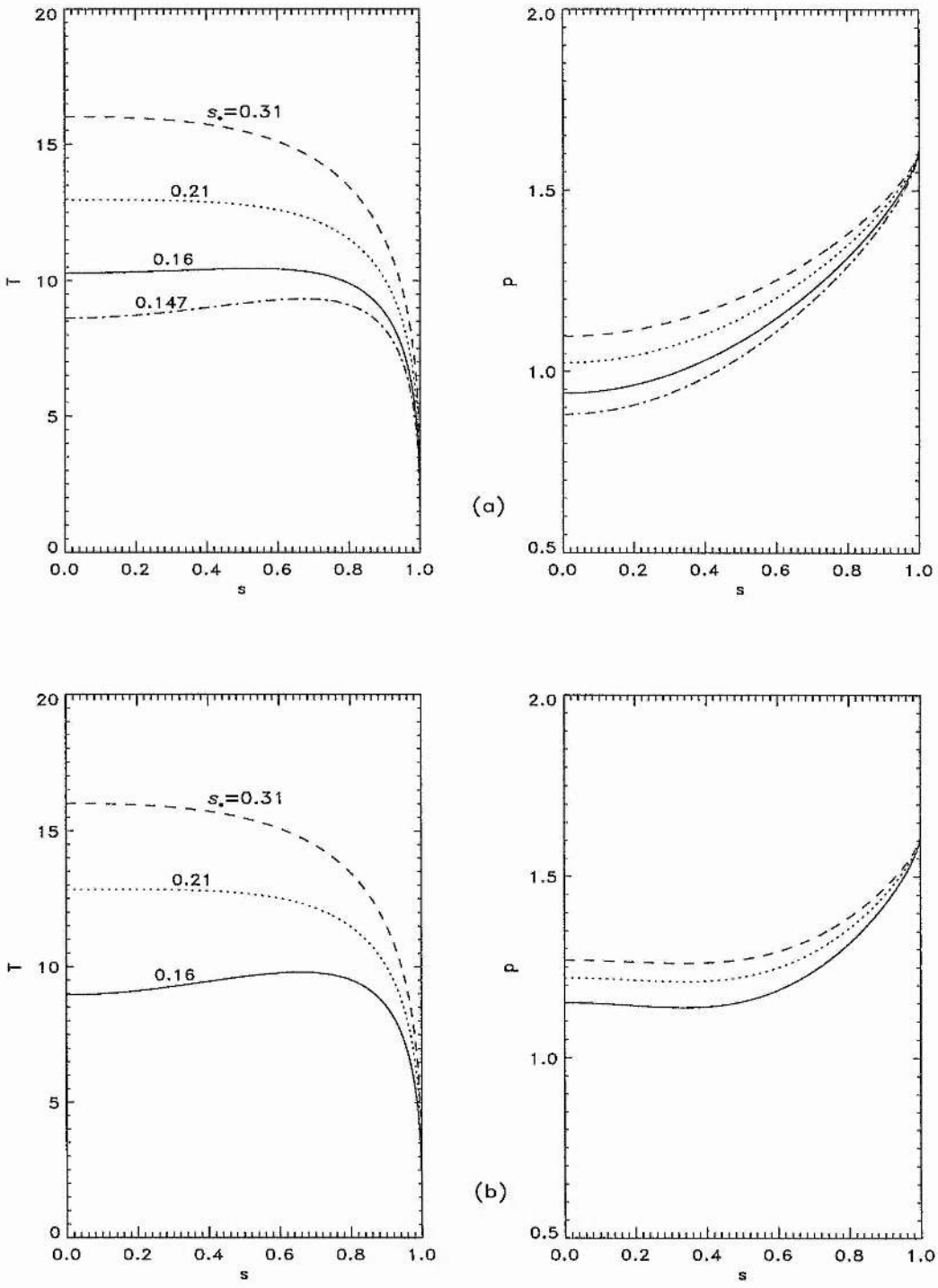

Figure 5.9: Temperature and pressure profiles for different values of the decay length of the heating s_* for a) no dip and b) with a dip.

s_* was performed.

Figure 5.10 is a plot of temperature as a function of s for the values of the parameter L_*, h_* and s_* given in Table 5.1. In this figure, prominence-like solutions are shown where the cool summit is at $T_s = 0.2$ (in units of 10^5K) and a hot coronal part can be seen between the summit and the footpoint. Here the footpoint temperature is at a chromospheric value.

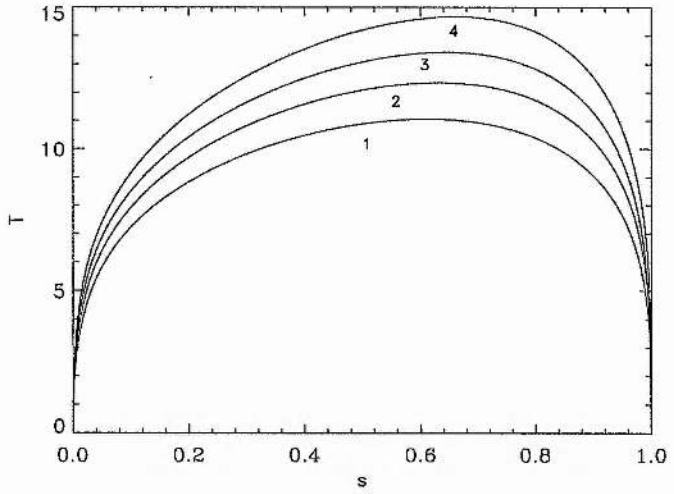

Figure 5.10: The variation of temperature along a loop from the summit at $s = 0$ to the footpoint at $s = 1$. The numbers refer to the listed values given in Table 5.1.

	L_*	s_*	h_*	T_{max}
1	936.01	3.76×10^{-1}	3.96×10^{-2}	11.01
2	1248.01	3.09×10^{-1}	3.96×10^{-2}	12.33
3	1560.01	2.71×10^{-1}	3.96×10^{-2}	13.50
	1872.02	2.44×10^{-1}	3.96×10^{-2}	14.36
4	1968.43	2.37×10^{-1}	3.96×10^{-2}	14.80

Table 5.1: Parameters Obtained For Prominences solution.

In Figure 5.10, the temperature profiles show a maximum of temperature close to $s = 1$ (footpoint) which is shifted to the right when L_* is increased. This shift occurs as a result of the decay length decreasing to satisfy the boundary conditions.

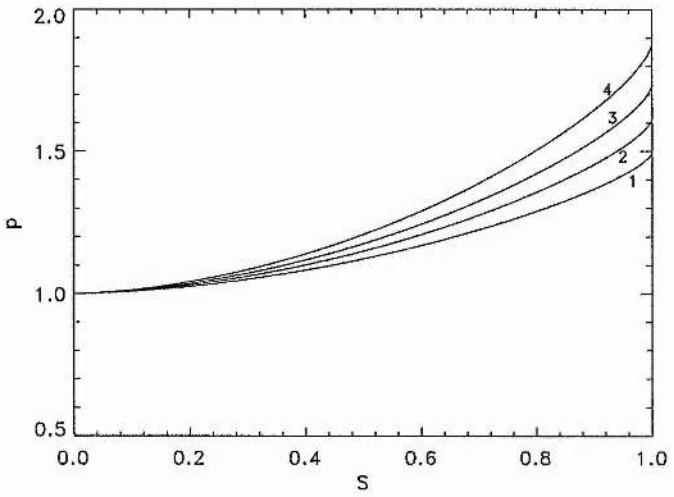

Figure 5.11: The variation of pressure along a loop from the summit at $s = 0$ to the footpoint at $s = 1$. The numbers refer to the listed values given in Table 5.1 .

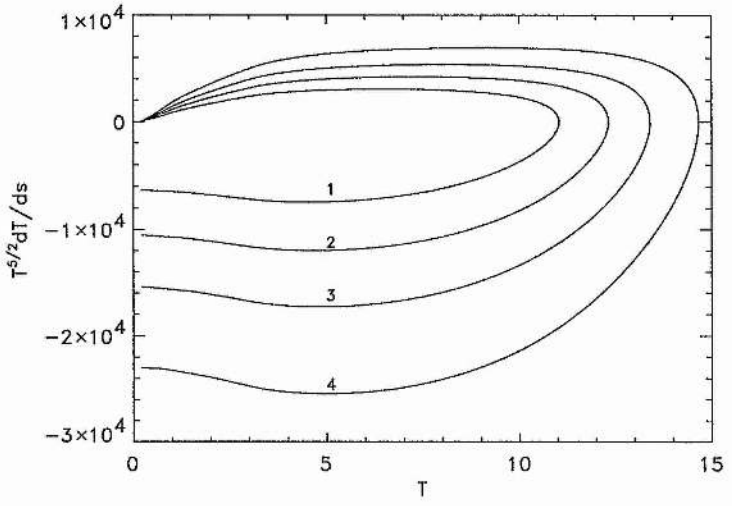

Figure 5.12: The phase plane diagram for the solutions given in Figure 5.10.

Figure 5.11 shows the pressure profiles for the temperatures shown in Figure 5.10. As seen the pressure increases from the summit to the footpoint. The four curves start from $p = 1$ at the summit due to the fact that the integration starts from known prominence pressures and temperatures. Here, one sees that the pressure at the footpoint increases when L_* increases.

In Figure 5.12 $T^{5/2}dT/ds$ is plotted as a function of T. This is the phase plane diagram for the same solutions as in Figure 5.10. The flux increases when L_* increases. Now, it is interesting to note how the contours from the footpoint (which start at non-zero negative value of $T^{5/2}dT/ds$) to the summit where $T^{5/2}dT/ds = 0$ are closed contours. This is the characteristic behaviour of non-autonomous systems.

5.3.4 Energetics Considerations

Figure 5.13 shows the different thermal energy terms for the solution labelled 2 in Figure 5.10.

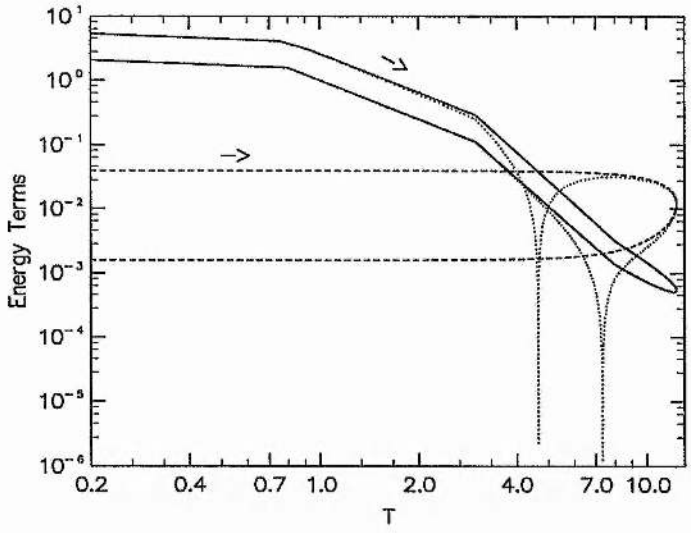

Figure 5.13: Plot of different energy terms as a function of temperature for hot-cool loop labelled with number 2 in Figure 5.10. Solid, dashed and dotted lines indicate the radiation losses, heating mechanism and the thermal conduction, respectively.

The absolute value of different energy terms, namely radiation, heating and conduction is drawn as a function of temperature. In this figure it can be seen that the

conduction balances the radiative losses in the low temperature regime whereas the heating becomes dominant at coronal temperature above about $T = 4.0$ (in 10^5K units), as expected.

When one moves along the loop starting from the footpoint (the arrow indicates the direction) to the summit, the radiation balances the heating at $T = 5.0$. After this point, the heating becomes greater than the cooling, and for temperature $5.0 < T < 12.0$, it is now the conduction which balances the heating. The point of maximum temperature is located between the footpoint and the summit. Moving along the loop one can find a point where heating balances the radiation again. The temperature at which the heating and cooling balance is $T = 7.5$. The shift between the two temperatures is due to the heating decreasing with altitude; the pressure also decreases with altitude when gravity is included. Below $T = 7.0$ the radiation becomes comparable to the conduction.

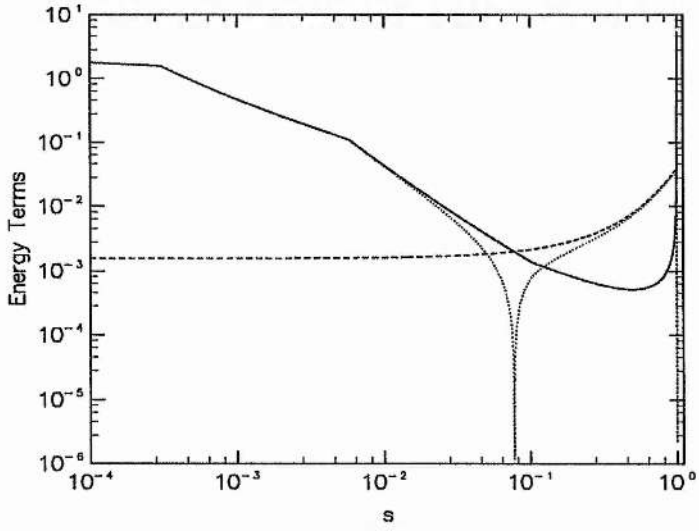

Figure 5.14: Plot of different energy terms as a function of s for a hot-cool loop labelled 2 in Figure 5.10.

Figure 5.14 shows the thermal conduction, the heating and cooling function as a function of coordinate s. It is now clear how the energy terms vary along the loop from the summit to the footpoint. When one moves from the summit to the footpoint the radiation is greater than the heating and the conduction balances the radiation up to $s \sim 2 \times 10^{-2}$; greater than this position, the heating dominates and balances the thermal conduction (thermal conduction behaves as a cooling mechanism). At

s very close to the footpoint, the cooling is greater than the heating and again the cooling balances the conduction. Here the thermal conduction behaves as a heating mechanism.

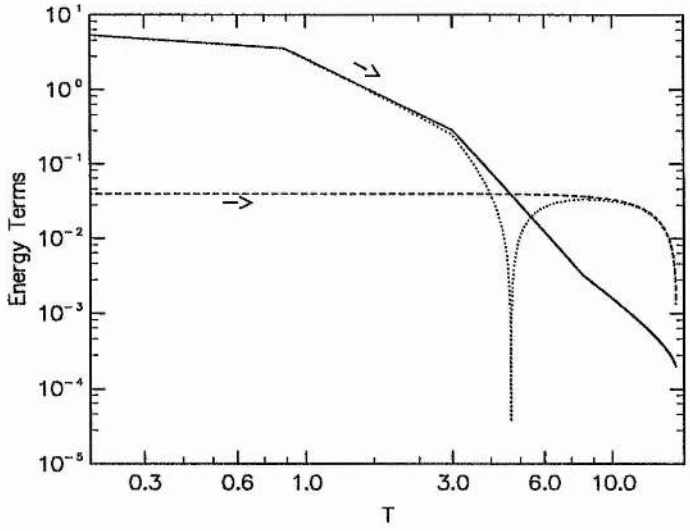

Figure 5.15: Plot of different energy terms as a function of temperature for the hot loop in Figure 5.9a with $s_* = 0.31$.

In Figure 5.15 the corresponding energy terms for a hot loop have been plotted. In contrast to Figure 5.13 the thermal conduction balances the heating at the loop summit. This hot solution corresponds to the solution showed in Figure 5.9a for $s_* = 0.31$.

It is also interesting to show the energetics for a solution close or equal to the critical value of the decay length of the heating. If one plots the corresponding energetic for the solution at $s_* = 0.147$ in Figure 5.9a, then the different energy terms as a function of temperature for this case are shown in Figure 5.16. The energy terms as a function of the position s are also plotted in Figure 5.17. Close to the summit all the energy terms are of the same order. However, due to the fact that the heating decreases with altitude the conduction balances the radiation at the loop summit. Whether the value of s_* is decreased, the thermal conduction no longer balances the radiation then no hot solution is found. Therefore, it is expected that the temperature will decrease and fall down to a new cool equilibrium in a manner similar to that described in Chapter 4.

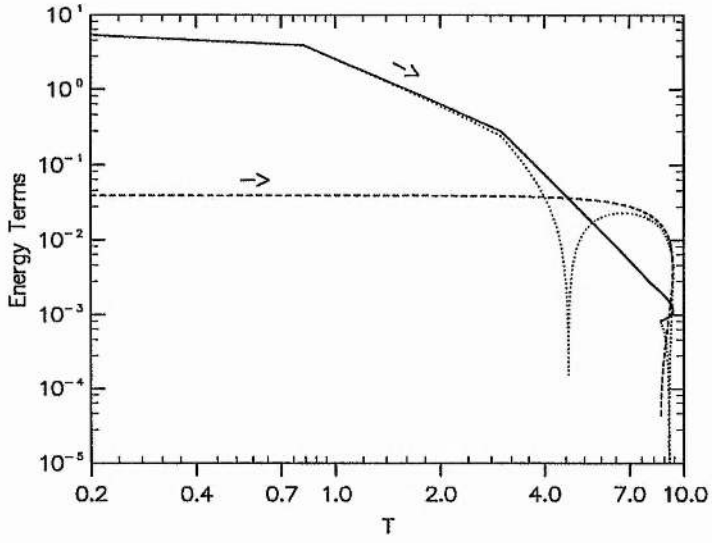

Figure 5.16: Plot of different energy terms as a function of temperature for a hot loop at critical $s_* = 0.147$ in Figure 5.9a .

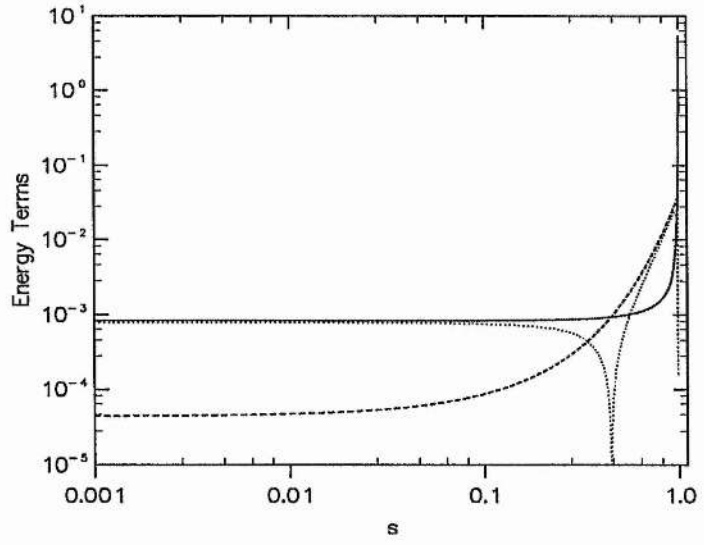

Figure 5.17: Plot of different energy terms as a function of s for a hot loop at a critical $s_* = 0.147$ in Figure 5.9a.

5.4 Summary of the Chapter

The present chapter has modelled a coronal loop by a single field line, along which the plasma is in both thermal and hydrostatic equilibria.

Again for a given values of the parameters L_*, h_* and s_*, multiple solutions were found.

Gravity in the hydrostatic equation was considered to have two parts, (i) one part assuming that the loop has a semicircular shape and (ii) the other part simulating a distortion of the loop summit due to a dip in the magnetic field.

When the dip was neglected, Figures 5.2 and 5.3 showed that the effect of gravity is to raise the summit temperature for a hot loop above of the value for uniform pressure case but reduce the summit temperature for the warm solution.

Furthermore, as seen in Figure 5.2, gravity allows one to find thermal equilibrium solutions for lower values of s_* as compared with the constant pressure case.

The numerical results for the variation of the thermal equilibrium with the base heating and the decay length of heating are also presented in Figures 5.4 and 5.5. They show that not much changes are presented in the general features of the thermal equilibrium when gravity is included.

In Section 5.3.2 the effect of a dip was studied. It was found that the pressure first decays and then increases along the loop starting from the footpoint. The effect of a dip is to increase the summit pressure, which increases the radiation (the heating does not change) and so reduces the summit temperature below the value for gravity without a dip.

It was observed, that the lack of equilibrium (Hood and Priest, 1979; Roberts and Rosenthal, 1980) can occur when decay length of the heating is decreased. However, the critical value of s_* is higher when the dip is considered.

In contrast with other authors (e.g. Steele and Priest 1994), prominence-like solutions were found in this study. The difference between their work with the present study is in the form of the heating function. The heating function considered here has a spatial dependence. The inclusion of gravity as can be seen by using a phase diagram (Hood and Anzer, 1988; Steele and Priest, 1994) produces a open contour when a heating does not have a spatial dependence, but when it is considered with

spatial variation in which it decays along the loop from the summit produces a closed contour as it was shown in Figures 3.2 and 5.12.

The energetics of the thermal equilibrium was also investigated. It gives more information about the different processes inside the loop. One of the interesting result is that for a critical value of s_* (as shown in Figure 5.16) the thermal conduction balances the radiation losses but it is likely that if s_* is decreased further then the radiation dominates the other mechanisms and the catastrophic cooling occurs. In conclusion, this chapter has therefore, shown that hot and hot-cool loop (prominence-like solution) are possible in hydrostatic equilibrium when heating function is considered to decay with altitude.

Chapter 6

Summary and Future Work

6.1 Thesis Summary

The present thesis has attempted to study several aspects of equilibrium and evolution of thermal structure in the solar corona under the assumption that the coronal heating has a spatial dependence.

Chapter 1 has described various solar phenomena both on and close to the solar surface. In particular, about observations of coronal loops and prominences.

Chapter 2 has outlined the MHD equations and described the energy mechanism involved in the present thesis namely, radiation losses, thermal conduction and the heating mechanism. In particular, the spatial dependence of the heating was discussed and the basic equations were reduced to a one-dimensional case.

The thermal equilibrium of coronal loops at constant pressure was examined in Chapter 3. First of all, the behaviour was investigated by using a phase diagram technique showing that for a spatially dependent heating function, the phase plane represents a non-autonomous system. Secondly, the static solution were studied by solving the energy balance numerically in order to find how the temperature varies along a magnetic field line.

The thermal equilibria now depend on a new dimensionless parameter due to the fact that the heating function had an exponential dependence. This new parameter, i.e. the decay length of the heating, was demonstrated to be very important for the onset of thermal non-equilibrium. If the heating decay length was decreased down

below a critical value (it depends on on the values of other parameters) then there are no hot loops. It was shown that multiple solutions exist and hot-cool loop or prominences-like solutions were found.

A simplified cooling function was introduced which had all the same properties as the full cooling function. This allowed one to demonstrate the existence of a lower solution branch. This branch was missed in the $T_s(T_b)$ graphs when a more accurate cooling function was used because of numerical difficulties.

The stability of these static solutions to the energy equation was also investigated up to a second order approximation and it was concluded that the linear approximation predicts that the instability depends on the size of the structure, but the second order approximation predicts that the stability or instability, additionally depends not only on the size of the structure but also on whether the disturbance decreases or increases the initial temperature.

Chapter 4 was concerned with simulating the thermal evolution of coronal structures with a view to simulating the formation of prominence. Due to the fact that the heating function had a spatial dependence of the form $\sim \exp(-s/s_*)$, it was found that hot or cool summits were reached depending on whether the decay length of the heating, s_*, was greater or smaller than a critical value. From this, it was shown how the loops evolve from a hot plasma to a cool condensation. It was also found that, after the condensation had formed, these cool solutions were remarkable stable.

Furthermore, it was demonstrated that the coronal evolution depended on the initial conditions. Hence, a threshold value was found on either side of which the loop evolved to different solutions.

The evolution of a trivial solution to a non-uniform solution was investigated. This numerical study agreed with the analytical results obtained in the second order stability analysis derived in Chapter 3.

In Chapter 5 hydrostatic thermal equilibrium was investigated by including the effect of gravity. Most of the results obtained in Chapter 3 were reproduced with the added feature that there is no hot solution when heating decay length was smaller than a critical value. The inclusion of gravity helped to find solutions where for constant-pressure loop did not exist.

The gravity was considered to have two parts due to , (i) the assumption that the loop has a basic semicircular shape and (ii) a distortion of the loop summit simulating a dip in the magnetic field.

When the dip was included the pressure first decays and then increases along the loop starting from the footpoint. The effect of a dip was to increase the summit pressure, which increases the radiation (the heating does not change) and so reduces the summit temperature below the value for gravity without a dip.

One of the most important result in this chapter was that prominence-like solutions were found when the effect of gravity is considered. Other authors have found it difficult to get this kind of solution. The main difference between their work and this thesis was in the form of the heating function considered. Here we assumed a spatially dependent heating function.

6.2 Future Work

There are several possibilities for extending this work and these are discussed now.

As mentioned, in throughout the thesis it is assumed that the loops concerned are of constant cross-sectional area (and hence constant magnetic field along the loop). Therefore, further work would include the area variation. It would modify the equation of thermal equilibrium (3.13) as

$$\frac{1}{\tilde{A}(s)}\frac{d}{ds}\left(\tilde{A}(s)T^{5/2}\frac{dT}{ds}\right) = L_*^2\left[p^2\chi T^{\alpha-2} - h_* \exp\left(-\frac{s}{s_*}\right)\right], \tag{6.1}$$

being

$$\tilde{A}(s) = \frac{A(s)}{A_0} = \left[1 + (k-1)\sin^2\left(\frac{\pi}{2}s\right)\right], \tag{6.2}$$

where A_0 is the base cross-sectional area and s is the distance along the loop from the footpoint to the summit. A value of $k = 1$ indicates a constant area loop, for $k > 1$ the summit is wider than the footpoint while $k < 1$, the footpoint is wider than the summit.

This thesis has also considered a spatial dependence of the heating, with the heating form symmetric in each leg of the loop. Hence, another extension would be to consider asymmetric heating because it is unlikely that identical heating on

both legs of the loop will occur. Asymmetric heating function in loops has been considered by Klimchuk and Mariska (1988) and Antiochos and Klimchuk (1991) to model flows in solar loops and prominences formation respectively.

A simple test initially would be to assume the heating with an exponential decay along the loop from one footpoint to another footpoint. Figure 6.1 shows the result of hot loops for different values of the decay length of the heating. The heating decreases from the left footpoint to the right footpoint. As seen in this figure there is a maximum in temperature in the left side which shifts to the right up to the midpoint when s_* is increased.

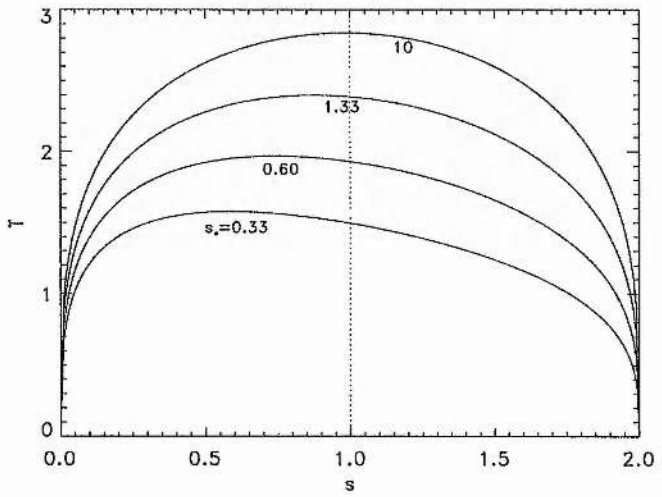

Figure 6.1: The variation of temperature along a loop from the footpoint at $s = 0$ to the footpoint at $s = 2$. The vertical dotted line indicates the loop midpoint.

Different forms of the heating function can be taken, for instance, considering the left footpoint has a dependence $\sim \exp(-s/s_{*l})$ and the right footpoint $\sim \exp(-(s/s_{*r})^3)$, s_{*l} and s_{*r} are the heating decay length for the left and right legs of the loop respectively. This could occur if the field and plasma in the left leg is more uniform than the right leg.

In Figure 6.2 the temperature as a function of s is shown under the above assumption. Asymmetric temperature profiles are shown. The maximum temperature is located either to the left side or the right side corresponding to the leg which has a larger energy input. The parameters in the heating function considered are : same

base heating h_* on both left for the three curves and the decay length of the heating $s_{*l} = 0.6$ and $s_{*r} = 0.33$ for the solid curve, $s_{*l} = s_{*r} = 0.6$ for the dashed curve and $s_{*l} = 0.33$ and $s_{*r} = 0.6$ for the dot-dashed curve.

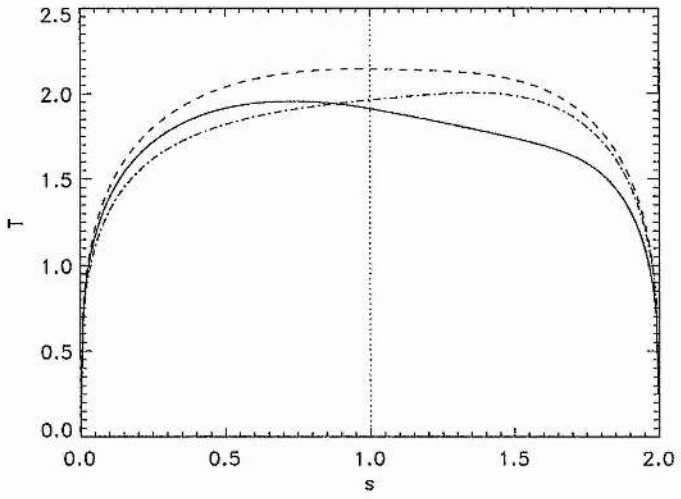

Figure 6.2: The variation of temperature along a loop from the footpoint at $s = 0$ to the footpoint at $s = 2$, for three different combinations of s_{*l} and s_{*r}. The vertical dotted line indicates the loop midpoint.

For a hot-cool loop it is expected that the condensation does not occur at the midpoint, but in the leg with the weaker heating. Further work needs to be done in order to obtain these loops and test their stability.

Further work in Chapter 4 would be to extend the values of the temperature at the boundary down to chromospheric values. It is not expected that there will be many changes when the boundary temperature is reduced. The only change that one expects is in the value of s_* at which condensation will occur as can be seen in the Figure 3.6 when the boundary temperature is moved to lower T_b.

With the model employed in Chapter 4 it would be interesting to study the effect of increasing the heat input when a condensation has form. Poland and Mariska (1986) have shown that a sufficient increase in the heating to a loop with a cool summit causes its temperature to rise up to a hot summit value. Démoulin and Vial (1992) have identified this process as a possible mechanism for the thermal disappearance of prominences. We have been able to produce a similar result as Poland and Mariska (1986) with our model as shown in Figure 6.3. This figure

shows the evolution of the summit temperature. The simulation has been started with the initial profile studied in Section 4.4. The plasma cools down and reaches chromospheric values. Then, the heating is increased linearly with time and suddenly the temperature increases up to coronal values.

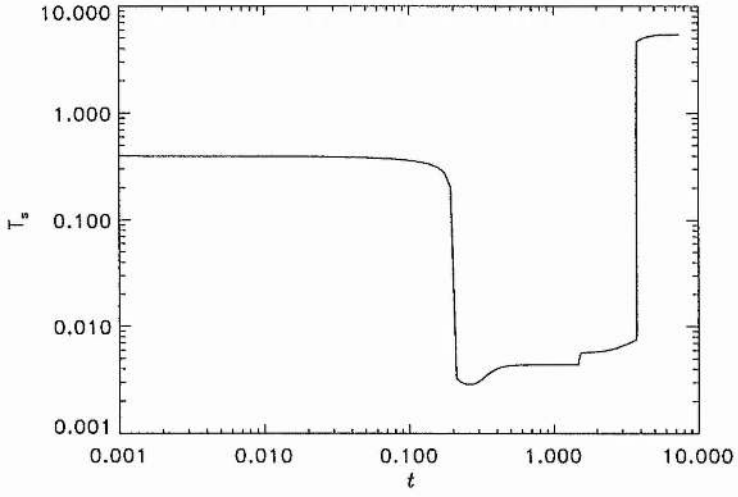

Figure 6.3: The temperature (in units of 2×10^6K) at the loop summit as a function of time.

Hood and Priest (1981) proposed a thermal non-equilibrium as a mechanism to heat up cool plasma to temperatures in excess of 10^6K. We believe that further study in this subject could help to understand the thermal disappearance of prominences.

All the developments mentioned for Chapter 3 can be carried out for Chapter 5.

Figure 6.4 shows a preliminary results when the area variation is included as well as gravity and the heating function employed in this thesis. It is a plot of the summit temperature as a function of L_* when s_* and h_* are keeping fix, for different values of the parameter k in the equation (6.2). The base temperature has been taken at a chromospheric value. As is seen, for a chosen value of L_*, the summit temperature increases with k (hence, T_s increases when the area increases). It is also found that there are more thermal equilibrium solutions at higher values of L_* when k is increased. Further investigations are required to understand the effects of the area variation on the thermal equilibrium of coronal loops.

Moreover, it would be an interesting study to consider different heating functions. So far, some difference appear in hot loops when a particular form of the heating

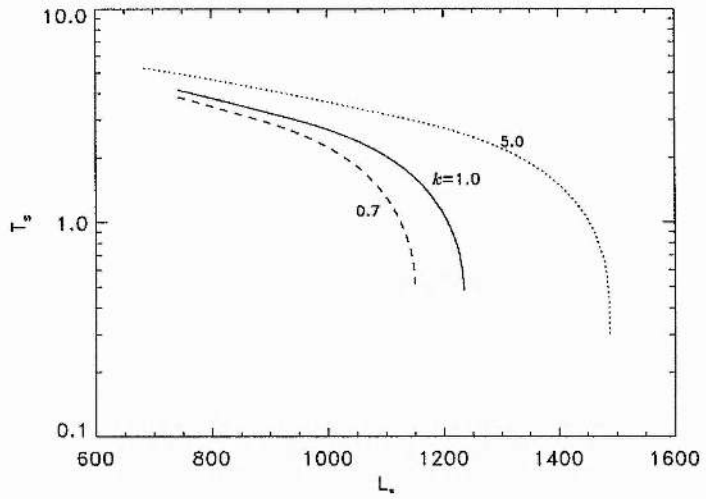

Figure 6.4: The summit temperature (in units of 10^5K) as a function of the parameter L_*, for different values of the area variation.

is considered. If heating is proportional to the density then gravity reduces the temperature of such loops (Steele and Priest, 1994). However, when the heating is constant gravity increases the temperature in such loops (Wragg and Priest, 1981b). In Chapter 5, an increase in the temperature in hot loop was also found.

Another extension in Chapter 5 would be to consider the effect of steady flows for the heating assumed in this thesis. Cargill and Priest (1982) have already studied the effect of flows when the heating function is constant and proportional to the density. However, it would be interesting how these results would change if a spatially dependent heating is assumed.

Finally, the most ambitious extension of this thesis is to solve the full set of reduce equations in one dimension discussed in Section 3.2 in which gravity is included. This thesis has already investigated with simple models, the basic processes in order to understand the behaviour of such a more complicated system.

Appendix A

A.1 Derivation of the Dispersion Relation (2.29)

Consider the field-aligned propagation of an small velocity perturbation $\mathbf{v}(z,t) = (v_x(z,t), 0, 0)$ in an uniform medium with constant density ρ_0 and uniform magnetic field $\mathbf{B_0} = (0, 0, B_0)$ and a corresponding magnetic field perturbation $\mathbf{b} = \mathbf{b}(z,t)$. Note that incompressible perturbation for which $\nabla \cdot \mathbf{v} = 0$ have been considered. The solenoidal condition of magnetic field also yields $\nabla \cdot \mathbf{b} = 0$.

The governing linearised equations in this case are the momentum equation with the inclusion of viscosity, and induction equation, viz.

$$\rho_0 \frac{\partial \mathbf{v}}{\partial t} = (\nabla \times \mathbf{b}) \times \frac{\mathbf{B_0}}{\mu} + \rho_0 \nu \nabla^2 \mathbf{v}, \tag{A.1}$$

$$\frac{\partial \mathbf{b}}{\partial t} = \nabla \times (\mathbf{v} \times \mathbf{B_0}). \tag{A.2}$$

Differentiating (A.1) with respect to time yields

$$\rho_0 \frac{\partial^2 \mathbf{v}}{\partial t^2} = \left(\nabla \times \frac{\partial \mathbf{b}}{\partial t} \right) \times \frac{\mathbf{B_0}}{\mu} + \rho_0 \nu \nabla^2 \frac{\partial \mathbf{v}}{\partial t}. \tag{A.3}$$

Combining Equations (A.2) and (A.3) gives

$$\rho_0 \frac{\partial^2 \mathbf{v}}{\partial t^2} = \nabla \times [\nabla \times (\mathbf{v} \times \mathbf{B_0})] \times \frac{\mathbf{B_0}}{\mu} + \rho_0 \nu \nabla^2 \frac{\partial \mathbf{v}}{\partial t}. \tag{A.4}$$

We now consider a single Fourier component

$$v_x(z,t) = \hat{v}_x \exp\left[i(k_z z - \omega t)\right], \tag{A.5}$$

$\hat{v}_x$ being the velocity amplitude.

Equation (A.4) then takes the following form

$$-\rho_0\omega^2\hat{v}_x = -k_z^2\frac{B_0^2}{\mu}\hat{v}_x + i\rho_0\nu\omega k_z^2\hat{v}_x, \tag{A.6}$$

which immediately gives the dispersion relation (see Equation (2.29) in Chapter 2 with z replaced by s)

$$k_z^2 v_A^2 - \omega^2 = i\omega\nu k_z^2. \tag{A.7}$$

Solving for k_z^2 one gets

$$k_z^2 = \frac{\omega^2}{v_A^2}\frac{1}{\left(1-\frac{i\omega\nu}{v_A^2}\right)}, \tag{A.8}$$

and k_z as

$$k_z = \frac{\omega}{v_A}\left(1-\frac{i\omega\nu}{v_A^2}\right)^{-1/2}. \tag{A.9}$$

For $\omega\nu/v_A^2 \ll 1$, retaining only the leading term in a binomial expansion one obtains

$$k_z = \frac{\omega}{v_A}\left(1+\frac{1}{2}\frac{i\omega\nu}{v_A^2}\right). \tag{A.10}$$

Substitution of (A.10) in (A.5) then readily gives

$$v_x = \hat{v}_x \exp\left(-\frac{1}{2}\frac{\omega^2\nu}{v_A^3}z\right)\exp\left[i(\frac{\omega}{v_A}z-\omega t)\right]. \tag{A.11}$$

With this result the mechanical energy flux can the be written as

$$\frac{1}{2}\rho_0 v_x^2 v_A \approx \frac{1}{2}\rho_0 v_A \exp\left(-\frac{\omega^2\nu}{v_A^3}z\right), \tag{A.12}$$

and so the dependence of the heating would be

$$H = h_0 \exp\left(-\frac{z}{z_H}\right), \tag{A.13}$$

with $z_H = v_A^3/\omega^2\nu$.

In this simple example we obtain an exponential variation of energy dissipation with distance, and hence a heating rate, as is given in our phenomenological model in Equation (2.28) of Chapter 2.

Appendix B

B.1 The Phase Plane

The equation (3.7) can be written as system of coupled nonlinear ordinary differential equations as

$$\frac{dT}{ds} = VT^{-5/2}, \tag{B.1}$$

$$\frac{dV}{ds} = L_*^2 \left[p^2 \chi T^{\alpha-2} - h\right], \tag{B.2}$$

where $V = T^{5/2} dT/ds$.

When h is a function of the loop coordinate s the system is called non-autonomous because the right-hand side depends explicitly on s, hence one has to proceed numerically. Assuming that h is independent of s the system becomes autonomous. The essential ingredients of the phase plane are the critical points, that is those values of T and V for which $dT/ds = dV/ds = 0$.

Hence, the critical points are

$$V = 0, \qquad \text{and} \qquad T = \left[\frac{h_*}{p^2\chi}\right]^{\frac{1}{\alpha-2}} = T_{crit}.$$

Linearising the equations (B.1) and (B.2) around the critical point by setting

$$\tau = T - T_{crit}$$

(B.1) and (B.2) become,

$$\frac{d\tau}{ds} = VT_{crit}^{-5/2} \tag{B.3}$$

$$\frac{dV}{ds} = L_*^2 \chi T_{crit}^{\alpha-3}(\alpha - 2)\tau \tag{B.4}$$

If the solution for V and τ are of the form $e^{\lambda s}$ then

$$\lambda^2 = L_*^2 \chi T_{crit}^{\alpha - 11/2}(\alpha - 2)$$

Thus, if $\alpha < 2$ then $T_{crit} = T_h$ is a centre point, but if $\alpha > 2$, then $T_{crit} = T_c$ is the saddle point (Drazin, 1992). In fact, for the autonomous system it is possible to construct a first integral by dividing (B.1) and (B.2) and integrating dV/dT. The first integral gives the phase space trajectories shown in Figure 3.2.

Appendix C

C.1 Derivation of the Non-Linear Approximation

Equation (3.20) can be expressed as

$$\frac{\partial T}{\partial t} = T\left\{\frac{\partial}{\partial s}\left(T^k \frac{\partial T}{\partial s}\right) - g(T)\right\} \tag{C.1}$$

where $g(T) = L_*^2(\chi T^m - H)$, $k = 5/2$ and $m = \alpha - 2$.

In addition, one assumes that the function $g(T)$ can be represented near $\overline{T}(s)$ by a Taylor's series, i.e.

$$g(\overline{T} + \delta T) = g_o(\overline{T}) + g_1(\overline{T})(\delta T) + \frac{1}{2!}g_2(\overline{T})(\delta T)^2 + \frac{1}{3!}g_3(\overline{T})(\delta T)^3 + ...; \tag{C.2}$$

where

$$g_o(\overline{T}) = L_*^2(\overline{T}^m - H), \tag{C.3}$$

$$g_1(\overline{T}) \equiv \left(\frac{dg}{dT}\right)_{\overline{T}} = L_*^2\, m\overline{T}^{m-1}, \tag{C.4}$$

$$g_2(\overline{T}) \equiv \left(\frac{d^2g}{dT^2}\right)_{\overline{T}} = L_*^2\, m(m-1)\overline{T}^{m-2}, \tag{C.5}$$

$$g_3(\overline{T}) \equiv \left(\frac{d^3g}{dT^3}\right)_{\overline{T}} = L_*^2\, m(m-1)(m-2)\overline{T}^{m-3} \tag{C.6}$$

Substituting (3.21) - (3.23) and (C.2) - (C.6) into equation (C.1) and equating terms of the same order in A, one obtains for:

The zero order in A

$$0 = g_o(\overline{T}) + \frac{\partial}{\partial s}\left(\overline{T}^k \frac{\partial \overline{T}}{\partial s}\right) \tag{C.7}$$

the first order in A

$$a_1 f_1(s) = \overline{T}\left[g_1(\overline{T}) f_1(s) + \frac{\partial}{\partial s}\left(\frac{\partial \overline{T}^k}{\partial s} f_1\right) + \frac{\partial}{\partial s}\left(\overline{T}^k \frac{\partial f_1}{\partial s}\right)\right] \tag{C.8}$$

the second order in A

$$\begin{aligned} a_2 f_1(s) + 2a_1 f_2(s) &= \overline{T}(g_1 f_2 + \frac{1}{2} g_2 f_1^2) + f_1^2 g_1 \\ &+ f_1\left[\frac{\partial}{\partial s}\left(T^k \frac{\partial f_1}{\partial s} + f_1 \frac{\partial \overline{T}^k}{\partial s}\right) + f_1 g_1\right] \\ &+ \overline{T}\frac{\partial}{\partial s}\left[\overline{T}^k \frac{\partial f_2}{\partial s} + f_1 k \overline{T}^{k-1} \frac{\partial f_1}{\partial s}\right. \\ &+ \left.(f_2 k \overline{T}^{k-1} + \frac{1}{2} f_1^2 k(k-1)\overline{T}^{k-2}) \frac{\partial \overline{T}}{\partial s}\right] \end{aligned} \tag{C.9}$$

and so on.

Then rearranging (C.8) and (C.9) for the trivial solution $\overline{T} = T_e$, one gets the equations (3.27) and (3.37) respectively.

Appendix D

D.1 Numerical Algorithm for the Simulation of Thermal Evolution

The purpose of this appendix is to describe briefly the numerical scheme used in solving the equations

$$\frac{\partial v}{\partial s} = \frac{\partial}{\partial s}\left(T^{5/2}\frac{\partial T}{\partial s}\right) - L_*^2\left[\chi T^{\alpha-2} - h\right], \tag{D.1}$$

$$\frac{\partial T}{\partial t} = -v\frac{\partial T}{\partial s} + T\frac{\partial v}{\partial s}, \tag{D.2}$$

subject to the boundary condition (4.9) and initial conditions (4.10).

The equations are solved using finite difference method where the size of the grid is defined by h and timestep is defined by k.

The method uses the temperature profiles to evaluate the velocity through the equation (D.1). The equation (D.2) is then employed to calculate the temperature at the next time-step.

The notation for the variables $T(s,t)$ and $v(s,t)$ are

$$\begin{aligned} T_i^j &= T(ih, jk) \\ v_i^j &= v(ih, jk) \end{aligned} \tag{D.3}$$

with h and k being the grid size for space and time respectively.

The method uses the two step sequence where the velocity is estimated at half a step by

$$v_{i+1}^{j} = v_i^j + h\left[\frac{1}{2}(f_i^j + f_{i+1}^j)\right] \tag{D.4}$$

where

$$f_i = 2/7\frac{T_{i+1}^{7/2} - 2T_i^{7/2} + T_{i-1}^{7/2}}{h^2} - L_*^2(\chi T_i^{\alpha-2} - h_i) \tag{D.5}$$

The temperature at half time-step is calculated from

$$T_i^{j+1/2} = T_i^j + k/2\left[T_i^j f_i^j - v_i^j\frac{T_{i+j}^j - T_{i-1}^j}{2h}\right] \tag{D.6}$$

and the full step is obtained from

$$T_i^{j+1} = T_i^j + k\left[T_i^{j+1/2} f_i^{j+1/2} - v_i^{j+1/2}\frac{T_{i+1}^{j+1/2} - T_{i-1}^{j+1/2}}{2h}\right] \tag{D.7}$$

The constraints for the time-step are from the conduction

$$\frac{k}{h^2} < \frac{1}{2T^{7/2}}$$

and the CFL conduction

$$\frac{k}{h} < \frac{1}{v}$$

with the value of k taken is smaller of the minimum of the two values.

Bibliography

[1] An, C. H.: 1985, *Astrophys. J.* **298**, 409.

[2] An, C. H.: 1986, *Astrophys. J.* **304**, 532.

[3] An, C. H., Bao J. J. and Wu, S. T.: 1988, *Solar Phys.* **115**, 81.

[4] Antiochos, S. K. and Klimchuk, J. A.: 1991, *Astrophys. J.* **378**, 372.

[5] Antiochos, S. K. and Noci, G.: 1986, *Astrophys. J.* **301**,440.

[6] Babcock, H. W. and Babcock, H. D.: 1955, *Astrophys. J.* **121**, 349.

[7] Ballester, J. L.: 1994, *Proc. of the Third SOHO Workshop - Solar Dynamic Phenomena and Solar Wind Consequences*, p 13.

[8] Braginskii, S. I.: 1965, *Rev. Plasma Phys.* **1**, 205.

[9] Browning, P. K.: 1991, *Plasma Phys. and Controlled Fusion* **33**, 321.

[10] Bray, R. J. Cram, L.E. Durrant, C. J. and Loughhead, R.E.: 1991, *Plasma Loops in the Solar Corona*, Cambridge University Press.

[11] Bray, R. J. and Loughhead, R.E.: 1964, *Sunspots*, Chapman and Hall, London.

[12] Cargill, P. J. and Priest, E. R.: 1982, *Geophys. Astrophys. Fluid Dynamics* **20**, 227.

[13] Chiuderi, C. and Van Hoven, G.: 1979, *Astrophys. J.* **232**, L69.

[14] Choe, G. S. and Lee, L. C.: 1992, *Solar Phys.* **138**, 291.

[15] Collier-Cameron, A.: 1988, *Monthly Not. Roy. Astron. Soc.* **233**, 235.

[16] Cox, D. P. and Tucker, W. H.: 1969, *Astrophys. J.* **157**, 1157.

[17] Craig, I. L., McClymount, A. N. and Underwood, J. H.: 1978, *Astron. Astrophys.* **70**, 1.

[18] Démoulin, P.: 1993, *Adv. Space Res.* **13**(9), 95.

[19] Démoulin, P. and Vial, J.C.: 1992, *Solar Phys.* **141**, 289.

[20] Démoulin, P., Raadu, M. A., Malherbe, J. M. and Schmieder, B.: 1987, *Astron. Astrophys.* **183**, 142.

[21] Dere, K. P., Bartoe, J-D. F., Brueckner, G. E.: 1986, *Astrophys. J.* **310**, 456.

[22] de Jager, C.: 1959, *Handbuch der Physik.* **52**, 80.

[23] Drazin, P.G.: 1992, *Nonlinear Systems*, Cambridge University Press

[24] Drazin, P. G. and Reid, J.: 1981, *Hydrodynamic Stability*, Cambridge University Press, Cambridge.

[25] Dunn, R. B.: 1960, Ph.D. Thesis, Harvard University.

[26] Engvold, O.: 1976, *Solar Phys.* **49**, 283.

[27] Engvold, O., Hirayama, T., Leroy, J-L., Priest, E. R. and Tandberg-Hanssen, E.: 1990, in *Dynamics of Quiescent Prominence*, IAU Colloq. No.117 (Ed. V. Ruzdjak and E. Tandberg-Hanssen),p.294, Lecture Notes in Phys. **363** (Springer-Verlag).

[28] Field, G. B.: 1965, *Astrophys.* **142**, 531.

[29] Forbes, T. G.: 1986, in *Coronal and Prominences Plasmas* (Ed. A. I. Poland), NASA Conf. Publ. 2442, p. 21.

[30] Heyvaerts, J. and Priest, E. R.: 1983, *Astron. Astrophys.* **117**, 220.

[31] Hildner, E.: 1974, *Solar Phys.* **35**, 123.

[32] Hirayama, T.: 1985, *Solar Phys.* **100**, 415.

[33] Hirayama, T.: 1986, *Coronal and Prominence Plasmas*, NASA conference Publication 2442 (Ed. A. Poland), p.149.

[34] Hollweg, J. V.: 1990, *Computer Phys. Reports*, **12**, 205.

[35] Hood, A.W. and Anzer, V.: 1988, *Solar Phys.* **115**, 61.

[36] Hood, A.W., Ireland, J. and Priest, E. R.: 1996, *Submitted.*

[37] Hood, A.W. and Priest, E. R.: 1979, *Astron. Astrophys.* **77**, 233.

[38] Hood, A.W. and Priest, E. R.: 1981, *Solar Phys.* **73**, 289.

[39] Ibañez S., M. H., Parravano, A. and Mendoza B., C. A.: 1992, *Astrophys. J.* **398**, 177.

[40] Ibañez S., M. H., Parravano, A. and Mendoza B., C. A.: 1993, *Astrophys. J.* **407**, 611.

[41] Ibañez S., M. H. and Rosenzweig, P.: 1995, *Phys. Plasmas* **2**, 4127.

[42] Ireland, R. C., Van der Linden, R. A. M., Hood, A. W. and Goossens, M.: 1992, *Solar Phys.* **142**, 265.

[43] Kawaguchi, I.: 1967, *Solar Phys.* **1**, 420.

[44] Kim, I. S.: 1990, in Ruzdjak, V. and Tandberg-Hanssen, E. (eds), *Dynamics of Quiescent Prominences*, Springer-Verlag, Berlin Heidelberg, Germany.

[45] Kippenhahn, R. and Schlüter, A.: 1957, *Zs. Ap.* **43**, 36.

[46] Klimchuk, J. A. and Porter, L. J.: 1995, *Nature* **377**, 131.

[47] Klimchuk, J. A. Mariska, J. T.: 1988, *Astrophys. J.* **328**, 334.

[48] Kuperus, M.: 1969, *Space Sci. Rev.* **9**, 713.

[49] Kuperus, M. and Raadu, M. A.: 1974, *Astron. Astrophys.* **31**, 189.

[50] Kuperus, M. and Tandberg-Hanssen, E.: 1967, *Solar Phys.* **2**, 39.

[51] Kuperus, M., Ionson, J. A. and Spicer, D. S.: 1981, *Ann. Rev. Astron. Astrophys.* **19**, 7.

[52] Landau, L.: 1944, *C.R. Acad. Sci.* **44**, 311.

[53] Landini, M. and Monsignori Fossi, B. C.: 1975, *Astron. Astrophys.* **42**, 213.

[54] Landini, M. and Monsignori Fossi, B. C.: 1981, *Astron. Astrophys.* **102**, 391.

[55] Leighton, R. B., Noyes, R. W. and Simon, G. W.: 1962, *Astrophys. J.* **135**, 474.

[56] Leroy, J. L.: 1977, *Astron. Astrophys.* **60**, 79.

[57] Leroy, J. L.: 1989, in *Dynamics and Structure of Quiescent Solar Prominences*(Ed. E.R. Priest), pp.77 and 92. Kluwer Academic Publishers: Dordrecht, The Netherlands.

[58] Leroy, J. L., Bommier, V. and Sahal-Brechot, S.: 1983, *Solar Phys.* **83**, 135.

[59] Lites, B. W., Bruner, E. C., Chipman, E. G., Shine, R. A., Rottman, G. J., White, O. R. and Athay, R. G.: 1976, *Ap. J. Lett.* **210**, L111.

[60] Malherbe, J. M.:1989, in *Dynamics and Structure of Quiescent Solar Prominences*(Ed. E.R. Priest), p.115. Kluwer Academic Publishers: Dordrecht, The Netherlands.

[61] Martin, S. F.: 1986, in *Coronal and Prominence Plasmas*, NASA Conf. Pub., 2442, (Ed. A. I. Poland). p.73.

[62] Martin, S. F.: 1990, in Ruzdjak, V. and Tandberg-Hanssen, E. (eds), *Dynamics of Quiescent Prominences*, Springer-Verlag, Berlin Heidelberg, Germany.

[63] McWhirter, R. W. P., Thonemann, P. C. and Wilson, R.: 1975, *Astron. Astrophys.* **40**, 63.

[64] Meerson, B.:1989, *Astrophys. J.* **347**, 1012.

[65] Mein, P. and Mein, N.: 1989, *Astron. Astrophys.* **203**, 162.

[66] Mendoza, C. A. and Hood, A. W.: 1996, *Astrophysical Letters and Communications* **in press.**

[67] Menzel, D. H. and Evans, J. W.: 1953, *Accad. Naz. Lincei. Convegno Volta* **11**, 119.

[68] Michard, R.: 1974, in Athay, R. G. (ed), *Chromospheric Fine Structure*, IAU Symposium No. 56, D. Reidel Publ. Co., Dordrecht, Holland.

[69] Mok, Y., Drake, J. F., Schnack, D. D., and Van Hoven, G.: 1990, *Astrophys. J.* **359**, 288.

[70] Mok, Y. and Einaudi, G.: 1985, *J. Plasma Phys.* **33**, 199.

[71] Mouradian, Z. and Soru-Escaut, I.:1990, *Hvar. Obs. Bull.* **13**, 379.

[72] Mouradian, Z., Martres, M. J. and Soru-Escaut, I.: 1986, in *Coronal and Prominence Plasmas*, NASA Conf. Pub., 2442, (Ed. A. I. Poland).p. 221.

[73] Nakagawa, Y. and Malville, J. M.: 1969, *Solar Phys.* **9**, 102.

[74] Orrall, F. Q. and Zirker, J. B.: 1961, *Astrophys. J.* **134**, 72.

[75] Oran, E. S., Mariska, J.T. and Boris, J. P.: 1982, *Astrophys. J.* **254**, 349.

[76] Parker, E. N.: 1953, *Astrophys. J.* **117**, 431.

[77] Parker, E. N.: 1988, *Astrophys. J.* **330**, 474.

[78] Parker, E. N.: 1989, *Solar Phys.* **121**, 271.

[79] Pettit, E.: 1925, *Publ. Yerkes Obs.* **3(IV)**, 205.

[80] Pikel'ner, S. B.: 1971, *Solar Phys.* **17**, 44.

[81] Plocieniak, S. and Rompolt, B.: 1972, *Solar Phys.* **104**, 303.

[82] Pneuman, G. W. and Orrall, F. Q.: 1986, in Sturrock, P. A., Holzer, T. E., Mihalas, D. M. and Ulrich, R. K. (Eds), Physics of the Sun. Vol. II: Solar Atmosphere, D. Reidel Publ. Co., Dordrecht, Holland.

[83] Pojoga, S., Mouradian, Z. and Soru-Escaut I.: 1994, *Proc. of the Third SOHO Workshop - Solar Dynamic Phenomena and Solar Wind Consequences*, p. 23.

[84] Poland, A. I. and Mariska, J. T.:1986, *Solar Phys.* **104**, 303.

[85] Poland, A. I. and Mariska, J. T.:1988, in *Dynamics and Structure of Solar Prominences* (Eds.J. L. Ballester and E. R. Priest), p. 133 (Palma de Mallorca: Universitat de les Illes Balears).

[86] Pottash, S. R.: 1965, *Bull. Astr. Inst. Neth.* **18**, 7.

[87] Priest, E. R.: 1982, *Solar Magnetohydrodynamics*, D. Reidel Publ. Co., Dordrecht, Holland.

[88] Priest, E. R., Hood, A. W. and Anzer, U.: 1991, *Solar Phys.* **132**, 199.

[89] Priest, E. R. and Smith, E. A.: 1979, *Solar Phys.* **64**, 267.

[90] Raymond, J. C. and Smith, B. W.: 1977, *Astrophys.J. Suppl.* **35**, 419.

[91] Roberts, B.: 1985, in *Solar System Magnetic Fields* (Ed. E. R. Priest), D. Reidel Publ. Co., Dordrecht. Holland.

[92] Roberts, B. and Frankenthal, S.: 1980, *Solar Phys.* **68**, 103.

[93] Rompolt, B.:1990, *Hvar Obs. Bull.* **14**(1), 37.

[94] Rompolt, B. and Bogdan, T.: 1986, in *Coronal and Prominences Plasmas* (Ed. A. I. Poland), NASA Conf. Publ. 2442, p. 81.

[95] Rosner, R., Tucker, W. H. and Vaiana, G. S.: 1978, *Astrophys. J.* **220**, 643.

[96] Rust, D. M.: 1967, *Astrophys. J.* **150**, 313.

[97] Saito, K. and Hyder, C. L.: 1968, *Solar Phys.* **5**, 61.

[98] Saito, K. and Tandberg-Hanssen, E.: 1973, *Solar Phys.* **31**, 105.

[99] Secchi, A.: 1875, *Le Soleil* Gauthier-Villars, Paris, Vols. 1 and 2.

[100] Serio, S., Peres, G., Vaiana, G.S., Golub, L. and Rosner, R.: 1981, *Astrophys. J.* **243**, 288.

[101] She, Z. S., Malherbe, J. M. and Raadu, M. A.: 1986, *Astron. Astrophys.* **164**, 364.

[102] Simon, G., Schmieder, B., Démoulin, P. and Poland, A. I.: 1986, *Astron. Astrophys.* **166**, 319.

[103] Smith, E. A. and Priest, E. R.: 1977, *Solar Phys.* **53**, 25.

[104] Schmidt, H. U.: 1974, in Athay, R. G. (ed), *Chromospheric Fine Structure*, IAU Symposium No. 56, D. Reidel Publ. Co., Dordrecht, Holland.

[105] Sparks, L., Van Hoven, G. and Schnack, D. D.: 1990, *Astrophys. J* **353**, 297.

[106] Spitzer, L.: 1962, *Physics of Fully Ionised Gases*, 2nd edition, Willey Interscience, New York.

[107] Steele, C. D. C. and Priest, E. R.: 1990a, *Solar Phys.* **125**, 295.

[108] Steele, C. D. C. and Priest, E. R.: 1990b, *Solar Phys.* **127**, 65.

[109] Steele, C. D. C. and Priest, E. R.: 1991a, *Solar Phys.* **132**, 293.

[110] Steele, C. D. C. and Priest, E. R.: 1991b, *Solar Phys.* **134**, 73.

[111] Steele, C. D. C. and Priest, E. R.: 1994, *Astron. Astrophys.* **292**, 291.

[112] Tang, F.: 1986, *Solar Phys.* **105**, 399.

[113] Tandberg-Hanssen, E.: 1974, *Solar Prominences*, D. Reidel Publ. Co., Dordrecht, Holland.

[114] Tandberg-Hanssen, E. and Anzer, U.: 1970, *Solar Phys.* **15**, 158.

[115] Tucker, W. H. and Koren, M.: 1971, *Astrophys. J.* **168**, 283.

[116] Tucker, W. H.: 1973, *Astrophys. J.* **186**, 285.

[117] Van den Oord, G. H. J. and Zuccarello, F.: 1996, *Proceedings of IAU Symp.* 176. Stellar Surface Structure, Ed. K. G. Strassmeier.

[118] Van der Linden, R. A. M.: 1993, *Geophys. Fluid Dynamics* **69**, 183.

[119] Van Hoven, G., and Mok, Y.: 1984, *Astrophys. J.* **282**, 267.

[120] Van Hoven, G., Mok, Y. and Drake, J. F.: 1992, *Solar Physics* **140**, 269.

[121] Vesecky, J. F., Antiochos, S. K. and Underwood, J. H.: 1979, *Astrophys. J.* **233**, 987.

[122] Wentzel, D. G.: 1974, *Solar Phys.* **39**, 129.

[123] Wentzel, D. G.: 1981, in *The Sun as a Star*, ed. S. Jordan, p.331. NASA SP-450. Paris/Washington.

[124] Woods, D. T., Holzer, T. E. and MacGregor, K. B.: 1990, *Astrophys. J.*, **355**, 295.

[125] Wragg, M. A. and Priest, E. R.: 1981a, *Solar Phys.*, **69**, 257.

[126] Wragg, M. A. and Priest, E. R.: 1981b, *Solar Phys.*, **70**, 293.

[127] Wragg, M. A. and Priest, E. R.: 1982, *Solar Phys.*, **80**, 309.

[128] Wu, S. T., Bao, J. J., An, C. H., and Tandberg-Hanssen, E.: 1990, *Solar Phys.*, **125**, 277.

[129] Young, C. A.: 1896, *The Sun* (D. Appleton: New York).

[130] Zhang Yi and Engvold, O.: 1991, *Solar Phys.* **134**, 275.

[131] Zharkova, V. V.: 1989, *Hvar Obs. Bull.* **13**, 331.

[132] Zirin, H.: 1979, *IAU Colloq.* **44**,193.

[133] Zirin, H.: 1988, *Astrophysics of the Sun* Cambridge University Press.

[134] Zirker, J. B.: 1989, *Solar Phys.* **119**, 341.

[135] Zirker, J. B.: 1993, *Solar Phys.* **148**, 43.

[136] Zirker, J. B. and Koutchmy, S.: 1989, *Hvar Obs. Bull.* **13**, 41.

[137] Zirker, J. B. and Koutchmy, S.: 1990, *Solar Phys.* **127**, 109.